MICROWAVE-ASSITED SYNTHESIS OF FLUORESCENT CARBON NANOPARTICLES

A Thesis

by

BONNIE CHEN

Submitted to the Office of Graduate and Professional Studies of
Texas A&M University
in partial fulfillment of the requirements for the degree of

MASTER OF SCIENCE

Chair of Committee,	Kenith E. Meissner
Committee Members,	Andreas Holzenburg
	Jun Kameoka
	Michael J. McShane
Head of Department,	Ibrahim Karaman

August 2014

Major Subject: Materials Science and Engineering

ABSTRACT

Carbon nanoparticles (CNPs) are a new type of luminescent nanomaterial which have strong potential in biological and biomedical applications, and have been the subject of intense research in recent years. CNPs are nanostructures consisting primarily of carbon atoms and can have tunable optical performance under UV excitation. Moreover, properties including good bio-compatibility, water solubility, and a non-toxic response show that CNPs are safe for the body and the environment. Thus, they are good candidates for both *in vivo* and *in vitro* applications. These advantages give CNPs strong potential in term of bio-labeling and bio-imaging.

Although several synthesis routes have been explored, these methods either involve high cost or complex reactions. Here, we explore an innovative and simple microwave-assisted synthesis for the production of CNPs from glucose. This method can control tunable emission and the excitation wavelength of CNPs by manufacturing of output energy during synthesis. Moreover, photoluminescence properties are studied and discussed through emission and absorption spectra. The components, structure, and chemical bonding type are investigated by transmission electron microscopy (TEM) and Raman spectrum.

The results show that CNPs exhibit an amorphous structure with aromatic rings and carbon double bonds and particle size in a nano range which increases with output energy. The emission spectra of CNPs are broad, extending across the visible spectrum, and exhibit a shift with excitation wavelength and output energy. Finally, hypotheses on

the fluorescent mechanism and reaction process are proposed which are based on experimental data and literature. The CNPs could be 5-(hydroxymethyl) furfural (5-HMF) derivatives, which are major products of glucose decomposition.

ACKNOWLEDGEMENTS

This thesis was completed in my fourth year at Texas A&M University as a master's student, and analyzes, discusses and displays valuable results obtained in the three years of the research program. I am grateful for all the support and encouragement of numerous people including my advisor and committee members, my friends, my colleagues, and my parents, among others. Without their help and supports, I could not have continued.

First, I would like to thank my advisor, Dr Meissner, for his patience, kindness, encouragement and advice during the past three and a half years. As his student, I admired his rigorous approach to science and logical thinking, important training for any independent researcher. Moreover, I thank him for his encouragement when my research was at a standstill. As a research advisor and spiritual mentor, he was invaluable.

Also, I would like to thank my committee members, Dr McShane, Dr Kameoka, and Dr Holzenburg, for their comments and suggestions. In particular, Dr Holzenburg's TEM class improved my knowledge of instruments. Our discussions also gave me ideas for preparing the sample and were responsible for some high-quality TEM images.

I want to take this opportunity to thank all staffs in the Microscopy & Imaging Center (MIC) and the Materials Characterization Facility (MCF), particularly Rick Littleton in MIC and Dr Amanda Young in MCF. As instructors of TEM, spectrofluorometry, and Raman spectroscopy, they spent an enormous amount of time explain everything about the instruments. Their professional attitude and patience were

evidenced by every question they answered. They assisted me to solve the experimental and operating problems I encountered and helped me to explain and analyze the data I obtained. I learned a lot from them. I must also thank my colleagues and all members of the Meisser group. Yi-Hwang and Ravish made suggestions on microwave synthesis and semiconductor theory and phenomena. Thanks also go to my friends: Chao-Chen Wei for his suggestions about TEM operation and data analysis, Chen-Yu Ma and Chih-Hung Hsu for their feedback on computer program coding, Ying-Po Liang for discussions about extreme value theory. Thanks to Yu Han, Jean Yeh, Shih-Kai Hung and others for their company in the tough times.

Finally, and most importantly, I must express my respect and love to my mother and father for their spiritual and economic support. Without them, this dissertation could not have been completed.

NOMENCLATURE

3-DG	3-deoxyglucosone
5-HMF	5-(hydroxymethyl)furfural
CNPs	Fluorescent Carbon Nanoparticles
CNTs	Carbon Nanotubes
DI water	Deionized Water
EDS	Energy Dispersive Spectrometer
EVT	Extreme Value Theory
FWHM	Full Width at Half Maximum
HRTEM	High-Resolution Transmission Electron Microscopy
MWCNTs	Multiwall Carbon Nanotubes
PL	Photoluminescence
QDs	Semiconductor Quantum Dots

TABLE OF CONTENTS

Page

LIST OF FIGURES

LIST OF TABLES

CHAPTER I

INTRODUCTION AND LITERATURE REVIEW

1.1 Bio-detection application

Biodetection techniques have been widely used for diagnosis of disease and environment analysis during recent years. Researchers have used nanotechnology and nano-approaches to explore new bio-imaging and bio-labeling strategies based on fluorescent nanomaterials in both biological and medicinal detection[1].

Usually, fluorescent materials are used in combination with fluorescent microscopy. Fluorescent nano-agents are targeted at cell markers or objects in order to display the target cells on microscopic or camera images. Specific excitation light irradiates the specimen, which is treated by fluorescent agents. A digital camera detects the fluorescent emission wavelength only and shows a bright area against a dark background. The high contrast between the fluorescent target and non-fluorescent materials enhances the efficiency of microscopy. The use of fluorescent materials makes it possible to identify specific cell targets or sub-cellular components. This technique can be applied to both *in vitro* and *in vivo* targets[1, 2].

One of the most important techniques in bio-labeling based on fluorescent materials is immunofluorescence. Immunofluorescence takes advantage of the conjunction property innumerable antibodies and antigens. In one work the relation between antibodies and antigens was specific and strong [2]. Selected antibodies were treated chemically to attach the fluorescent agents. If the antigen presented in the target sample,

the labeling antibody conjugates bound to the antigens. After the sample was washed, fluorescent antibody-antigen combinations still remained. The result was that emission was visible by eye or detected by camera when the sample was exposed to light at its excitation peaks[2].

Another important development technique based on fluorescent materials is cancer tracing and cancer cell imaging for diagnosis and analysis. Cancer is the leading cause of death in developed countries, so its treatment has long been the goal of scientists and physicians. The first stage in cancer treatment is malignancy detection. However, most tumors are only detectable after growing larger than 1 centimeter. At that point, millions of tumor cells may already be metastasized and could cause serious damage to the body. Fluorescent imaging and labeling techniques are powerful and fast tools for cancer diagnosis and analysis. Since the fluorescent agents range from molecules to nano-size, agents are able to label cell components, such as mutant DNA, protein or cell membrane. Moreover, a labeling technique helps pathologists classify tumor cell types to make appropriate treatment recommendations to promote the success rate of surgery or chemotherapy. Therefore, fluorescent detection technologies dramatically raise the accuracy of diagnosis and analysis in medical detection[1].

1.2 Common fluorescent nanomaterials

Organic fluorophores are one of the most commonly used fluorescent agents in fluorescent maker techniques. Fluorophores are fluorescent chemical compounds that contain an aromatic group or cyclic structure with several π bonds. These molecules have the capability to absorb and re-emit light. Moreover, they have a high quantum

yield, which is the emission to absorption ratio. High-intensity emission of fluorophores is extremely valuable in bio-imaging applications. Hundreds of fluorophores have been well defined in terms of excitation and emission spectrum, as well as molecular structure. However, the molecule nature of fluorophores makes them easy to photobleach. When exposed to continuous light or inside the complex environment of a live cell, fluorophores degrade and destructure rapidly. The sensitivity and photostability of fluorophores limit their use in bio-imaging and detection applications[2].

Semiconductor quantum dots (QDs) have been widely used as bio-imaging and bio-labeling imaging agents. QDs are semiconductor nanocrystalline particles in the nanometer range. For these nano-scale materials, the physical properties show dramatic differences compared with macro-scale materials. These nano-scale particles confine photoexcited electrons and holes to produce unique optical and electronic properties. The different sizes of QDs limit the distance of electrons and holes and change the energy of the band-gap of the semiconductor. The tunable band gap makes differently sized QDs emit at different wavelengths. Therefore, this size tunability allows QDs to be engineered to suit different applications. Recent techniques allow QDs to be coated with a hydrophilic polymer shell and/or conjugated with antibodies or biological peptides to form an immunofluorescent probe [3, 4]. QDs have significant advantages over fluorophores, including greater quantum yield, higher photostability, multi-color emissions in single excitation wavelength, and size-tunable emission properties. However, as they are fluorescent agents, the toxicity resulting from the heavy metal

elements limits their applications in biological and live cell imaging. Hence, developing stable and non-toxic fluorescent agents is important for bio-detection techniques[3, 4].

1.3 Fluorescent carbon nanoparticle - literature review

1.3.1 Carbon nano-material generation

Carbon is the most important element for life on Earth. All organisms depend on carbon complexes to form their bodies. Most cell components, such as DNA and enzymes, are made of carbon atoms bonding with other elements, such as oxygen, hydrogen, and nitrogen. Carbon allotrope is also an important subject for carbon material science, since the structures affect the physical properties leading to different uses. Diamond and graphite are the most well-known carbon allotropes and have been used for hundreds of years. Recently, several carbon nano-materials have been discovered and researched, such as buckminsterfullerene (C_{60})[5], carbon nanotubes (CNTs)[5], and nanodiamonds[5]. Their special chemical and physical properties point to a high potential in applications in industry and medicine.

1.3.2 Fluorescent carbon nano-particles discovered by accident

The first fluorescent carbon nanoparticles (CNPs) were discovered accidentally by Xu and co-workers in 2004[6]. When making carbon nanotubes derived from arc-discharge soot on graphic sheet, they also found some carbon particles during electrophoretic purification. Under 365 nm UV illumination, these particles emitted visible blue light. These new fluorescent nano-particles were termed “carbon dots.” After this interesting report was published, several researchers started to examine the properties of CNPs. CNPs exhibited high photostability and were non-toxic to living

cells[7-10]. These advantages gave CNPs greater potential than fluorophores and QDs in bio-imaging and bio-labeling applications.

1.3.3 Other physical properties of CNPs

In addition to photostability and low toxicity, the structure of CNPs has also been researched. Most papers report CNPs smaller than 50 nm in diameter. As observed by high-resolution transmission electron microscopy (HRTEM), CNPs present globular or tubular structures with a layer around the hollow center [9, 11-17]. Some results showed CNPs with sheet structures with diameters of 10-300 nm, which is similar to the crystalline lattice of graphite [18-21]. Elemental analysis showed compositions lacking metal elements, which means CNPs only include carbon, hydrogen, oxygen, and nitrogen atoms. This analysis demonstrated the CNPs were organic compounds [6, 13, 19, 22, 23].

Bonding types of CNPs have also been reported in many papers. Most papers reported that CNPs presented carboxyl or carboxylic acid functionalities on their surface. Also, some papers reported the absence of carbon (sp3) and (sp2) bonding vibrations [10, 12, 13, 15, 17, 21, 23]. The absence of sp3 carbon bonds indicated that the CNPs possessed a diamond-like structure, a graphite structure or some aromatic rings, analogous to chrysene, pyrene, etc. [9, 18, 19, 21]. Despite the research about bonding and structure, the chemical structure of CNPs is still unclear.

1.3.4 Synthesis routes review

Several routes have been used to synthesize CNPs. Generally speaking, the techniques for synthesis of CNPs are categorized either as top-down or bottom-up. After

CNPs are made, surface passivation is often applied; here, we discuss only the approach to making raw CNPs.

1.3.4.1 Top-down synthesis process

Top-down synthesis routes have been developed since 2004. In top-down processing; the process starts from bulk or 100-nanometer carbon materials such as graphite or carbon nanotubes as the carbon source. Then these materials are processed with a high energy laser or ionic beam, oxidized and thinned. The sizes of CNPs can be controlled to 1-3 nm. Moreover, the process allows engineers to design desirable geometries in CNPs.

Depending on the different energy used to thin the carbon source, top-down synthesis can be separated into different categories, laser-ablation, and electrochemical treatments. Laser-ablation or focus ionic beams are the most common methods used to synthesize CNPs. For ablation[11], researchers use a hot-pressing mixture of graphite powders and cements as carbon target with a high-pulse laser. The laser is focused on the carbon source and ablation occurs in a flow mixture of argon gas and water vapor. Once the CNPs are produced, a luminance test is applied and no fluorescent reaction is detected. The CNPs are then treated with nitric acid for several hours and bright luminance is detected after treatments.

Electrochemical treatment is the other common route in top-down synthesis [24]. Researchers use multiwall carbon nanotubes (MWCNTs) as the carbon source. The nanotubes are designed to serve as the electrode in an electrochemical cell. Under the electric potential circle, the solution take place a redox reaction by applying currents.

Since the effective electrochemical area increases with CNP generation, larger charging currents are observed during the potential circle. Finally, these CNPs are extracted by evaporation from acetonitrile solution to water and fluorescent examinations are applied.

Top-down synthesis has several advantages. It allows researchers to control the size, shape and structure externally during the process. Although it can exactly control the size and shape of CNPs, the top-down process needs expensive equipment and rigid conditions in order to maintain a quality manufacture environment. Moreover, complex steps and designs mean that CNPs are generated slowly. The low productive yield makes the manufacturing process time-consuming. These disadvantages drive researchers to develop new types of synthesis routes.

1.3.4.2 Bottom-up synthesis process

The bottom-up synthesis process builds CNPs from atomic or molecular species via chemical reactions. Acid oxidization and heat processes are the most useful routes in this class of synthesis for combining the carbon atoms. Since there are so many different methods, here we only list the general steps in three processes [5, 10, 12-17, 22].

Step 1: Prepare the carbon precursors. Several carbon sources such as graphite, glucose, candle soot, or citric acid could be used to form the CNPs.

Step 2: Oxidize the carbon precursors. Researchers usually oxidize the carbon precursors in an acid solution, such as sulfuric acid (H2SO4), nitric acid (HNO3), hydrochloric acid (HCl), etc. This step is usually performed at high temperature during the experimental process. Some researchers only heat the solutions of carbon precursors

without an acid solution, burning the carbon precursors to achieve the oxidization reaction.

Step 3: Final treatment to passivate the surface [14]. After oxidization, CNPs are produced. Some researchers further passivate the surface of CNPs with organic cappings or metallic elements. This makes CNPs easier for other experimental examination, enhances the quantum yield or renders them suitable as fluorescent agents for imaging or labeling.

These routes have advantages including low cost and ease of synthesis. High product yield and high effective product rate allow researchers to synthesize large amounts of CNPs within a short time. However, the bottom-up routes involve complex reactions so it is hard to control the whole reaction. Compared with the top-down synthesis, the bottom-up makes it more difficult to control the functional groups of products, particle size distributions, particle shape and compositions of CNPs.

1.3.5 Research problems for CNPs at the present stage

Similarly to QDs, CNPs have special optical properties and high stability so they have great potential for in vitro and in vivo applications. However, as far as we know, there are no mature synthesis processes for manufacturing CNPs. With top-down synthesis routes researchers can control the size and shape of CNPs. However, yield is low and it needs expensive equipment to maintain a high-quality manufacturing environment. With bottom-up synthesis routes researchers can produce CNPs of high yield with a low-cost process. However, the complex reaction makes it hard to control all the reactions and functional groups of the products. Moreover, as far as we know, no

bottom-up synthesis process has been designed to control the emission properties of CNPs during the process. Most synthesis processes manufacture CNPs but do not engineer emission spectra according to need. Therefore, to obtain a mature fluorescent agent in bio-imagery or bio-labeling applications, developing a synthesis process that produces CNTs with tunable emission properties is very important.

The luminescence mechanism of CNPs is still unclear. Some researchers assume that the tunable emission properties of CNPs by size are similar to those of QDs [6, 16]. Other researchers propose different explanations: the photoluminescence of CNPs is attributed to the presence of surface energy traps which are affected by quantum confinement [11, 14, 17, 20, 21]. After passivating the surface, CNPs exhibit stronger photoluminescence. Researchers think this phenomenon results from the increase of surface to volume ratios of CNPs [11, 14, 17, 20, 21]. On the other hand, other researchers think the luminance mechanism of CNPs relates to a small, conjugated aromatic domain within the CNPs [9, 18, 19, 21].Those domains, with various sizes, coexist in a single, physically connected CNP [9, 18, 21]. In brief, these assumptions lack clear experimental evidence, and the luminescence mechanism of CNPs is still an open question.

1.4 Purpose of research

This thesis has a threefold purposes:

(1) **to design a microwave synthesis method for controlling tunable emission properties of CNPs.** The experiment uses a bottom-up synthesis process. For the carbon precursor, we chose glucose. Glucose is a simple monosaccharide which is

found in animals and plants. This digestible sugar is safe for any living cell. A microwave is used for oxidization of CNPs. The microwave-assisted hydrothermal method has several advantages. First, water is the solvent and is non-toxic, non-flammable, and non-corrosive. This ideal solvent provides a non-hazardous and environmentally friendly reaction [25]. Second, water is a microwave absorber. The microwave-assisted method transfers heat directly to the reaction, creates homogeneous heat distribution, and causes reactions quickly. The whole experiment is developed in safe and low-cost conditions.

(2) **to study and analyze the properties of CNPs in relation to microwave experimental parameters.** In order to produce CNPs with tunable emission properties, different experimental parameters during microwave heating will be studied, including temperature, heating time, heating power, pressure, and input energy. The emission spectrum and excitation spectrum will be fitted and defined by the fitting parameters. Physical properties, such as particle size and bonding type, will also be examined by experimental instruments.

(3) **to propose a hypothesis for the luminance mechanism of CNPs.** In this work, the results will be discussed and supported by reference papers to provide an explanation for the fluorescent mechanism of CNPs. Several hypotheses proposed by other researchers will be reviewed and compared with our experimental data and explanations. Finally, a generalized summary regarding the structure of CNPs and a hypothesis will explain the luminance mechanism of the CNP structure.

CHAPTER II

THEORY

2.1 Fluorescent mechanisms

Fluorescence is a form of photoluminescence in which a substance absorbs ultraviolet or visible light photons, and then emits light from an electronically excited state. Depending on the different types of electronic configurations of the excited states and the transitions in emission pathways, photoluminescence can be divided into two categories, fluorescence and phosphorescence [2]. The first is a process whereby fluorescent materials absorb particular wavelengths from ground state to singlet state. Then excited electrons return to ground state with emission photons. Fluorescent materials emit a longer wavelength after a brief interval, usually between 10^{-9} and 10^{-7} s. Phosphorescence is similar to the fluorescence process. The electrons excite from ground state to single state but jump to the lowest triplet state to relax energy; this is called the intersystem crossing process. Finally, electrons return to ground state with emission. This emission is called phosphorescence. It usually has much longer time intervals [2], between 10^{-3} and 10 s.

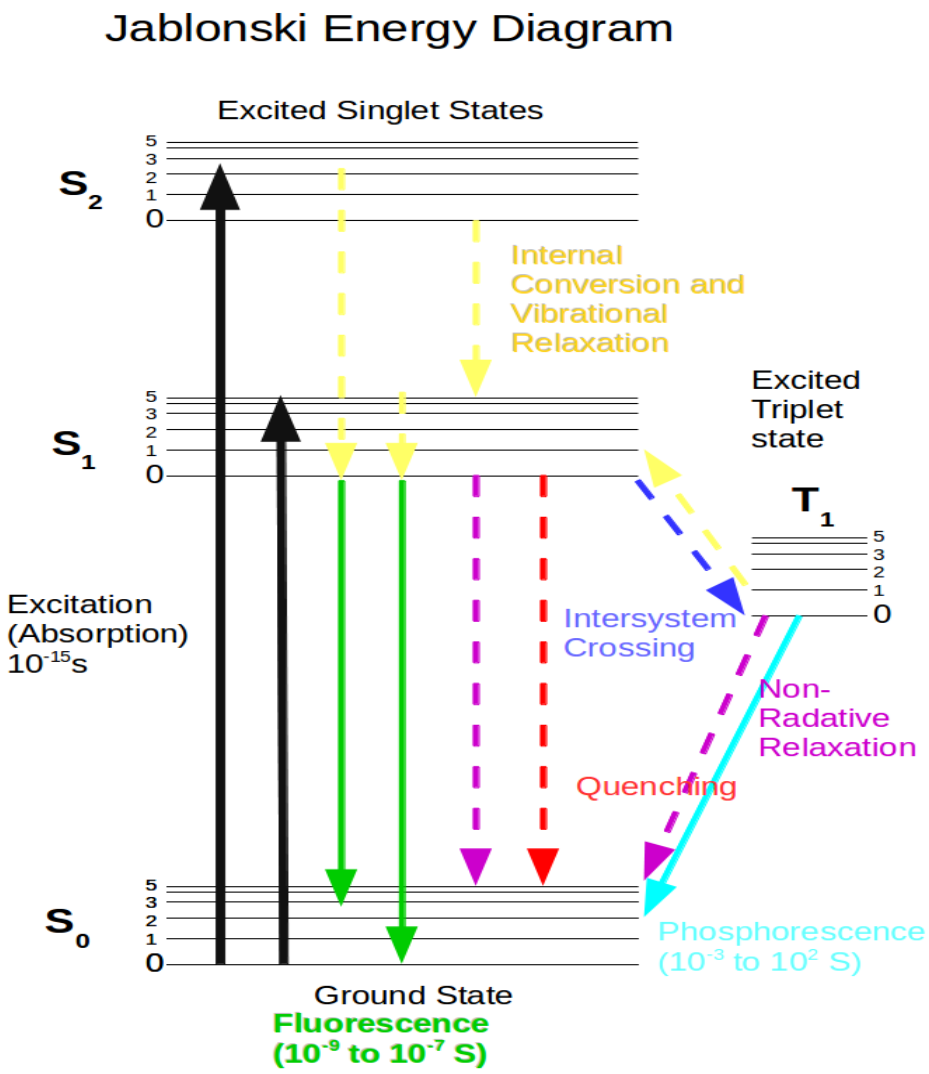

Figure 2-1. Jablonski energy diagram of fluorescent mechanism.

2.1.1 Jablonski energy diagram

The Jablonski energy diagram is the most usual way to explain the electronic configurations of the excited states and emission pathways of the fluorescence mechanism. Fluorescent molecules possess several different electronic states. The

Jablonski energy diagram illustrates the singlet ground state S_0 from which the excitation process starts, as well as first and second excited singlet state. Each state is subdivided into vibrational and rotational energy levels, which result from different atomic nuclei and bonding orbitals. After molecules absorb energy, they may change to other states in a number of different ways, including emission of photons, molecular inter-conversation and non-radiative relaxation processes. According to quantum mechanism theory, only specific wavelengths of light can be absorbed since electron energy levels are not continuous. The specific wavelength range is called the absorption band [2].

As energy is absorbed, fluorescent materials or molecules are excited to the first (S_1) or second (S_2) energy states. Then the electrons will slowly relax to the lowest vibration energy level of the first excited state. They exhibit several behaviors in order to release over-load energy. These behaviors are listed in Figure 2-1. and Table 2-1. When the electron absorbs energy and arrives at the excited state vibration level it will slowly relax the lowest vibration level of S_1. These processes are internal conversion (from S_n to S_1) and vibration relaxation (from S_1 to S_1). Fluorescence occurs when the relaxation from lowest vibration energy level in first state to ground state is accompanied by emission of a photon. As a result, the fluorescence spectrum shifts to a longer wavelength than the excitation spectrum because of the loss of vibration energy. Also, excitation energy can be dissipated in a non-radiative way (e.g. heat) or by collision with another molecule to transfer energy. A phenomenon termed intersystem crossing means the electrons go to the lowest excited triplet state (T_1). The consequence is that the electrons release energy in the emission of a photon through phosphorescence [2].

Table 2-1 Relaxation process type[2].

Transition	Process	Rate Constant	Timescale (Second
Type	Name		Interval
S_0 => S_1 or S_n	Absorption (Excitation)		10^{-15}
S_n => S_1	Internal Conversion		10^{-14} to 10^{-10}
S_1 => S_1	Vibrational Relaxation		10^{-12} to 10^{-10}
S_1 => S_0	Fluorescence		10^{-9} to 10^{-7}
S_1 => T_1	Intersystem Crossing		10^{-10} to 10^{-8}
S_1 => S_0	Non-Radiative Relaxation Quenching		10^{-7} to 10^{-5}
T_1 => S_0	Phosphorescence		10^{-3} to 100
T_1 => S_0	Non-Radiative Relaxation Quenching		10^{-3} to 100

2.2 Microwave assisted synthesis method

2.2.1 Microwave basics

Microwaves are part of the electromagnetic spectrum. They occur in a transition region between infrared and radiofrequency radiation. The wavelengths range from 1 cm to 1 m, and frequencies are between 300 GHz and 300 MHz. The relation between energy, E, frequency, υ, wavelength, λ, and angular frequency, ω, is given by:

$$E = \hbar\omega = h\upsilon = \frac{h\boldsymbol{c}}{\lambda}$$

where $\boldsymbol{c}$ is light speed. The energy of a microwave in industrial or domestic ovens is close to 0.00001eV (2.45GHz, 12.22cm). Compared with chemical bonding or Brownian motion, the energy is too small to induce chemical reactions. The main interaction is

matters interacting with microwaves and transforming electromagnetic energy into heat [26].

2.2.2 Heat resulting from dipole motion

Some insulating materials can be heated by high frequency electromagnetic energy because it does not have the ability to transfer energy when subjected to an electric field. The consequence is that electromagnetic energy is accumulated. If the materials contain polar molecules which have an electrical dipole moment, the molecules rotate to align with the applied field. If the field is oscillating or alternating, the molecules rotate continuously to achieve alignment. The rotating molecules collide with other surrounding molecules and transfer energy. Since temperature is the average kinetic energy, the collisions of molecules dipoles result in a temperature increase to reach thermal equilibrium. The interactions between electromagnetic waves and matter can be quantified by a complex physical parameter, dielectric permittivity. This parameter is described by an equation:

$$\tilde{\varepsilon} = \varepsilon' - j\varepsilon''$$

The $\varepsilon'$and ε'' are the real and imaginary parts of complex dielectric permittivity [26].

2.2.3 Dielectric loss

The torques exercised by an electric field induce the rotation of molecules, and these molecules need a time to polarized, which induced a delay comparing with ideal rotation rate. This delay makes molecule rotate non-ideally. This delay is defined as relaxation time, τ. Relaxation processes are probably the most important of the interactions between electric fields and matter because the delay causes energy to

dissipate when electromagnetic waves move across the materials. In order to identify the frequencies, ω, the region causing the relaxation, Debye describes the modification of dielectric permittivity, ε, by optical frequency [27]. The results show that dielectric loss covers a broad range. The maximum is

$$\varepsilon''_{max} = \frac{\varepsilon_s - n^2}{2}$$

where n is refractive index and ε_s is static permittivity or permittivity for a static field, when the

$$\boldsymbol{\omega_{max} = \frac{1}{\tau}}$$

2.2.4 Thermal dependence of dielectric loss

According to both theory and experimental results, the specificity of microwave heating results from the thermal dependence of a dielectric property. The complex dielectric permittivity also depends on the temperature and dynamic behaviors of molecules provided by thermal energy. Moreover, the electric field amplitudes depend on the real and imaginary electric permittivity, so the electric field also depends on the temperature.

The applied energy results in dissipated microwave energy, and the dissipated energy depends on the dielectric property. Therefore, the heating rate depends on the materials' properties (thermal diffusivity and specific heat). The heat resulted from microwave dissipated energy caused an increase in temperature, and the increasing temperature produced a feedback to the dielectric property, and further affected the dissipated energy. The effect becomes a cycle, shown as Figure 2-2 [28].

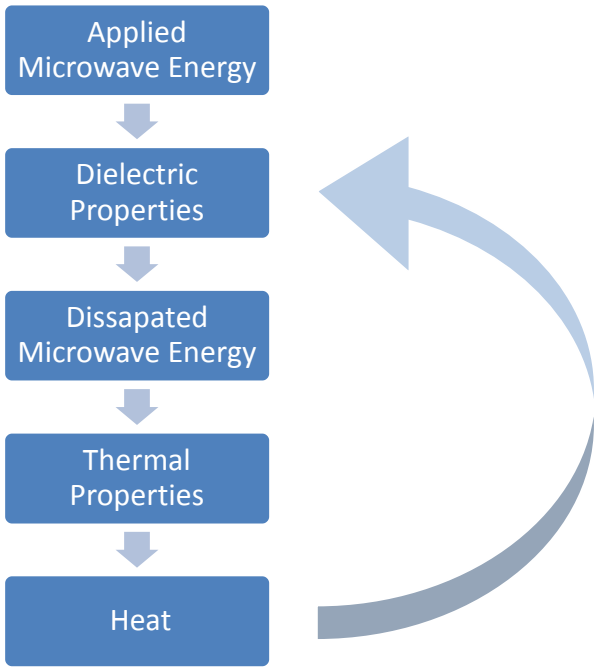

Figure 2-2. Schematic diagram of thermal feedback for dielectric properties.

2.2.5 Efficiency of energy and power

The heat generated in a unit volume is the electric field strength of the microwave field, the frequency, and the dielectric properties of materials. The microwave power dissipation can be shown by:

$$P_d = 2\pi\omega\varepsilon_0\varepsilon'' E^2$$

Here, P_d is the power transfer in unit volume of materials. ω is the operating frequency. ε_0 is dielectric permittivity of free space, or the dielectric constant, and = 8.85×10^{-12}

AS/Vm. ε'' is imaginary part of complex permittivity, also termed the dielectric loss factor. E is electric field strength. In this formula, the conductivity is negligible [28].

Electric permittivity is a characteristics of materials, and shows the level of microwave power absorption by the materials. If the loss factor is high, the substance is a better microwave energy absorber, which means it is easier to be heated in the electric field. Water and all aqueous solutions exhibit a high loss factor so they can absorb high frequency energy. Compared with water, sugar has a low loss factor because of its symmetrical structure.

However, the electric field strength is determined by the design of the microwave device applicator as well as conditions of the dielectrics in the applicator. Therefore, there is no way to find out the actual electric field strength in real microwaves. The microwave power is absorbed by materials and can be described in calories. In the applicator, a vessel with liquid w (g) at an initial temperature T_1 (℃) is irradiated for t (s) to raise the temperature to T_2 (℃). The liquid has specific heat C (J/kg K).

$$\boldsymbol{P_r = \frac{wC(T_2 - T_1)}{t}}$$

The heating efficiency could be

$$\eta = \frac{P_r}{P_{microwave}} \times 100\%$$

2.2.6 Microwave scales

The primary mechanism of microwave heating is dielectric loss, which affects the microwave energy transfer. Dipole rotation affects the alignment of molecules in the

electric field. At 2.45GMHz, the field oscillates 4.9×10^{9} times per second and agitates molecules to generate heat. The quantity of heat produced by dipole rotation is determined by the dielectric relaxation time of the sample, which is also affected by temperature and viscosity.

CHAPTER III

EXPERIMENTAL METHOD

3.1 Research design

The CNPs were synthesized by a microwave-assisted synthesis method. This method was established and modified according to the results of Dr Yang and her group [29]. A laboratory microwave instrument (CEM microwave system) was used for both aqueous and water-free chemical reactions. All experiments were performed without the addition of any catalyst. Glucose powders were used as the primary carbon source. Although CNPs could be synthesized in both aqueous and water-free reactions, in this project only the properties of CNPs in aqueous reactions were studied. For aqueous synthesis, the concentration of glucose powders was fixed at 33%. The pressure during the heating process was kept below 23 psi. The dependent variables, including heating temperature, heating time, and supply output power of the microwave system, were controlled by the CEM microwave instrument and software. During the heating process, the solution changed color, from clear to dark brown, with the generation of fluorescent CNPs. Therefore, the color of the solutions was the first benchmark for judging whether products were made or not. After generation of the CNPs, samples were cooled to room temperature by the air vent of the CEM microwave. Then, the CNP solution was deposited in a sealed glass tank and were examined for fluorescent or other physical properties. There were no passivation steps or other surface modification reactions. The

CNP solution exhibited stable fluorescence after six months. The whole experimental process is shown in Figure 3-1.

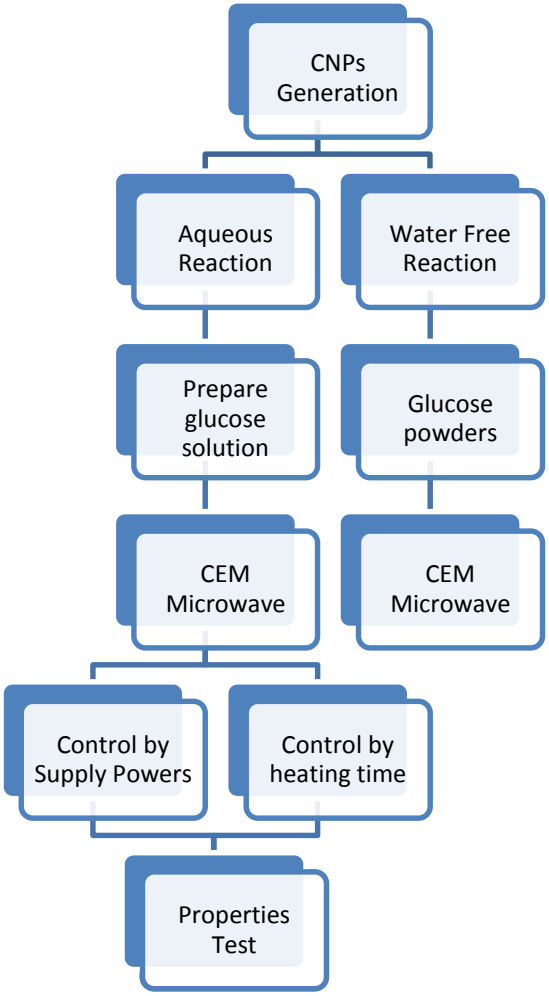

Figure 3-1. Process of microwave assisted synthesis procedure

3.1.1 CEM (CEM Corp., North Carolina, USA) microwave system

The Discover® system is a single-mode focused microwave system with a resonant cavity, designed for optimized energy transfer, as Figure 3-2. The microwave maximum power output is 300 watts in pulsed control mode with a magnetron frequency of 2.45 GHz. Also, the system is able to operate both in pressurized reaction vials and at atmospheric pressure. An optical IR thermometry sensor is situated under the reaction vessel to detect and control the temperature. This system can work at temperatures up to 300℃. Synergy™ software controls and monitors the reaction temperature, time, power and pressure during the synthesis process.

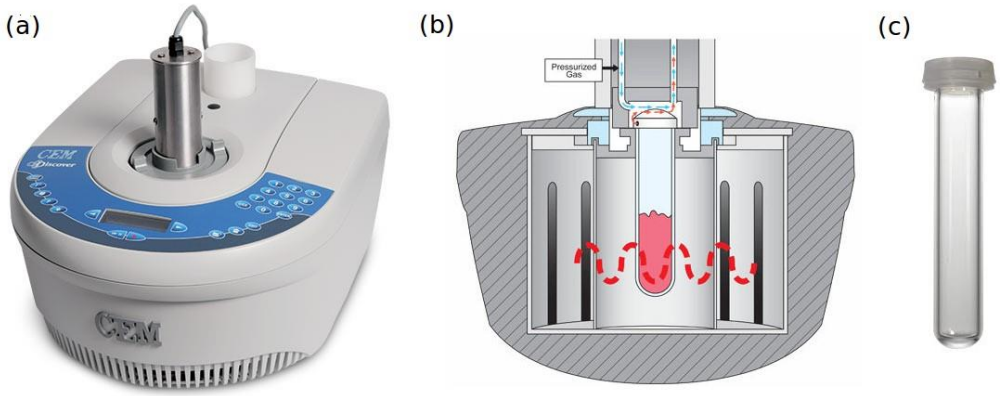

Figure 3-2. CEM Discover® microwave instrument. (a) Schematic diagram of the top of CEM Discover® microwave instrument. The reactor had one cavity with a pressure device. A monitor in front of the cavity showed the temperature and time and connected the instrument to computers. (b) Illustrates CEM's microwave heating theory. During the microwave process, the surrounding microwave reactor provided a uniform electromagnetic field whose density ensured the sample heated evenly. A vent in the pressure device to remove extra gas released unexpected pressure; the vent also kept the reaction under sealed conditions. (c) Side view of specific glass vessel with lip seal that is used by the microwave. Illustration courtesy of CEM Corporation (2006) website [30].

3.1.2 Materials

D-(+)-glucose powder was purchased from Sigma-Aldrich (Missouri, USA). The purity of powders was over 99.5%. Deionized water (DI water) was used for the preparation of aqueous solutions.

3.1.3 Moderate and hydrothermal temperature of water

In this research work, both moderate temperature and hydrothermal conditions were used during the microwave heating process; hydrothermal conditions mean the temperature of the water was over 100 ℃ but below the critical temperature 374 ℃ (221 bar)[25]. Usually the range of temperatures was from 100℃ to 260℃ for organic chemistry since reaction behavior under these conditions is well understood[25]. Moreover, the dielectric permittivity decreased as temperature increased [25]. This resulted in the reduced polarity of the water. In hydrothermal conditions, water can be the solvent, reactant, catalyst, medium or a combination of these. Water as solvent can create a clear, safe, and economic reaction for organic chemistry [25, 28].

3.1.4 Aqueous phase CNPs synthesis

Two grams of glucose powder were put in an Erlenmeyer flask and dissolved in 4 ml of DI water. In order to make the supersaturated glucose solution, the solution was heated for 30 min at 75℃ to allow the glucose to dissolve. Then the solution was cooled down to room temperature. In this stage, the solutions were observed to be transparent with no undissolved glucose. Also, no fluorescence was observed under UV light.

3.1.5 Microwave heating

For the CEM microwave system, both moderate temperature (89 to 100℃) and hydrothermal temperature (100 to 123℃) were used on different samples. Heating time (5 to 15 min) and microwave power (100 to 300 W) were also controlled variables in the synthesis process. Ten ml glass vessels were used with 5 ml of glucose solution with a lip-type seal. The experiment started at ambient pressure and room temperature. The microwave process operated under dynamic pressure and a temperature mode with fixed power and time. During heating pressure built up in the vessel, the final pressure reached a maximum of 22 psi. After heating, the solutions were air cooled to room temperature. Finally, if the solutions had visible emission under UV excitation, CNPs were deemed to have been successfully synthesized.

Sample microwave heating process temperature profiles are shown in Figure 3-3. The first 37 seconds served as a preheating stage for all samples. In this stage the temperatures increased rapidly because of the high dielectric constant of water. After the temperature reached 85 to 90 ℃, the temperature profile entered a second stage. In the second stage, the reaction temperatures maintained a high temperature level but increased slowly. That resulted from the dielectric constant of water decreased when temperature over 100 ℃ [25], but the reactions continued and CNPs were generated during this stage. Finally, the reaction times were achieved and the power shut down. The temperatures went through an exponential decrease (not shown). During the heating reaction, the maxima of temperature and pressure increased with increasing output power.

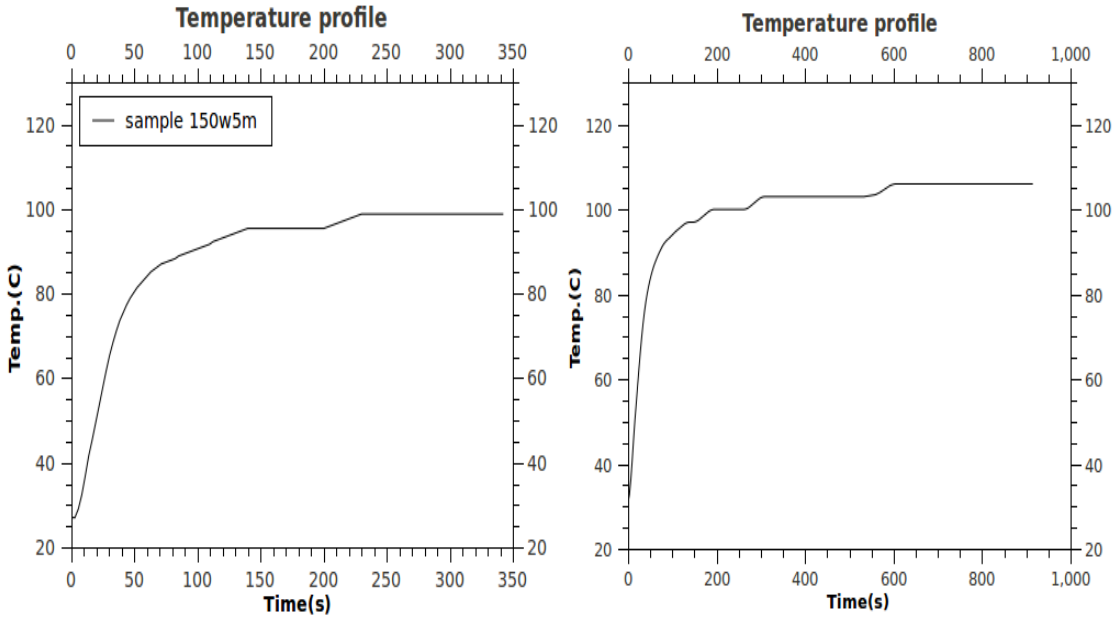

Figure 3-3. Typical microwave heating temperature profile of CNP solutions with time. The temperature rose fast in the first 37 seconds. After 37 seconds, the temperature reached 80℃ and became stable; the rate of rise decreased.

3.1.6 Key factors controlling the emission properties of CNPs

In the original literature [29, 31], temperature and heating time were considered as the key parameters in controlling the emission wavelengths. Under different synthesis temperatures and times of synthesis process, the CNP solution presented various color fluorescence. The temperature was thought to be the primary factor which controlled the emission wavelength [29, 31]. However, after examination of hundreds of samples which were synthesized in different temperatures from 100 to 180℃, a statistical

analysis show the combination of heating time and heating output power (input energy) was the major parameters affecting the CNP of emissions. In order to validate this hypothesis, a series of CNPs were manufactured in 5, 10 and 15 min of heating times and with 100, 150, 200, 250, and 300w of microwave output power. (See Table 3-1.) Images of CNPs under UV excitation are shown in Figure 3-4. The result of a statistical analysis of the samples is presented in Chapter 5.

Table 3-1: Fifteen samples at various heating times and heating output power during synthesis process.

time\power	100 Watts	150 Watts	200 Watts	250 Watts	300 Watts
5 min	100w5m	150w5m	200w5m	250w5m	300w5m
10 min	100w10m	150w10m	200w10m	250w10m	300w10m
15 min	100w15m	150w15m	200w15m	250w15m	300w15m

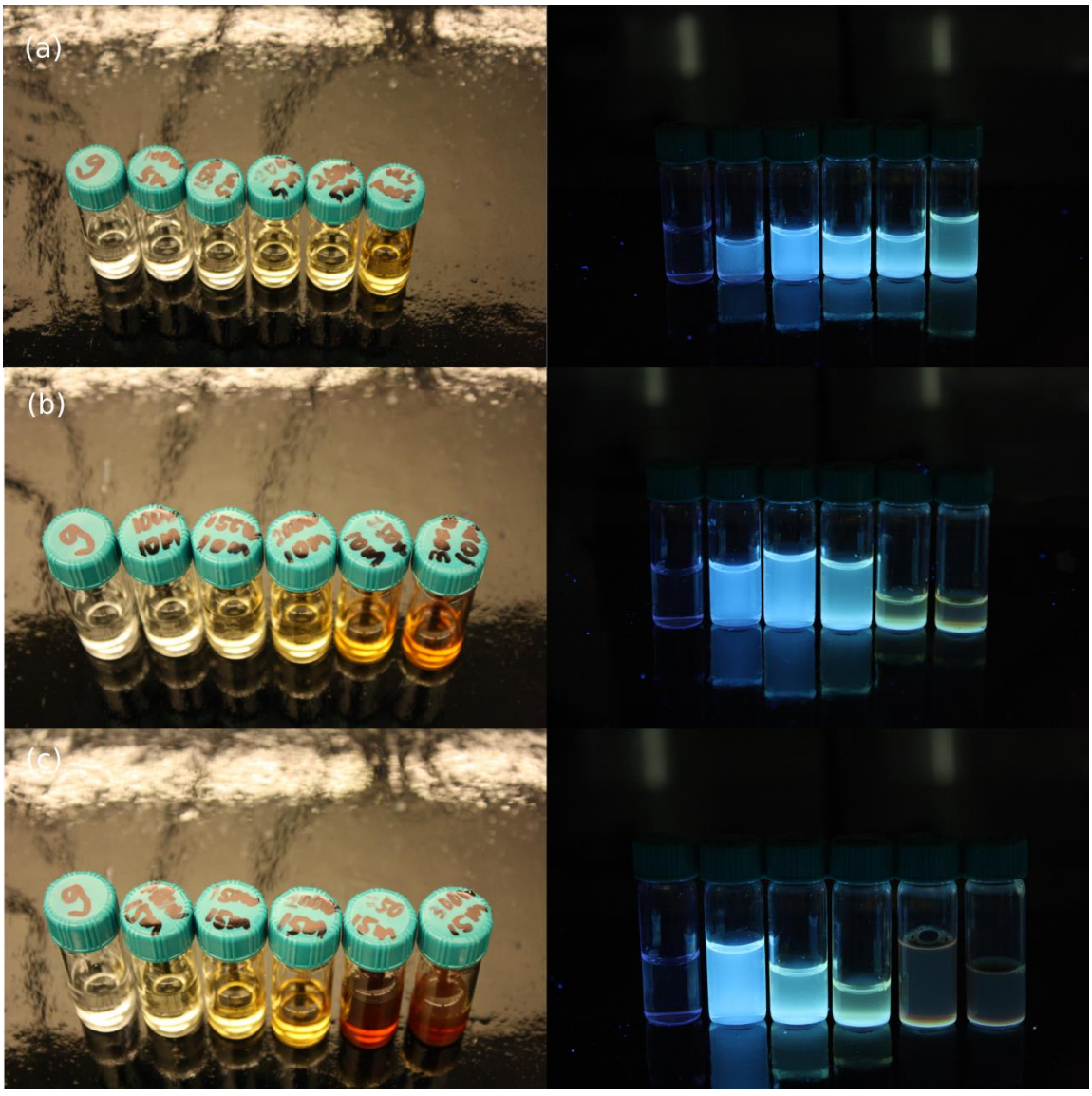

Figure 3-4. Microwave-assisted synthesis of CNP by time and power. (a) Synthesis under 5 min. (b) Synthesis under 10 min. (c) Synthesis under 15 min. The first sample on the left was supersaturated glucose solution, which did not show fluorescence. Samples from left to right were synthesized under 100w, 150w, 200w, 250w and 300w output power. UV exposure revealed different fluorescence from blue to yellow

3.1.7 Solid phase fluorescent CNPs

The CNPs were also synthesized in water-free conditions whereby 2 g glucose powders were deposited in a reaction vessel with no water or other chemical solvents. The synthesis temperature was controlled in an open vessel (1 atm pressure) between 140 and 150℃. The power of the microwave was fixed at 250 Watts. During the heating process, the glucose powder liquefied before burning. Liquid could be designed for desired shape by compression and transfer molding method before the liquid cooled down to the room temperature. Solid-state fluorescent CNPs were produced. The reaction times were not a fixed value. The times were between 2 and 3 min before burning the liquid. Figure 3-5 shows images of the CNPs exposed to visible and UV light.

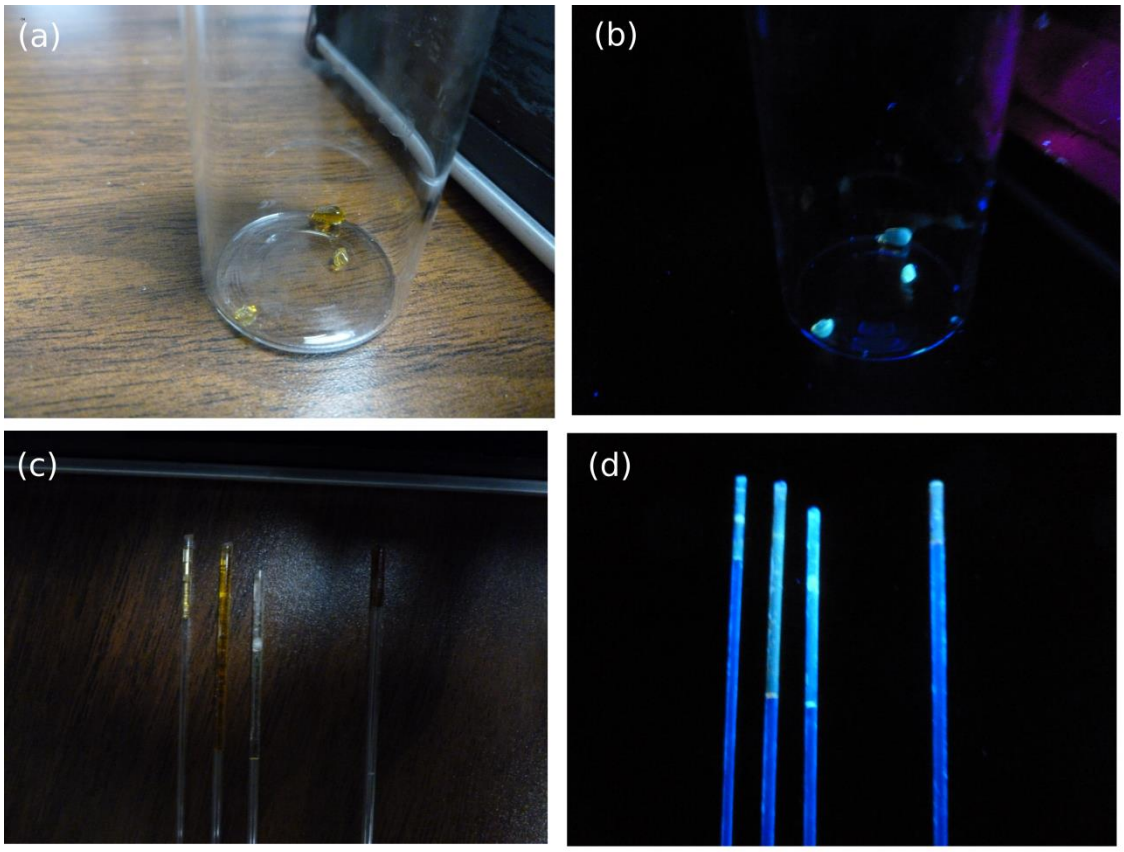

Figure 3-5. Solid phase of CNPs under visible and UV light. (a)(c) Visible light. (b)(c) UV light. Blue fluorescence could be observed after exposure to 340 nm UV light. The particles can reach 0.5 cm; the shape of fluorescent CNPs could be engineered by microwave synthesis.

3.2 Properties analysis

After synthesis, the optical properties and physical properties of the aqueous CNPs were analyzed. For optical properties, the fluorescent emission and excitation spectra were recorded by a spectrofluorometer and the absorbance spectra were recorded by a UV-Vis-NIR spectrophotometer. Physical analysis was done with transmission electron

microscopy (JEOL JEM-2010 TEM), an energy dispersive spectrometer (EDS), and Raman spectrometer (Horiba Jobin-Yvon LabRam IR system).

3.2.1 Physical properties analysis

3.2.1.1 Transmission electron microscope (TEM) and energy dispersive spectrometer (EDS)

A JEOL JEM 2010 TEM was used for high-resolution imaging. The accelerating voltage was 200 kVwith an LaB6 filament. A Digital Gatan SC1000 ORIUS CCD camera was used for imaging. In addition, an Oxford Instruments ATW type EDS detector with INCA Energy TEM platform was used for chemical analysis.

TEM sample preparation

The CNP solutions were prepared by a negative staining method on the grid in order to increase image resolution. The preparation process was illustrated in Figure 3-6. First, the grids were cleaned with acetone and ethanol twice and then dried. Second, three drops of sample solution, 2% Uranyl Acetate and DI water were dropped on a cleaned KIM film. Third, a carbon film coated with mica was immersed in sample solution for 30 seconds (carbon side uppermost) and then immersed into the 2% uranyl acetate solution for 30 seconds (carbon side uppermost). The mica coated carbon film was placed in DI water. The carbon film with CNPs floated on the surface of the water. Finally, the carbon film was attached to the grids to gain the TEM image sample [32].

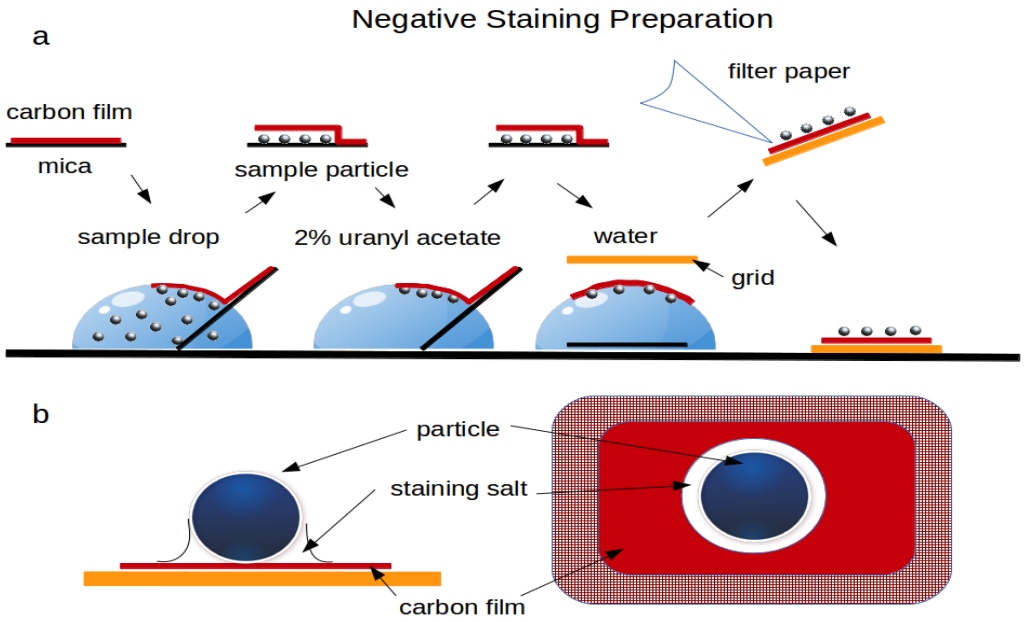

Figure 3-6. Negative staining TEM sample preparation method. (a) Steps of preparation. Specific mica coating carbon film was used to immerse the sample solution and 2% uranyl acetate solution. The CNPs were attached between the layer of mica and carbon film. Then, the film was put in the water. The mica film sank into the water and the carbon film and CNPs were suspended on the surface . Finally, attached the carbon film by grid. (b) Schematic of sample CNPs surrounded by staining salt, which were able to enhance the visibility under TEM [32].

3.2.1.2 Raman spectroscopy

A Horiba Jobin-Yvon LabRam IR system was used for confocal Raman microscopy. The instrument provided highly specific spectral fingerprints which enabled precise chemical and molecular characterizations and identifications. A 785 nm single wavelength laser was selected to prevent fluorescence. Raman spectra were collected in the 100 to 3000 cm^{-1} range.

3.2.2 Measurement of optical properties

3.2.2.1Emission and excitation scanning spectra

PTI QuantaMaster series spectrofluorometer was used to measure the emission and excitation spectra. A plastic cuvette which had no fluorescent emission was used as the container. Lasers in the equipment emitted specific wavelengths to excite the sample and record the emission spectral. Single wavelength lasers with UV-light of 340 nm, and 380 nm, and visible light of 420 nm, and 460 nm served as excitation wavelengths; to excite the samples and yield the fluorescent emissions. After examining the emission spectra, we chose the minimum wavelength to scan the excitation spectra.

3.2.2.2 Absorbance

A Hitachi U-4100 UV-Vis-NIR spectrophotometer was used for measurements of the absorbance spectra. Tungsten and deuterium lamps were used for UV and visible light sources, respectively. The wavelength scanning ranged from 200 to 700 nm. A quartz cuvette which had no absorbance between 200 and 700 nm was used as the container. Since the CNP solution had high absorbance, three different concentrations of solution, 100%, 10% and 1% CNPs diluted with water were measured.

3.3 Fitting of data and procedure

Mathematical fitting of data has several advantages for analysis of the experimental data. First, it provides a way to know what kind of fitting parameters control the data. If the data are closely related to the variable parameters, we can represent the whole curve just by fitting parameters. Second, mathematical fitting can help researchers distinguish the issues that result from experimental errors and identify data trends. Third,

mathematical equations can be used to derive theoretical implications relating variables to one another. Mathematical expressions are a good starting point for such calculations. Moreover, fitting expressions can also be used for predictions, unlike experiments. In other words, curve fitting is a powerful tool for analyzing the experimental data.

In order to represent experimental data using a model based on mathematical equation, the emission and excitation spectra of the CNPs were analyzed and fitted by statistical software, Qtiplot. With the correct mathematical model, we could determine important characteristics of emission and excitation spectra, such as the shape of the curve, the peak location, the amplitude of the curve, and the full width at half maximum (FWHM). After calculations, the results showed the R squared was higher than 0.97. This result indicated that these parameters are the coefficients of the emission and excitation spectra. All results are shown in Chapter 5 and the Appendix.

3.3.1 Model selection- emission spectrum fitting

In this project, Gumbel distribution was selected for the emission spectra. The mathematical expression of the Gumbel distribution can be written as

$$y = Ae^{(-z+1-e^{-z})} + y_0$$

$$z = \frac{x - XC}{S}$$

$$z \in \mathbb{R}$$

where, four parameters are:

$$A: \text{Intensity}$$

$$XC: \text{peak center location}$$

$$S = \text{peak scale}$$

$$y_0 = \text{offset}$$

The Gumbel distribution profile is shown in Figure 3-7.

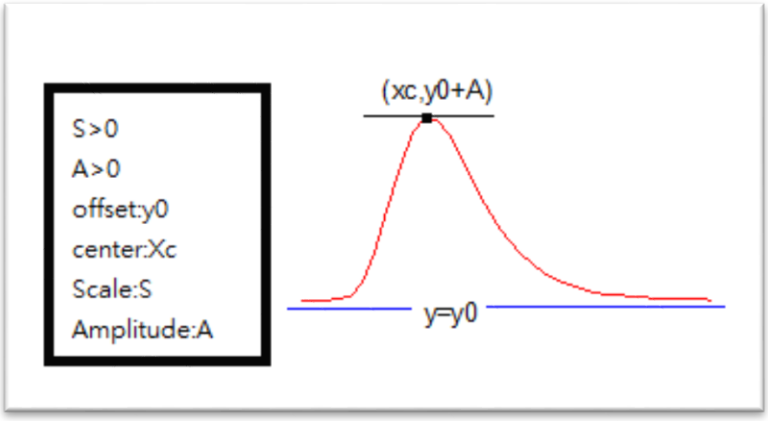

Figure 3-7. Gumbel distribution profile. The equation is presented in Section 3.3.1 The parameters of peak centers, amplitudes, and scale can be defined and quantified mathematically.

In probability and statistical theory, Gumbel distribution is one type of extreme value theory. It is unbounded and defined on the entire real axis. Extreme value theory (EVT) is a separate branch of statistics that deals with extreme values or rare events. In other words, this distribution model measures a limited number of distributions with maximum and minimum values that occur with very small probability in a given sample of a given random variable. If the distribution of underlying sample data is of the normal or exponential type, Gumbel distribution can be used to represent the distribution of maximal values according to EVT. Gumbel distribution is widely used in modeling

engineering problems, in particular modeling of meteorological phenomena such as annual flood flows.

Several mathematical parameters were defined by the Gumbel function, including the peak center, Xc, which was the mean of the peak and presented maximal amplitude in the position. Scale, S, was related to standard deviation of spectra width. Amplitude was the intensity of the emission spectrum. y0 was the offset of the spectrum.

In this work, emission spectrum curves were fitted with Gumbel distribution. The R squared was over 0.98, which means the spectra data strongly matched the probability of the Gumbel distribution function. All of the fitting results are listed in Chapter 5.

3.3.2 Excitation spectrum fitting

Different from emission spectra, excitation spectra were fitted with the Gaussian distribution and Lorentz distribution, For Gaussian distribution, the equation is written as

$$\mathrm{y} = \mathrm{Ae}^{-\frac{(\mathrm{x}-\mathrm{XC})}{2\mathrm{w}^2}} + y_0$$

where,

$$\mathrm{A} = \mathrm{Intensity}$$

$$\mathrm{XC} = \mathrm{peak\ center\ location}$$

$$\mathrm{w} = \mathrm{half\ width}$$

$$y_0 = \mathrm{offset}$$

Four parameters were also defined, intensity, including peak center location, peak intensity and peak widths. For the Lorentz distribution, the equation can be written as

$$\mathrm{y} = \frac{2A}{\pi} \times \frac{w}{4(X - Xc)^2 + w^2} + y_0$$

where,

$$\mathrm{A} = \mathrm{Intensity}$$

$$\mathrm{XC} = \mathrm{peak\ center\ location}$$

$$\mathrm{w} = \mathrm{half\ width}$$

$$y_0 = \mathrm{offset}$$

All of the fitting results are listed in Section 5.1.2, 5.1.3. and the Appendix.

3.3.3 Experimental parameters definitions

During microwave synthesis, different experimental parameters were recorded for studying the relationship with optical performance. In this section, several of these parameters are defined. The first, temperature, is defined as the highest temperature reached during microwave synthesis. In this project, the maximum temperature ranges from 89 to 123℃. The second, heating power, also termed as "the energy delivery rate," is the amount of energy consumed per unit time of CEM microwave. In other words, power is the rate at which the CEM microwave converts electrical energy into heat. The unit of power is joules per second (J/s), known as the watt. The third, heating time, is how much time the CEM microwave takes to work. The unit is the minute. Finally, the output energy is how much energy the CEM instrument expends in the whole synthesis. The output energy is the product of power multiplied by time and the unit is the joule.

These four parameters were studied in relation to the optical performance of CNPs during microwave synthesis.

CHAPTER IV

PHYSICS ANALYSIS-RESULTS AND DISCUSSION

4.1 TEM image

4.1.1 Image CNPs by TEM image

TEM has the ability to image CNPs. The first step was to calibrate the magnification of the TEM. A standard grid was used to with a magnification of 25 kV.

In TEM images, CNPs presented as globular or oblate nano-particles with diameters between 2 and 50 nm. Representative samples were characterized by TEM and are shown in Figure 4-1 to Figure 4-4. Each sample was analyzed and 50 dots were counted to calculate an average size and distribution. Figure 4-1 shows a TEM image of CNPs from a 10w5m (100 Watts power and 5 min heating time) synthesis. The small particles appear to be amorphous. The average size of 100w5m was 2.73 nm with a fairly uniform size distribution. Figure 4-2 shows a TEM image of CNPs from a 150w10m synthesis. The average size was 5.03 nm and the structure was still primarily amorphous but some lattice structures could be observed with a lattice spacing of 0.29 nm. The size distribution was broader than that of CNPs from the 100w5m synthesis. Figure 4-3 shows a TEM image of CNPs from a 300w5m synthesis. The average size increased to 7.64 nm and the size distribution was significantly broadened. The lattice space was still 0.3 nm. The CNPs in 150w10m and 300w5m had the same structure, but since the particle size was still too small to crystallize, the particles still had an amorphous structure. More information is provided by the diffraction pattern described

in Section 4.1.3. Figure 4-4 shows a TEM image of CNPs from 300w10m and 300w15m syntheses. The size distribution was binomial with many CNPs around 10 nm and some huge particles (larger than 50 nm). Since the particle size distribution was too large to find 50 dots in an image, we did not count particle size or draw a size distribution histogram. For sample 300w15m, the particle size increased to more than 100 nm.

In summary, the CNP samples showed oblate spheroid particles in solution with diameters from 1 to 100 nm. The appearance of CNPs matched results from the literature [9, 11-17]. TEM images of samples indicate that CNP particle size increased with microwave power and time. From the 100w5m to the 300w15m synthesis, the particle size increased from 1 nm to greater than100 nm. The particle size distributions also broadened with increased output power and time. For the 100w5m sample, the particle size were around 3 nm, whereas the 300w10m sample presented two particle size groups, one around 10 nm and the other greater than 50 nm. A lattice spacing in CNPs can be observed in Figure 4-2 and Figure 4-3. The lattice spacing was 0.29 to 0.3 nm in differently sized particle samples and in different experimental runs. The lattice spacing matched literature reports[9, 11-17]. For larger particles in Figure 4-4, lattice structures were not observed. It was possibly because particles were too large, so the lattice layers impeded the transmission of electrons. Studying diffraction patterns by electrons is another way to gain structure information. This information is given in Section 4.1.3.

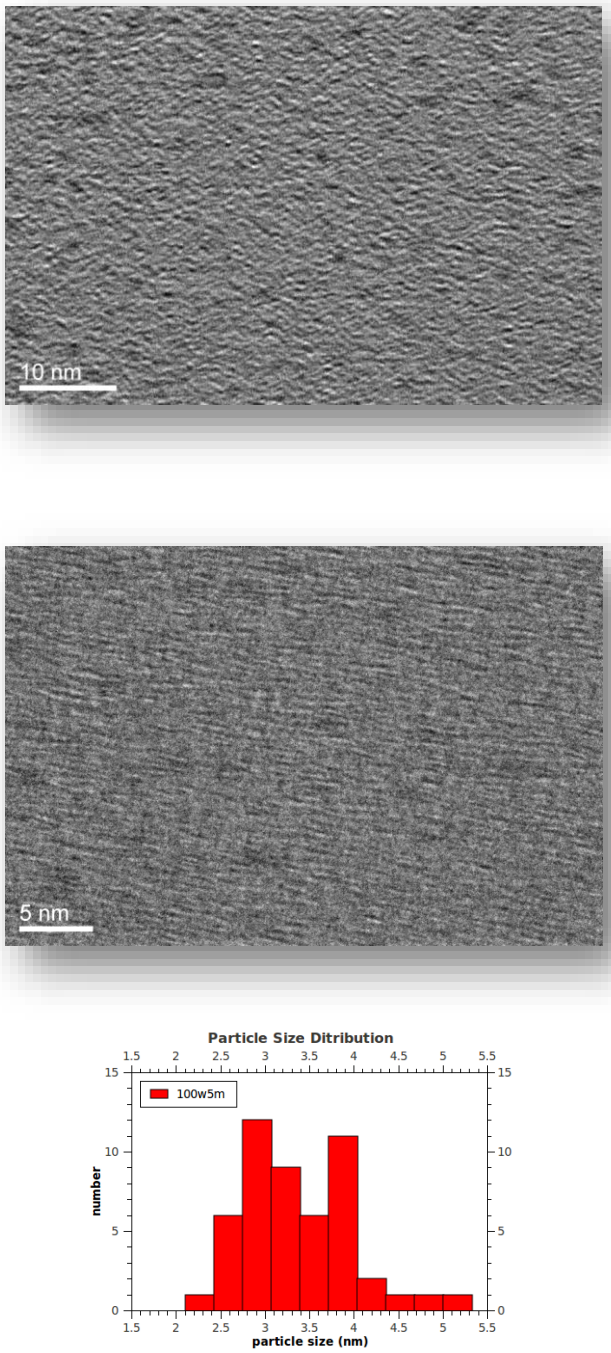

Figure 4-1. TEM image of 100w5m sample. Top: 100w5m sample under 400KX magnification. Middle: sample under 600kX magnification. Bottom: distribution of particle size of 100w5m sample. Fifty particle sizes were counted; the average was 2.7 nm in diameter.

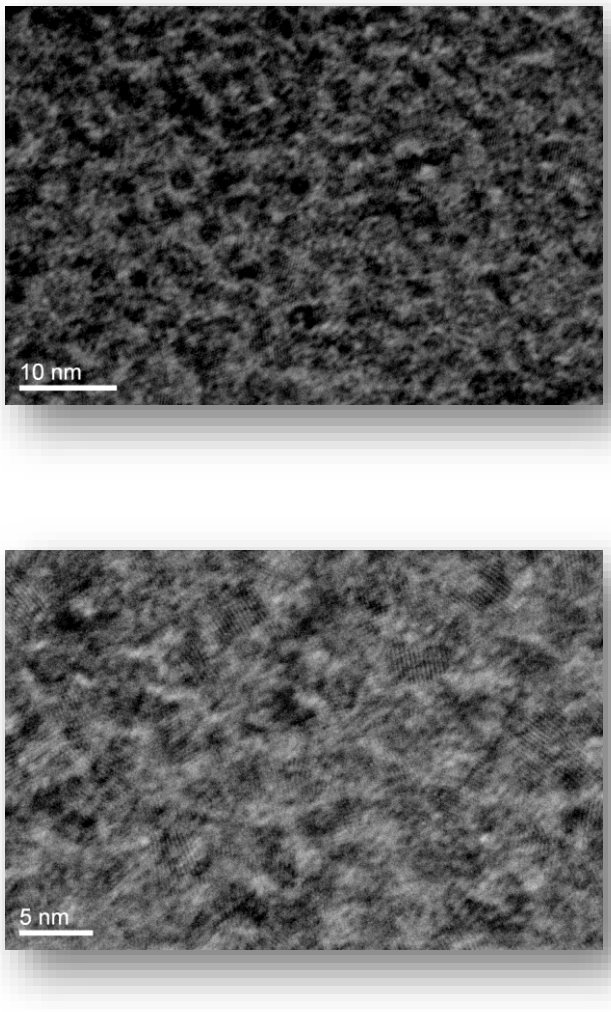

Figure 4-2. TEM image of 150w10m sample. Top: 150w10m sample under 400kX magnification. Middle: sample under 600kX magnification. Bottom: distribution of particle size of 150w5m sample. Fifty particle sizes were counted; the average was 5.4 nm in diameter.

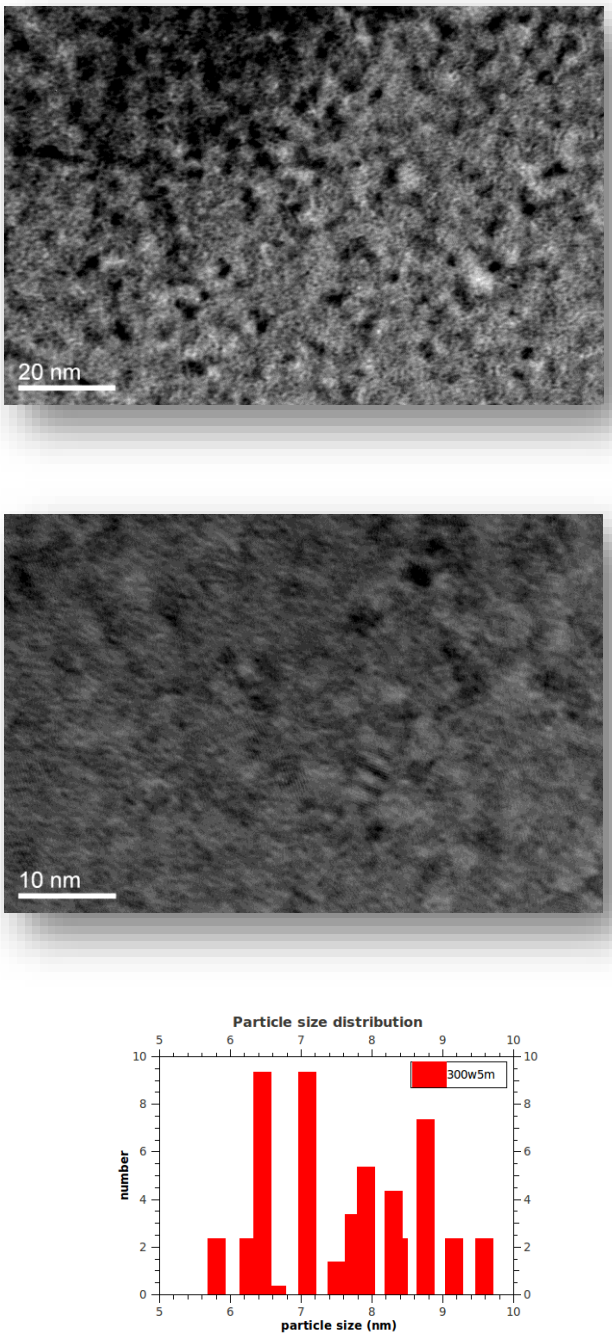

Figure 4-3. TEM image. Up: 300w5m sample under magnification of 200KX. Middle, sample under magnification 400kX. Bottom: distribution of particle size of 300w5m sample. The average of size was 7.8 nm in diameter.

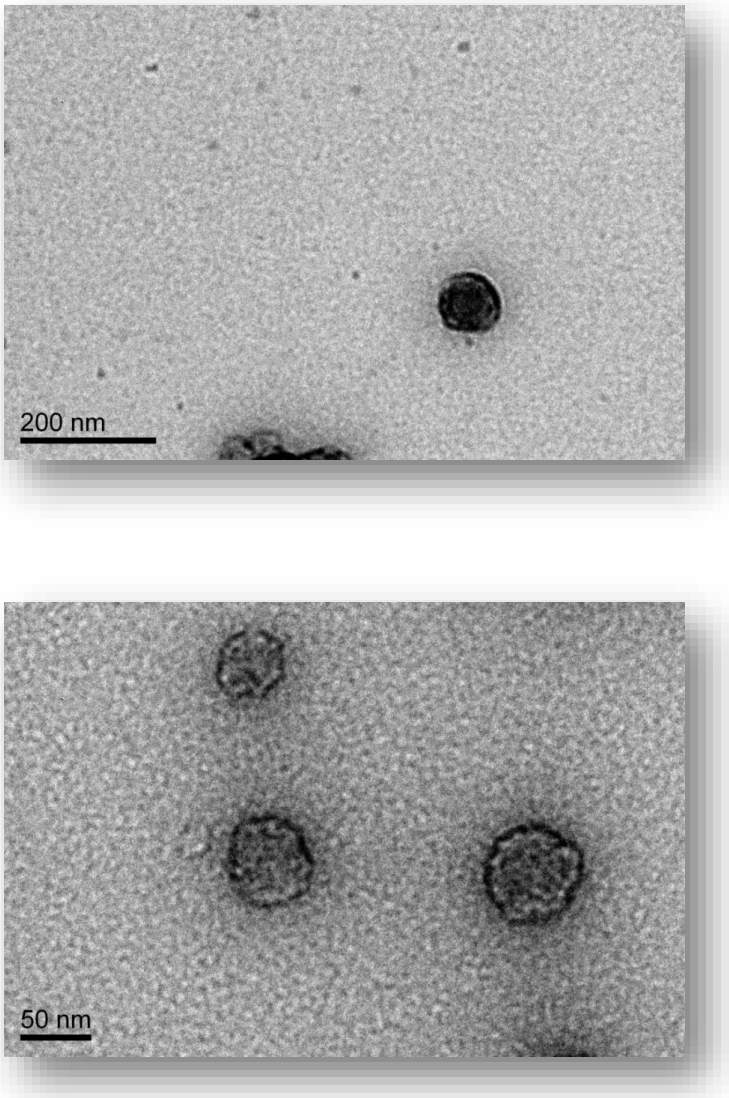

Figure 4-4. TEM image of 300w10m and 300w15m samples. Top: 300w10m sample under 25kX magnification. Middle : 300w10m sample under 50kX magnification. The sample exhibited small particles (10 nm) and huge particles (up 50 nm). Since the particle size distribution was too large, we did not calculate particle size and distribution. Bottom: 300w15m sample under 2500X magnification. Huge particles larger than 100 nm were observed.

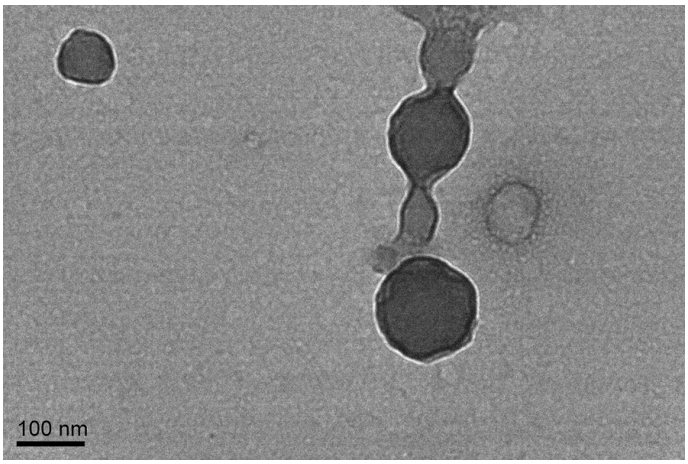

Figure 4-4. continued

4.1.2 Energy dispersive spectrometer (EDS) provides compositions of CNPs

TEM is equipped with an EDS for elemental analysis and chemical characterization. EDS provides chemical analysis of the field of view or spot analyses of particles. In Figure 4-5, elemental analysis was performed on the 150w5m sample. Carbon made up the majority of the CNPs, 96.47 %, and oxygen was the next most plentiful element at 3.53 %. Since EDS could not detect hydrogen atoms, the atomic ratio of carbon and oxygen atoms was close to 24:1. This result showed the CNPs were hydrocarbon products, which means they are an organic compound consisting almost entirely of hydrogen and carbon, with a few oxygen atoms.

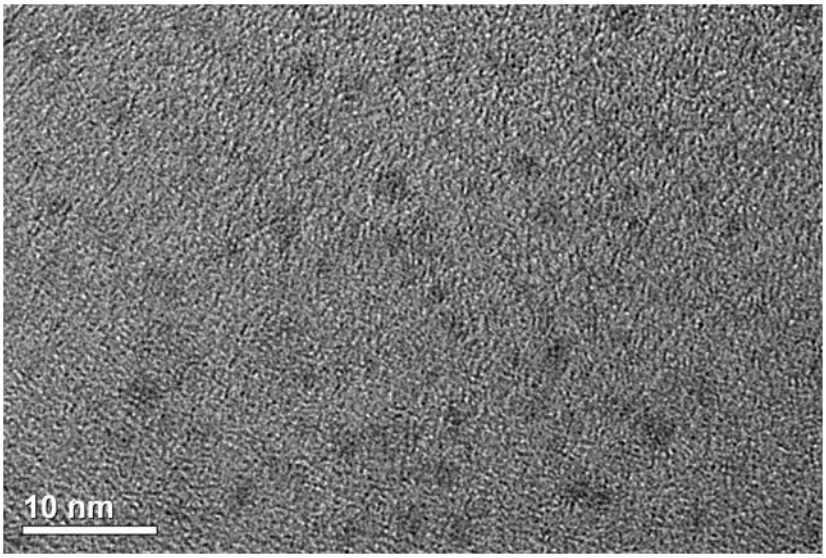

Figure 4-5. EDs detection region of 150w5m sample. The result are presented in Table 4-1. Only Carbon and Oxygen elements were detected.

Table 4-1. Element analysis of 150w5m sample by EDS

Element	Weight%	Atomic%
Carbon	95.35	96.47
Oxygen	4.65	3.53

4.1.3 Electron diffraction pattern of CNPs

Electron diffraction was used to provide more structural information about the CNPs. An accelerated electron beam was able to pass thought the CNPs and make a diffraction pattern. Figure 4-6 shows an image of a CNP with an 18 nm diameter from the 300w5m sample and its diffraction pattern. The rings in the pattern were too dim to observe, but still had some weak lattice signals. This diffraction pattern showed the

particle was of amorphous structure, but since lattice signals could still be observed, the particles were in the early crystalline stage.

An amorphous structure is essentially a random structure. Although it may contain small groups of atoms arranged in an orderly manner, it does not contain long-range order between atoms. Typical amorphous materials include glass and almost all organic compounds.

The structure of some big particles was also examined by electron beam. Figure 4-7 shows another CNP which was 74 nm in diameter in the 300w15m sample. Three clear rings were observed in the pattern. The ratios of the distance of rings were 1:1.47:1.71. The second ring was close to plane (105) and the third was close to plane (108). The outer ring resulted from plane (110). Those crystal planes did not match the carbon crystalline plane composited of carbon single crystal, it was due to there are different anisotropic small crystals or grains in the particle. Therefore the structure exhibited a polycrystalline structure.

4.1.4 TEM imaging exhibited CNPs aggregated after aging

After six months, a CNP sample was re-imaged by TEM. Figure 4-8. shows a TEM image of CNPs from the 150w5m sample. These CNPs were found to aggregate and form linear carbon materials. It implied that the CNPs had the ability to polymerize. However, the polymeric CNPs still presented the same color of fluorescence.

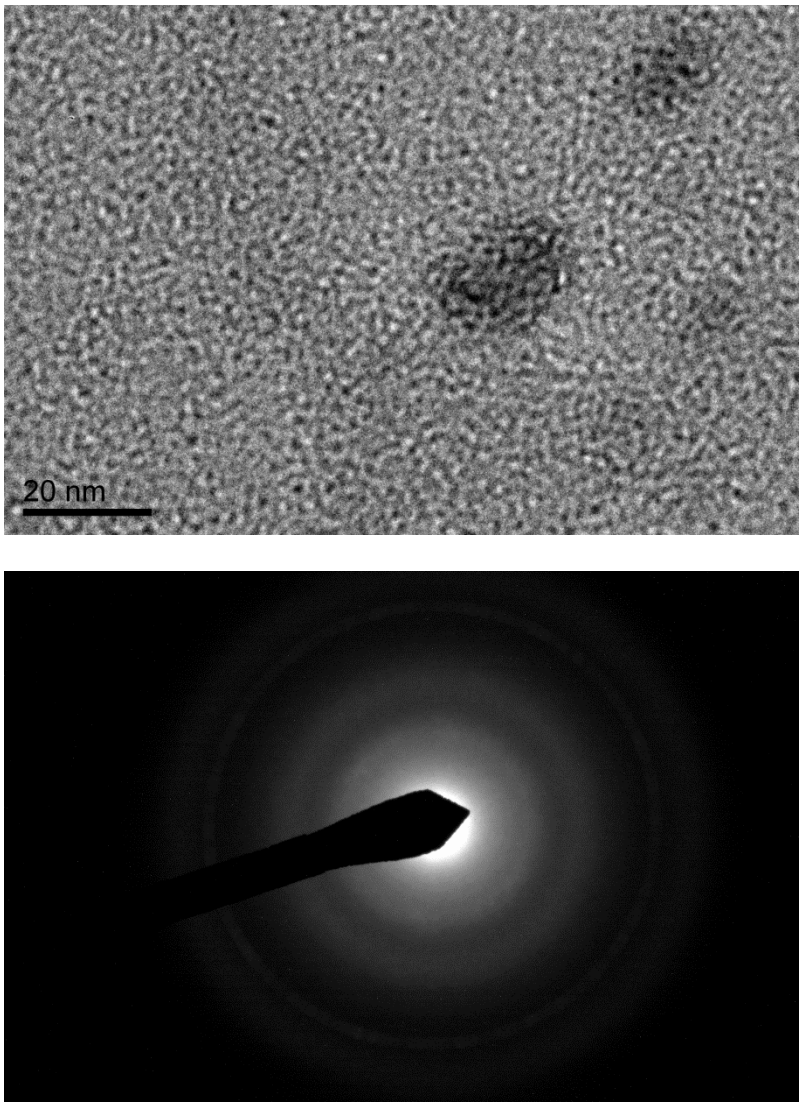

Figure 4-6. TEM image and diffraction pattern of 300w5m sample. An electron beam passed through the particle which had a diameter of 18 nm in the right center and a diffraction pattern. The pattern showed dim rings so the structure was amorphous, but started to crystallize.

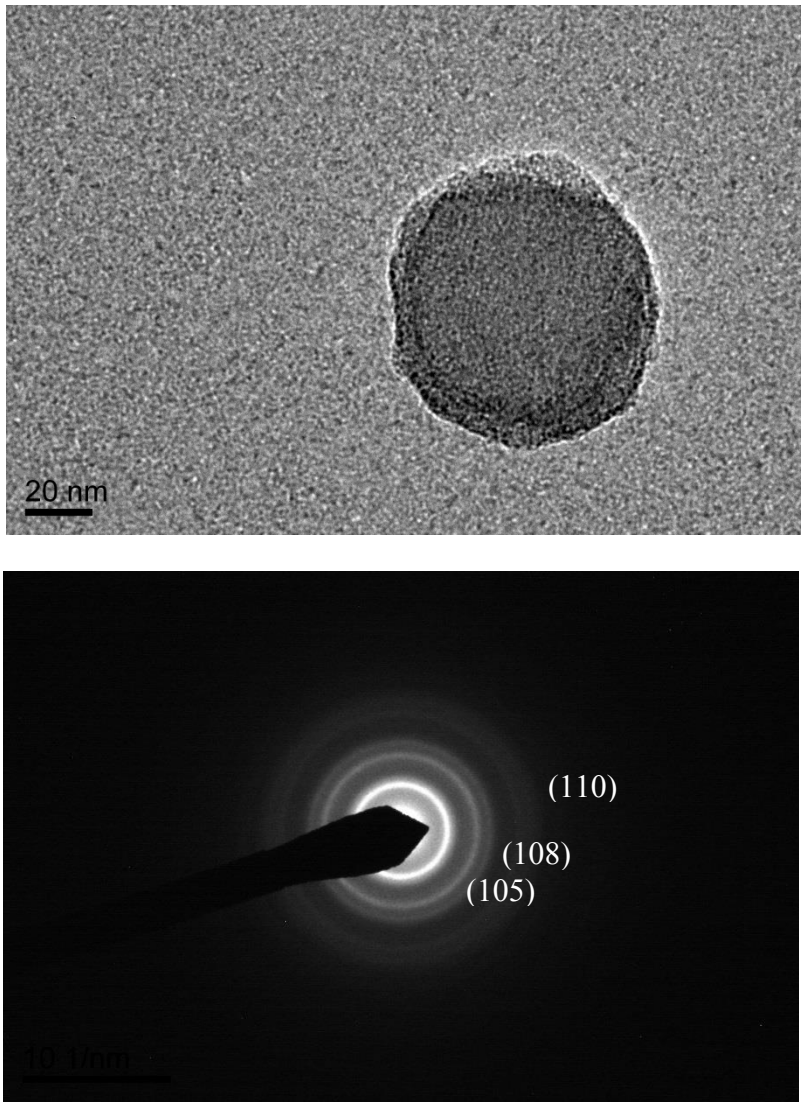

Figure 4-7. TEM image of large particle of CNP and its diffraction pattern in 300w15m sample. The particle size was over 70 nm in diameter.Three clear rings were observed. The ratios of distances of rings were 1:1.47:1.71, which come from planes (1 0 5), (1 0 8), and (1 1 0), respectively. The pattern shows the polycrystal structure of the particle.

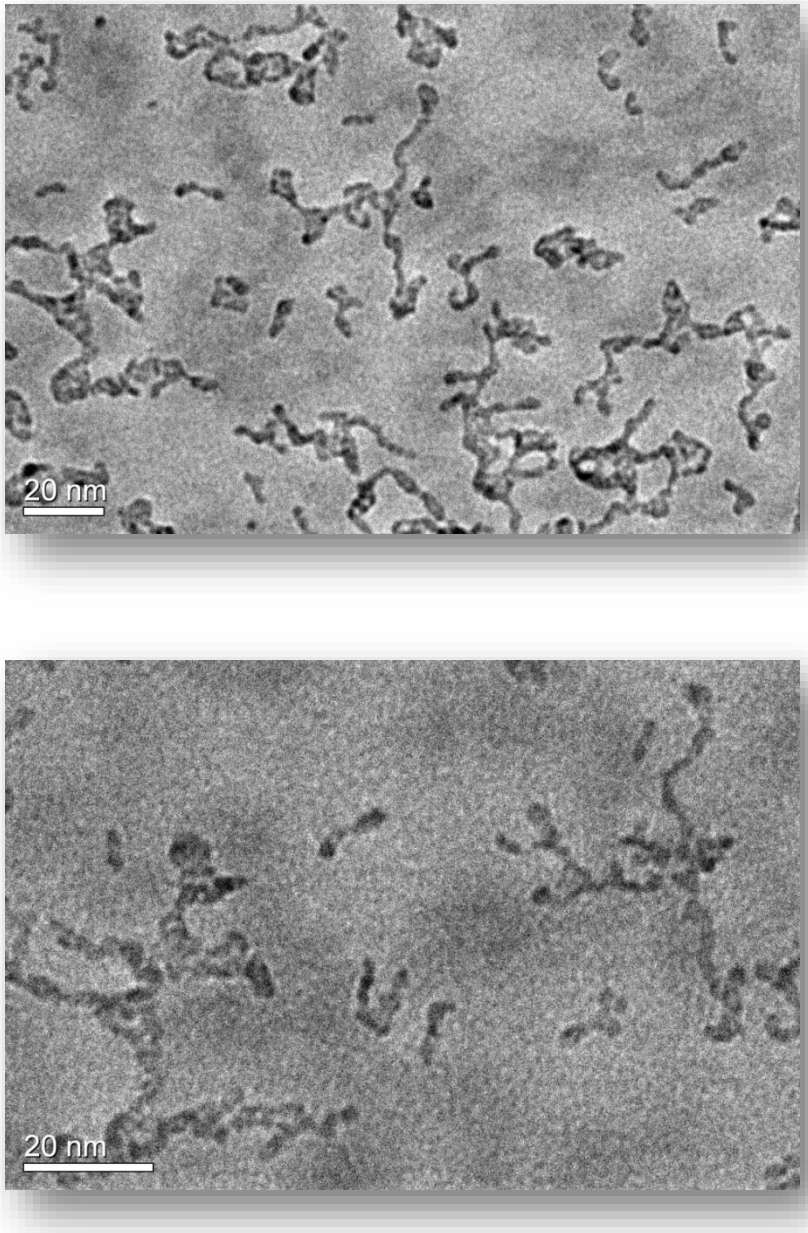

Figure 4-8. TEM image of 150w5m sample after aging for six months. The particles connected together to form linear carbon materials. However, the samples still presented the same fluorescent color, implying CNPs have the ability to polymerize.

4.1.5 Summary and discussion of TEM results

TEM yielded several observations about CNP synthesis. When microwave output power and time increased, the particle size also increased. Particle sizes ranged from around 1 nm to 100 nm. The particles were hydrocarbon products that may have resulted from the aggregation of glucose or glucose derivative. When particle size was around 2 nm, particles were amorphous. When size increased to 5-7 nm, some lattices were built but the overall structure was still amorphous. For particles larger than 50 nm, global particles had a polycrystalline structure. Increasing energy during microwave synthesis promoted CNP nucleation and growth.

Negative staining was used to prepare TEM samples in order to get higher resolution. However, when we observed the image of CNPs, small particles were not surrounded by staining rings. The negative staining method evidently does not work for small particles. For particles larger than 50 nm and linear carbon materials in Figure 4-8, a clear staining ring surrounded the CNPs. Therefore, we assume the negative staining method can only be applied to larger particles.

4.2 Raman spectroscopy

Raman spectra were studied to identify CNP structure and bonding type. Selected Raman spectra of samples are presented in Figure 4-9 and Figure 4-10. The Raman peaks from the CNPs were encased together, which implies there are several different bonding mechanisms and CNPs may interact with water. Several papers reported Raman spectra of carbohydrates affected by product concentrations and wavelength of the excitation laser [33, 34]. Since several types of bonding or even several products were

produced during the microwave synthesis, identifying a single bonding in our Raman spectra was not possible. However, some stronger peaks and bonding type spectral regions could be defined; these peaks gave us some structural information.

In Figure 4-9, the Raman spectrum of glucose solution before microwave synthesis is presented as a reference. All Raman spectra could be separated into two types. In one group, the samples presented almost the same spectrum as the glucose solution. These samples included CNP solutions from the 100w5m, 150w5m, 200w5m, 250w5m, 300w5m, 100w10m, 150w10m, 200w10m, 100w15m and 150w15m synthesis processes. Selected spectra of these samples are presented in Figure 4-9. In the second group, Raman peaks increase or decrease with output energy compared with the spectrum of glucose solution as shown in Figure 4-10. These spectra included samples from the 250w10m, 300w10m, 200w15m, 250w15m, and 300w15m synthesis processes. Literature results were consulted to understand the meaning of the peaks and bonding types [33, 34].

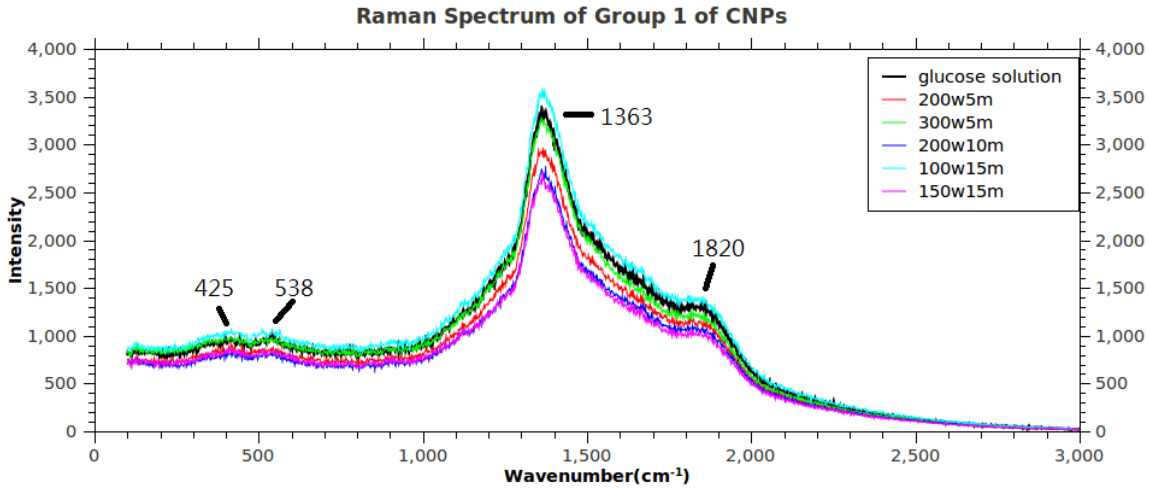

Figure 4-9 . Raman spectrum of Group1 of CNPs. Black line is spectrum of glucose solution. The CNP sample exhibited a similar spectrum with glucose solution.

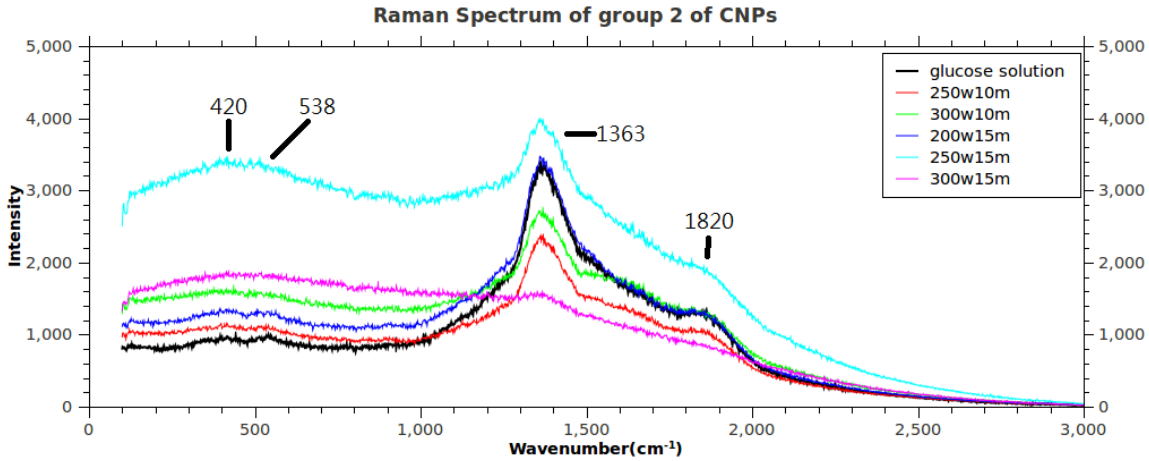

Figure 4-10. Raman spectrum of Group 2 of CNPs. Black line is glucose of glucose solution. The intensity of low wavenumber region increased with input energy until 250w15m. The 300w15m sample showed lower intensity in low wavenumber region and of peak in 1363cm^{-1}.

4.2.1 Low wavenumber region, 200-600 cm^{-1} region

In the low wavenumber range, the skeletal vibration motion is evident, including δ(C-C-C), δ(C-C-O) , δ(C-O), and π(C-C) modes. The spectrum from the glucose solution showed a strong peak at 425 cm^{-1} from the δ(C-C-O) modes. Another significant peak could be defined at 538 cm^{-1} and was contributed by the δ(C-C-C) mode. In the first group, all spectra showed these two peaks, implying there are two bonding mechanisms in the particles. In the second group, the peak of the signals at these wavenumbers increased with output energy, which implies the amount of δ(C-C-C) and δ(C-C-O) increased.

4.2.2 820-950 cm^{-1} region

The spectral range 820-950 cm^{-1} is part of a region referred to the anomeric region. Researchers usually use the peaks in this region to distinguish between α-glucose and β-glucose. This region contains contributions from vibrations of ν(C-O), δ(C-C-H), ν(C-C) and δ(C-C-O) modes. However, in this region, all the spectral of CNPs were encased together and no significant peaks could be distinguished.

4.2.3 1000-1200 cm^{-1} region

The spectral range 1000-1200 cm^{-1} has been suggested [34] to be dominated by contributions from ν(C-C) and ν(C-O) stretching vibrations. δ(C-O-H) motions are also in this region. Unfortunately, in this region, all peaks were encased together, and no peak could be identified.

4.2.4 1200-2000 cm^{-1} region

The δ(C-C-H), δ(O-C-H), and δ(C-O-H) vibrational modes dominate the Raman spectrum in the 1200-2000 cm^{-1} range. For all Raman spectra of CNPs, significant peaks are shown at 1363 cm^{-1}. This D band signal results from vibration of disordered carbon atom with dangling bonding [12, 21]. Usually it can be observed on the edge of graphene. The D band peak in CNPs solution presented CNP including disorder aromatic structure in sp2 carbon system. The other specific peak of graphene reported in the literature is the G-band, which is located at 1583 cm^{-1}. The G band results from vibration of sp2 bonding of carbon atoms in a 2D hexagonal lattice of graphite cluster or graphene sheet. However, in our Raman spectrum of CNPs, the G-band could not be identified since the peaks were encased together. Another significant peak in our Raman spectrum located at 1820 cm^{-1} could be attributed to the ν(C=O) or ν(C=C) mode. All CNP samples had significant signals in 1363 and 1820 cm^{-1} regions except the 300w15m sample.

4.2.5 Summary of Raman spectrum

Raman spectra of CNP samples were studied. Raman peaks were generally encased together, making it difficult to define the single bonding mechanisms. However, the Raman spectra indicated there was carbon hydrated bonding. The Raman spectra exhibited high intensity at 1363 and 1820 cm^{-1} and lower intensities at 425 and 538 cm^{-1}. The 1363 and 1820 cm^{-1} peaks implied that the structure of CNPs contained ring structure or disordered aromatic structure in the sp2 carbon system.

CHAPTER V

OPTICAL PERFORMANCE -RESULTS AND DISCUSSION

5.1 Emission spectrum and excitation spectrum

5.1.1 Emission spectrum

To study the fluorescent properties of CNPs, specific wavelengths were selected to excite the samples at 40 nm increments (340, 380, 420, and 460 nm) of lasers. For all CNP samples, emission spectra consisted of a broad peak across the near-UV and visible regions. Each sample exhibited red-shift emission spectra with different excitations. For CNPs synthesized with lower output energy, the optical performance was high excitation in the UV region and high blue emission in the range from 400 nm to 500 nm. For CNPs synthesized with higher output energy, the optical performance showed a different behavior. High excitations were in the blue visible region and high emissions crossed from500 nm to 700 nm. Typical examples are shown in Figure 5-1 to illustrate this phenomenon. For the 150w5m sample, the emission spectrum ranged from 380 to 650 nm, and for the 250w15m sample, the emission spectrum ranged from 480 to over 700 nm. The 150w5m sample had high absorption in the UV region and high emission crossing from 400 to 500 nm, but low absorption in visible light and emission in the region of 500 to 700 nm. The 250w15 sample showed the opposite optical performance. It had high absorption in the visible region and emission between 500 and 700nm, but poor absorption in UV light and emission between 400 and 500 nm.

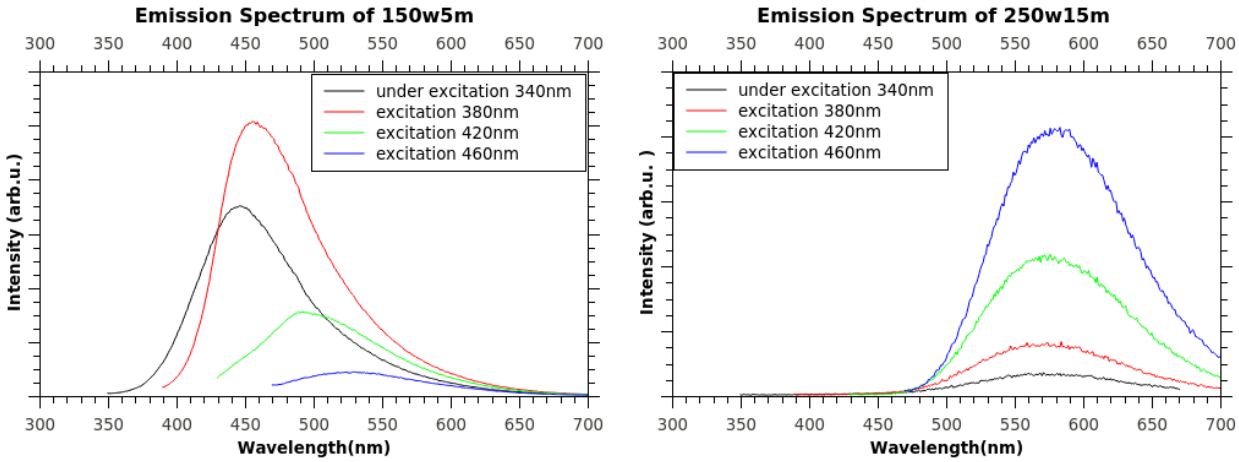

Figure 5-1. Emission spectrum of 150w5m (left) and 250w15m samples (right). Each sample was excited by four different wavelengths of lasers, which were in the UV region (340 and 380 nm) and in the visible region (420 and 460 nm). For the 150w5m sample, the emission spectrum ranged from 380 to 650 nm and high emission crossing from 400 to 500 nm. For the 250w15m sample, the emission spectrum ranged from 480 to over 700 nm and high emission between 500 and 700 nm.

In Figure 5-1, the 150w5m sample (left) excited at 340 nm exhibited a dark blue emission spectrum from 380 nm to 650 nm and centered at 446 nm. The same sample excited at 420 nm exhibited a light blue emission spectrum from 450 nm to 650 nm and centered at 489 nm. The emission exhibited a red shift with red shifted excitation. Moreover, the emission excited with 340 nm had stronger intensity than that excited with 420 nm. For the 250w15m sample, the optical performance was opposite to that of the 150w5m sample. The 250w15m sample (right) excited at 340 nm exhibited a yellow emission spectrum from 480 to 650 nm and a center located at 581 nm. When excited at 420 nm, the 250w15m sample still exhibited a yellow emission spectrum similar to the 340 nm spectrum. The emission of the 250w15m sample did not red shift with red

shifted excitation, and the emission intensity excited at 420 nm was stronger than that excited at 340 nm.

In other words, the CNPs made by microwave-assisted synthesis under different heating time and output power exhibited different fluorescent colors and emission intensity at different wavelengths. The relation between experimental parameters and emission spectra is analyzed and illustrated in the following sections.

5.1.2 Gumbel distribution and emission spectrum fitting results of the CNPs

To study the emission spectra of CNPs, the emission profile was fitted with a mathematical function. We are the first group to find the emission spectra of all samples can be described by Gumbel distribution; the equation is presented in Section 3.3.1 and the distribution profile in Figure 3-7. Each emission peak was fitted by the equation to define the peak location, peak intensity (amplitude), and peak scale (related to width).

The fifteen CNP samples synthesized under different experimental parameters and excited by four wavelengths (340, 380, 420 and 460 nm) were fitted. Examples of emission spectra fitting are shown in Figure 5-2. In Figure 5-2, spectra from the150w5m and 250w15m samples excited at 340 nm and 460 nm are plotted as block dots. Their fitting curves are plotted as a red line. All mathematical parameters of 15 CNP sample fits are listed in Table 5-1 to Table 5-4, and the fitting curves are listed in the Appendix. The results show R squareds of fitting line were over 0.98 except for the 100w5m sample excited at 460 nm, which means the fitting curves matched the experimental emission spectra.

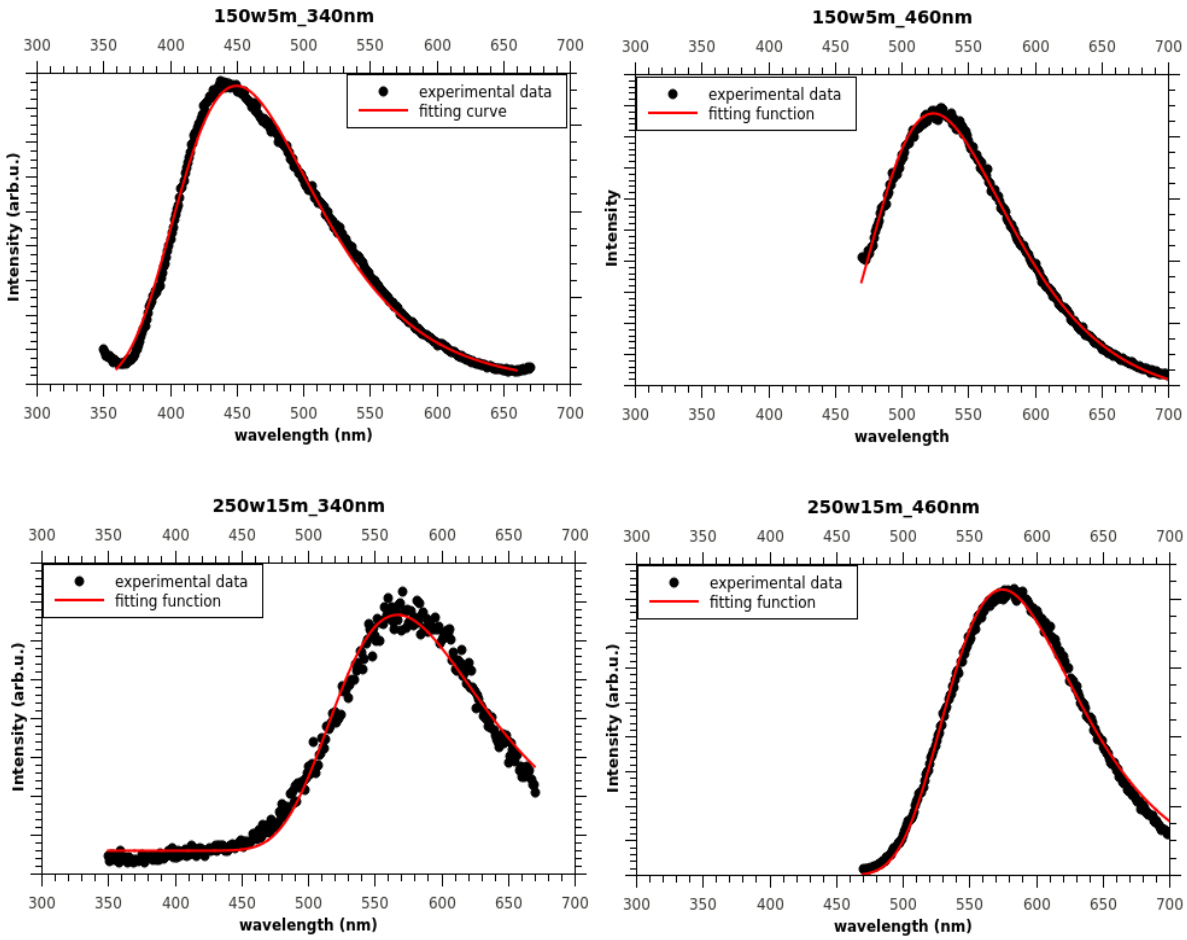

Figure 5-2. Experimental emission spectra and the Gumbel distribution fitting curve. Top: 150w5m sample under 340 nm (left) and 460 nm (right) excitation. Bottom: 250w15m sample under 340 nm (left) and 460 nm (right) excitation.

Tables 5-1 through 5-4. list the fitting parameters and characteristics of the CNP spectra under excitation of 340 nm, 380 nm, 420 nm and 460 nm, respectively. The first column lists sample names and synthesis parameters. The second column shows the fluorescent color of the sample. The third and fourth columns show the values of Xc and S fitting results, respectively. The fifth column shows the R squared, indicating how well

the fit matches the data. The final column presents the intensity or the amplitude of the curve peak. Offsets, y0, were so small compared with the amplitude that they are not included in the tables.

5.1.3 Discussion of emission peaks shift properties

5.1.3.1 Emission centers shifted with increasing excitation wavelength

All emission peaks of CNPs exhibited an excitation-dependent shift, except the 250w15m and 300w15m samples. Figure 5-3 presents normalized spectra of the 150w5m sample as an example. The 340 nm excitation produced a peak centered at 456 nm. When we increased excitation to 380 nm, emission spectra red shifted to 460.4 nm. With increasing excitation wavelength to 460 nm, the emission peak followed the excitation and shifted to a peak center at 529 nm.

Table. 5-1 Samples under 340 nm wavelength of laser and their fitting results.

Sample	Color	Fitting parameters			
		Xc (nm)	S (nm)	R^2	Intensity (arb.u.)
100w5m	Dark blue	449.8	51.24	0.9944	172084
100w10m	Dark blue	447	42.57	0.994	558856
100w15m	Dark blue	449.5	40.75	0.993	624817
150w5m	Dark blue	449.9	51.39	0.994	172402
150w10m	Dark blue	451.9	42.91	0.992	535767
150w15m	blue	475	52.42	0.992	120113
200w5m	Dark blue	449.3	37.67	0.998	789321
200w10m	blue	476.1	53.33	0.992	117331
200w15m	green	512.9	60.46	0.989	15063
250w5m	blue	464.4	47.67	0.991	253781
250w10m	green	524.9	60.54	0.978	9401
250w15m	yellow	567.1	54.83	0.986	6067
300w5m	blue	481.8	54.43	0.994	70632
300w10m	Light green	546.3	55.96	0.982	5870
300w15m	orange	602.7	56.84	0.995	9843

Table. 5-2 Samples under 380 nm wavelength of laser and their fitting results.

Sample	Color	Fitting parameters			
		Xc (nm)	S (nm)	R^2	Intensity (arb.u.)
100w5m	blue	461.9	46.5	0.991	97440
100w10m	blue	462.7	41.33	0.99	522707
100w15m	blue	469.6	44.58	0.993	1081407
150w5m	blue	460.4	34.2	0.996	976787
150w10m	blue	472.6	46.49	0.993	973484
150w15m	light blue	492.4	53.43	0.999	683981
200w5m	blue	462.9	35.83	0.995	1580900
200w10m	light blue	491.9	53.99	0.999	659535
200w15m	green	521.5	54.04	0.995	159548
250w5m	light blue	479.4	47.94	0.994	973102
250w10m	green	531.4	53.09	0.994	93911
250w15m	yellow	565.2	50.66	0.99	15339
300w5m	light blue	494.3	53.1	0.998	556708
300w10m	light green	549.6	51.62	0.99	23239
300w15m	orange	592.8	52.85	0.994	17264

Table. 5-3 Samples under 420 nm wavelength of laser and their fitting results.

Sample	Color	Fitting parameters			
		Xc (nm)	S (nm)	R^2	Intensity (arb.u.)
100w5m	light blue	495.5	45.98	0.995	305994
100w10m	green	507.7	48.2	0.991	210971
100w15m	green	510.1	43.9	0.996	675109
150w5m	light blue	495.5	46.06	0.995	306393
150w10m	green	511.1	44.39	0.996	617471
150w15m	green	520.3	46.09	0.998	952389
200w5m	blue	498.4	46.09	0.996	602611
200w10m	green	519.7	45.53	0.998	910137
200w15m	green	534.7	48.67	0.998	517258
250w5m	green	514.4	46.37	0.997	836758
250w10m	light green	540	48.87	0.998	381497
250w15m	yellow	570	49.62	0.993	42894
300w5m	green	520.6	46.96	0.998	845336
300w10m	light green	554.3	49.23	0.996	121308
300w15m	orange	594.1	51.42	0.992	22196

Table. 5-4 Samples under 460 nm wavelength of laser and their fitting results.

Sample	Color	Fitting parameters			
		Xc (nm)	S (nm)	R^2	Intensity (arb.u.)
100w5m	blue	473.9	-10.63	0.946	13083
100w10m	green	527.4	46.74	0.996	87136
100w15m	green	530.4	46.42	0.999	289651
150w5m	green	523.9	49.47	0.998	92420
150w10m	green	531.2	47.31	0.999	264263
150w15m	green	537.8	47.84	0.999	584335
200w5m	green	526.1	48.24	0.999	193802
200w10m	green	537.1	47.98	0.999	555353
200w15m	Light green	547.5	49.36	0.999	498102
250w5m	green	535	48.35	0.999	410208
250w10m	Light green	551	49.96	0.999	434610
250w15m	yellow	574.8	48.51	0.993	82751
300w5m	green	538.9	48.56	0.999	532091
300w10m	Light green	561.4	49.64	0.996	212399
300w15m	orange	598.8	49.93	0.993	23335

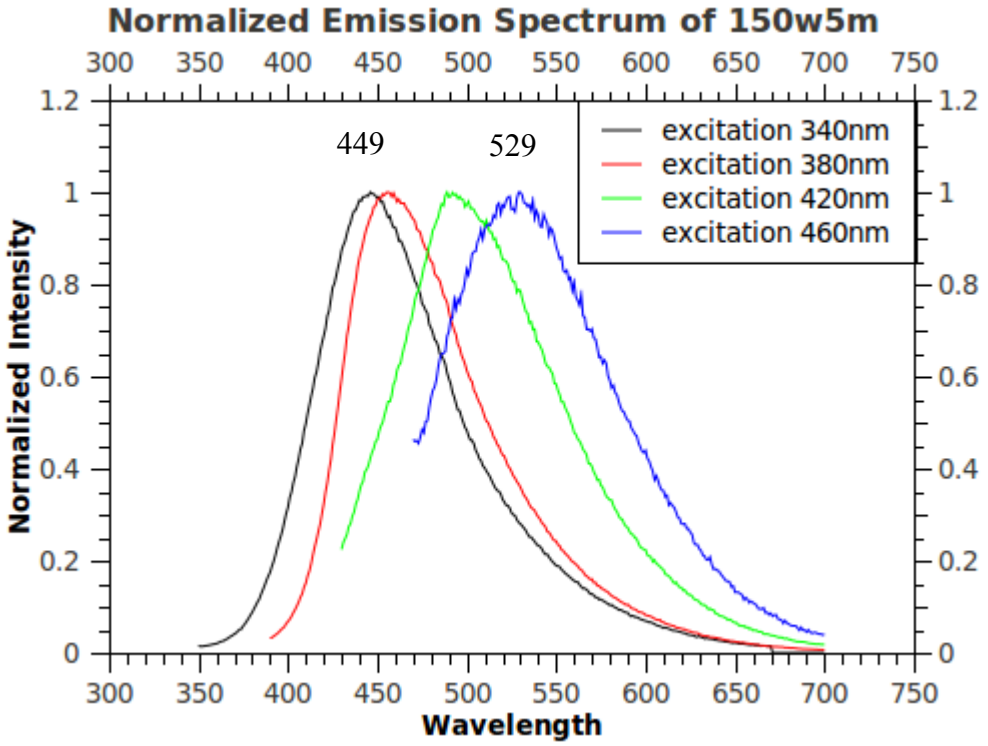

Figure 5-3. Normalized emission spectrum of 150w5m sample. The excitation increased from 340 to 460 nm wavelength and the emission spectral red shift from 449 to 529 nm.

5.1.3.2 Shifting interval of emission peaks decreased with output energy

Samples were excited by four different wavelengths, 340 nm, 380 nm, 420 nm and 460 nm. The shift in emission centers between the four excitation wavelengths was studied. We found the shifting reduce the interval with total output power. For example, Figure 5-4 (top) showed normalized emission spectra for the 100w5m and 300w15m samples. For the 100w5m sample, the shift between emission centers was 17 nm (excitation 340 to 380 nm), 38 nm (380 nm to 420 nm), and 38 nm (420 nm to 460 nm), respectively. However, for the 300w5m sample, the shifting distances reduced to -5 nm

(340 nm and 380 nm), 3 nm (380 nm to 420 nm), and 5 nm (420 nm to 460 nm). Figure 5-4 (bottom) plots the emission centers with excitation wavelength (X-axis was excitation wavelength and Y- axis was emission wavelength). The shift slope was fitted linearly. The slope of the 100w5m sample was 0.708. For the 300w15m sample, the slope reduced to -0.026.

For all CNP samples we calculated the shift slope. As shown in Figure 5-5, we found that samples can be classified into three groups depending on the slope. Samples with slopes between 0.5 and 0.8 included the 100w5m, 100w10m, 100w15m, 150w5m, 150w10m, 150w15m, 200w5m, 200w10m, 250w5m, and 300w5m samples. Samples with slopes below 0.2 included the 300w10m, 250w15m and 300w15m samples. The 250w10m and 200w15m samples were in the transition region between these groups (0.5 to 0.2). Higher slope samples were concentrated in the lower output energy region, and lower slopes were concentrated in the higher output energy region. When the CNPs were manufactured with lower output energy, the distribution of emission peaks was wide. With increasing output energy, the slopes decreased and the shifting of emission peaks narrowed.

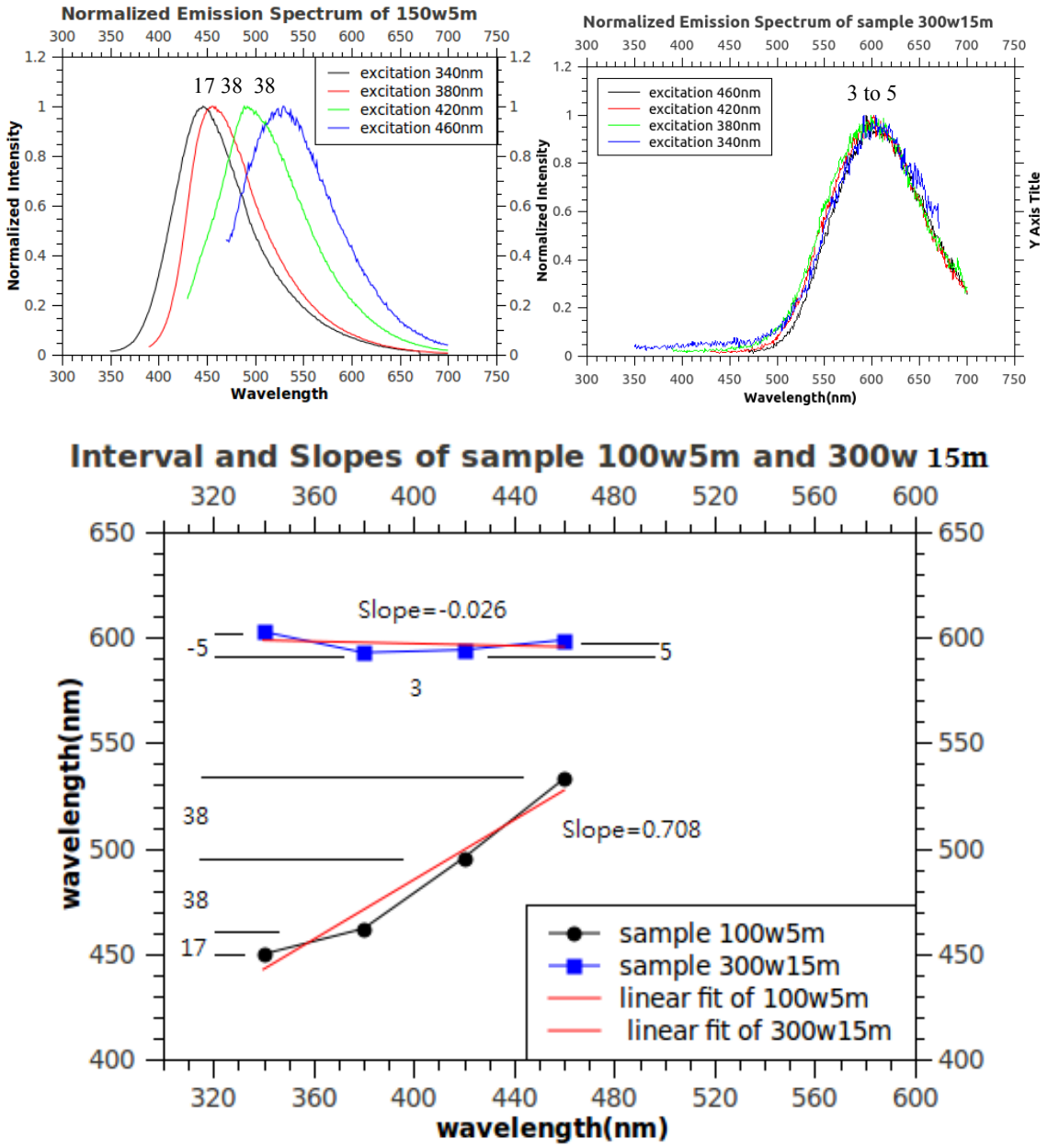

Figure 5-4. The emission spectrum of 100w5m and 300w15m. The shifting interval and their slope were calculated. For the 100w5m sample, the shift between excitations was 17, 38, and 38 nm. The slope was 0.708. For the 300w15m sample, the shift between excitations was 3 to 5 nm. The slope was -0.026.

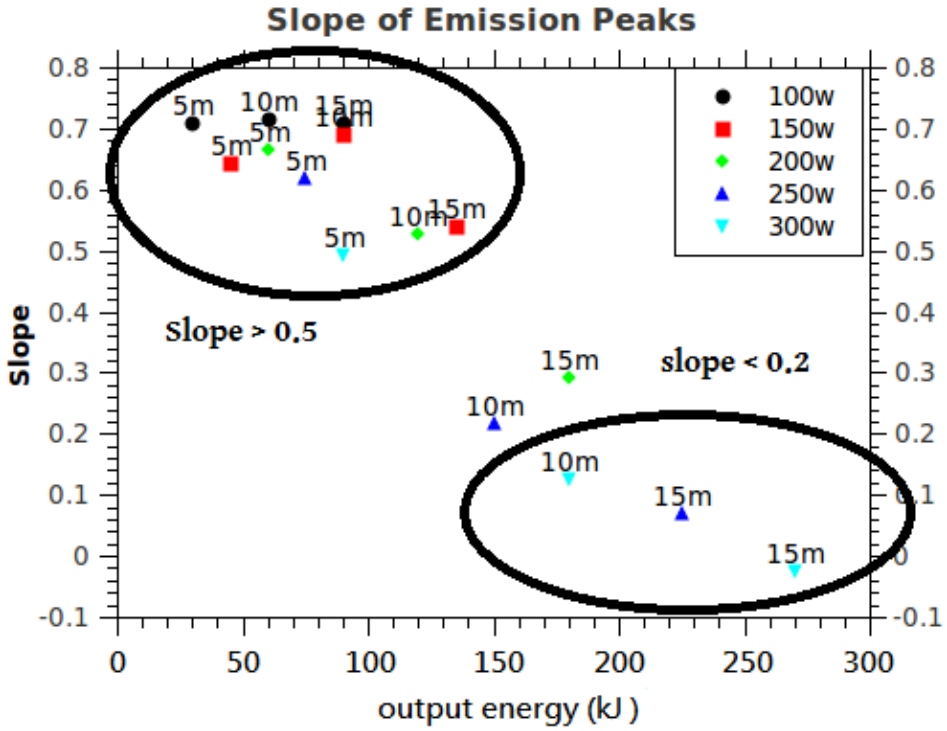

Figure 5-5. Slope of shifting emission peaks. CNPs produced with lower output energy had a higher slope, which meant the emission peaks were widely distributed. CNPs produced with higher output energy had lower slopes, which meant the emission peaks were narrowly distributed.

5.1.3.3 Raman and emission spectral slope imply different product steps

Section 5.1.3.2 and Figure 5-5 show emission center peaks plotted with excitation and the slopes can be classified in three groups: between 0.5 and 0.7, below 0.2, and in a transition region between 0.2 and 0.5. The same tendency could be observed in Ramam spectra. For the group with a slope from 0.5 to 0.7, the Raman spectrum showed high intensity at 1363 cm^{-1} and small broad peaks at 425 and 538 cm^{-1}. For the group with a

slope below 0.2, the Raman spectra showed high intensity at 425 cm^{-1} and 538 cm^{-1}, The 200w10m and 150w15m samples are the transitional group between higher and lower slopes. When the slope of emission position decreased, we found peak intensity at 1363 cm^{-1} also decreased and the peak intensity at 425 cm^{-1} and 538 cm^{-1} increased. Therefore, we could define the process steps by the slope of emission position and the ratio of 1365 cm^{-1} and 388 cm^{-1} peak intensity.

5.1.3.4 Emission centers shifted with increasing total output energy

In order to demonstrate that the microwave-assisted synthesis method produced CNPs with tunable emission properties, the impact of the experimental process and the relationship between experimental parameters and emission peaks were studied, including the heating temperature, heating time, and output energy. The time and power could be functions of output energy. We found the emission spectra shifted linearly with output energy. Figure 5-6 shows the centers of emission spectra as black circles, plotted against output energy for all excitation wavelengths. The data shown in Figure 5-6 (a) were fitted to 340 nm excitation emissions with a line with a slope of 0.00068 and intercepted at 408.17 nm, yielding an R squared of 0.9073. Figure 5-6 (b) was fitted to 380 nm excitation emissions with a linear fitting line with a slope of 0.00059 and interception at the y-axis at 430.25 nm. Figure 5-6 (c) was fitted to 420 nm excitation emissions with a linear fitting line with a slop of 0.000 4 and interception at the y-axis at 478.14 nm. Figure 5-6 (d) was fitted to 460 nm excitation emissions with a linear line with a slope of 0.00028 and interception at the y-axis at 510.3 nm. All centers of emission exhibited a linear red-shift property with output energy.

(a.)

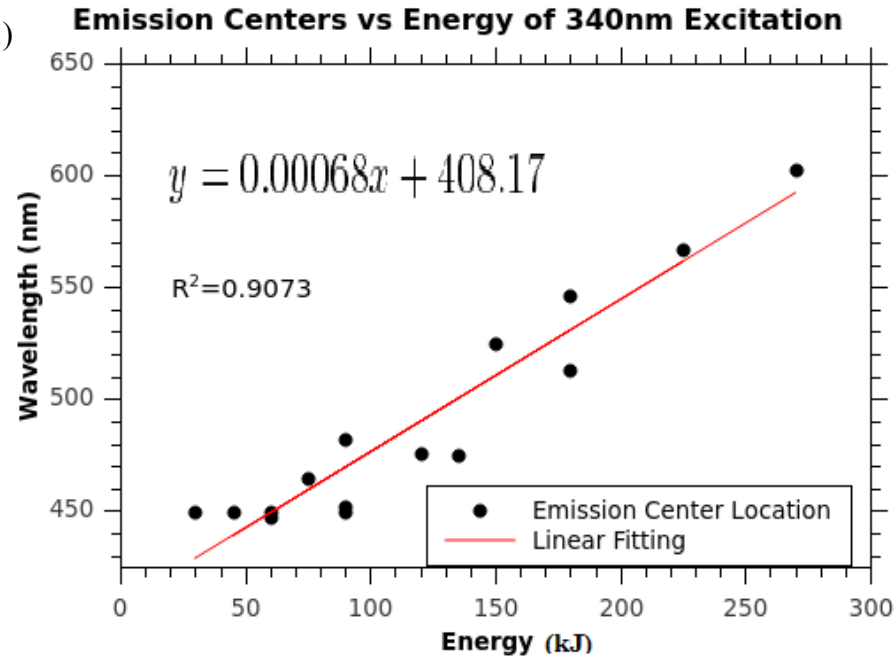

(b.)

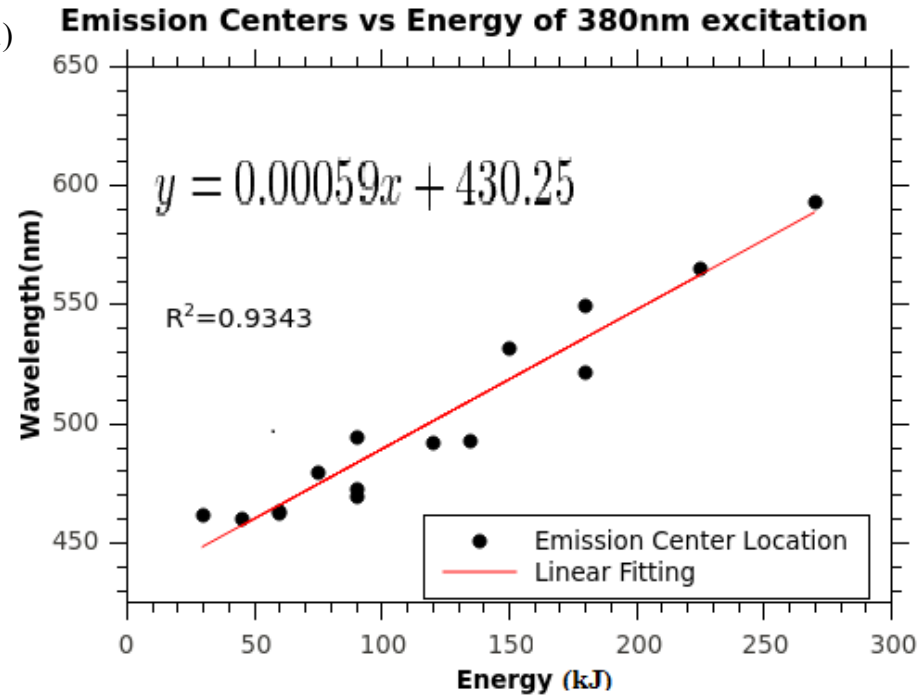

Figure 5-6. Emission peak locations plotted with output energy and fitting line (red). (a) emission spectra obtained by exciting 340 nm wavelength. (b) emission spectra obtained by exciting 380 nm wavelength. (c) emission spectra obtained by exciting 420 nm wavelength. (d)emission spectra obtained by exciting 460 nm wavelength. The emissions centers showed a linear increase with output energy.

(c.)

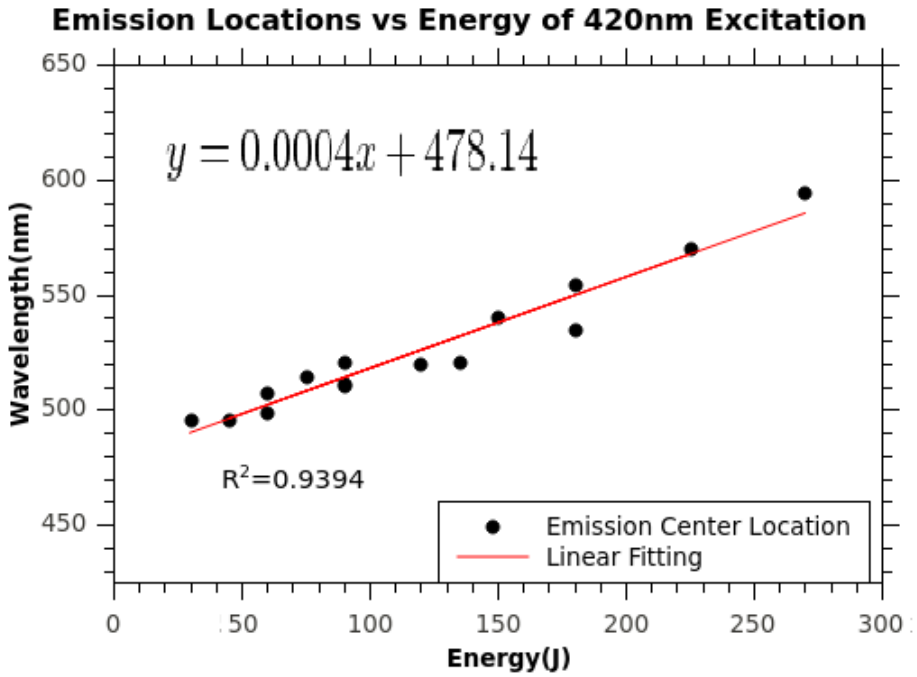

(d.)

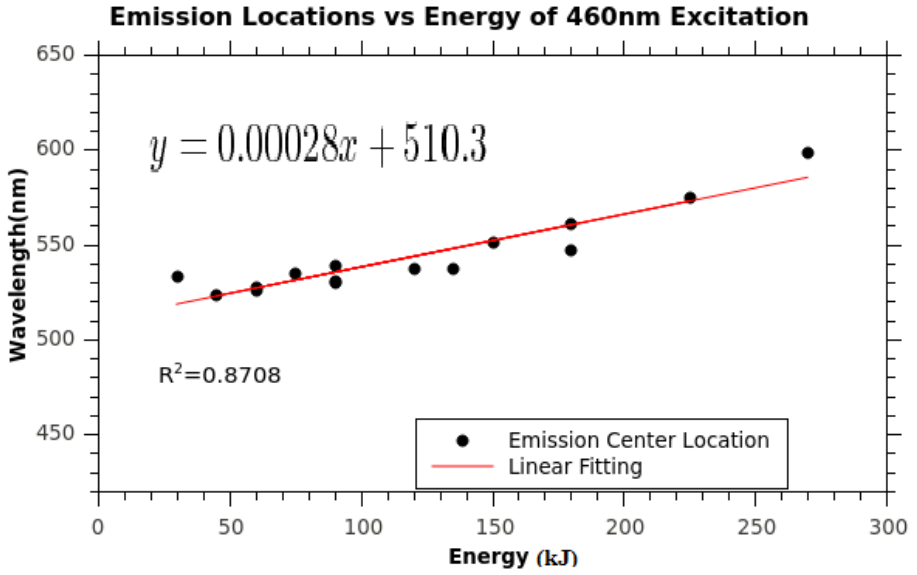

Figure 5-6. Continued.

Figure 5-6 shows that CNPs exhibited a linear dependence on output energy. Figure 5-7 shows all emission centers and the four linear fitting lines together. We found all the line fits intersected with each other. Table 5-5 lists the intersection points of each pair of fits. The intersection points located in the 575 to 585 nm range had output energy ranging from 245 kJ to 268 kJ. This indicates that CNPs produced in the 245 kJ to 268 kJ range of output energy have roughly the same emission spectra centers,

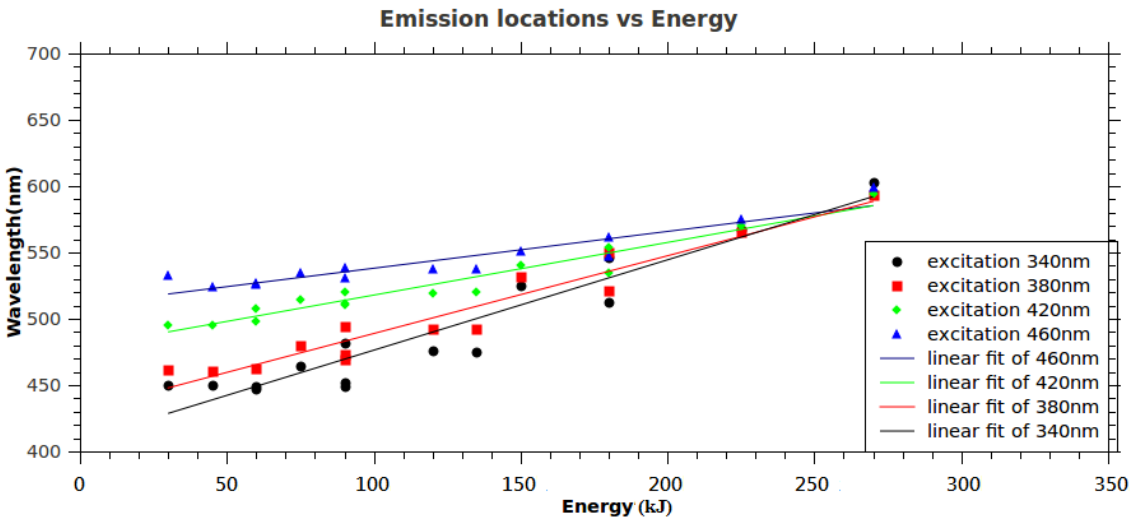

Figure 5-7. All emission centers and their fitting lines. These lines could cross with each other.

Table 5-5. Crossing point of emission centers with others at different excitation wavelengths.

	380	***420***	***460***
340 nm	(575, 245.33)	(578, 249.89)	(582, 255.33)
380 nm		(579, 252.05)	(583, 258.23)
420 nm			(585,268.00)

5.1.3.5 Effect of power deliver rate on emission centers of CNPs

The microwave power, or the "energy delivery rate of the microwave," also affects the emission shift. The higher power results in more energy is applied into the system during synthesis process per unit time. Figure 5-8 shows the power effect on the fitted emission peaks. In the figure, the y-axis is the emission wavelength, the x-axis is the total output energy, and the emission centers with the same power are connected by differently colored lines. In Figure 5-8, the lower power rates have flatter slopes in emission peak shift under excitation at 340 nm and 380 nm. With increasing power, the slope increases. However, for 420 nm and 460 nm exciting emission spectra, all powes show a similar slope. Thus for excitation of 420 nm and 460 nm, the power will not affect slope. Higher energy rates strongly affect emissions exciting at 340 nm and 380 nm, possibly because higher energy rates supply more energy to oxidize the sample. CNP samples excited at 340 nm and 380 nm do not reach to chemical equilibrium state,

and greater energy could cause greater reaction. CNP samples excited at 420 nm and 460 nm are more stable; the extra energy causes reactions at less than 340 nm and 380 nm.

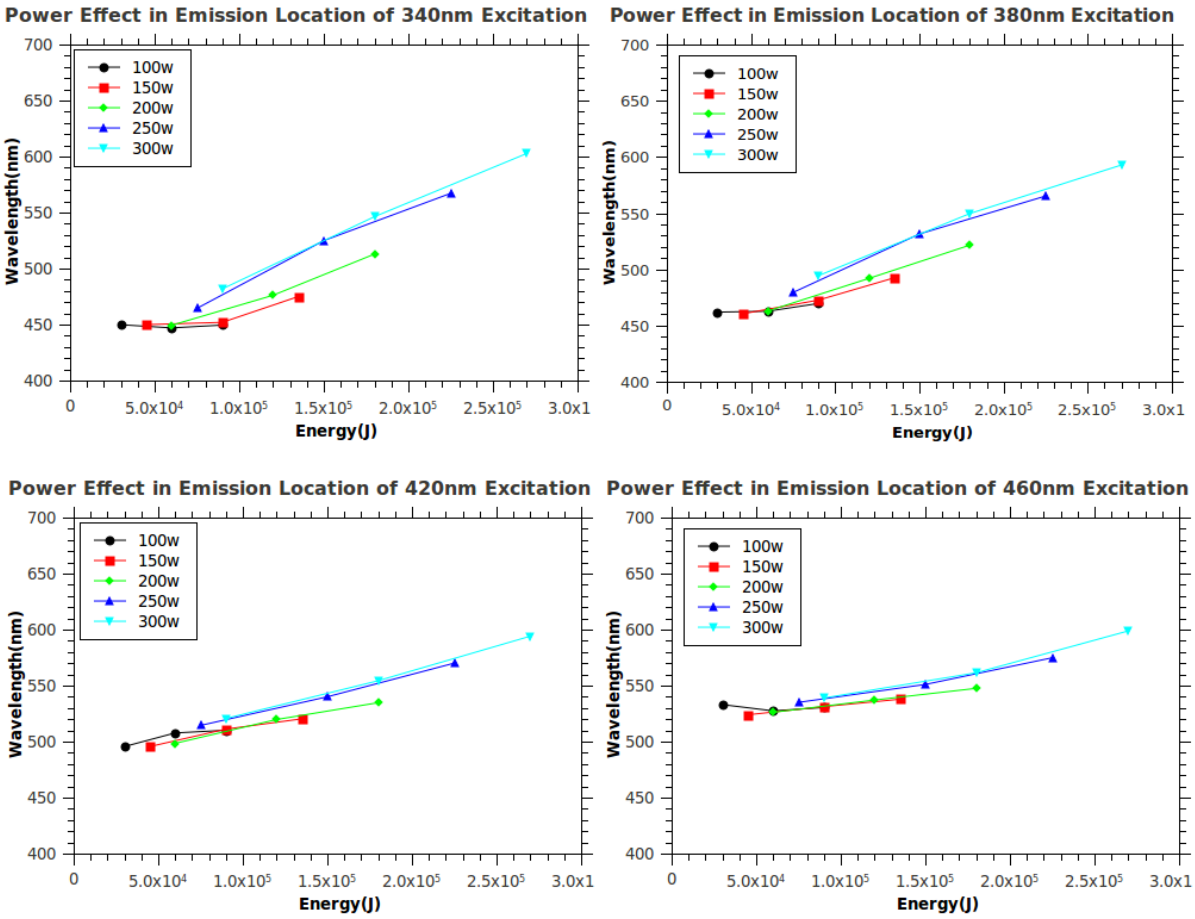

Figure 5-8. Power effect of emission centers in different excitation wavelengths. For 340 and 380 nm excitations, the lower power had flatter slope. Increasing the power meant the slope of shift emission also increased. For 420 to 460 nm excitations, the power did not affect the slope of the shift of emission centers.

5.1.3.6 Another explanation for emission shifting of CNPs by temperature

Although Section 5.1.3.5 illustrated how the power delivery rate could cause emission spectra shifting, there is another reason why emission spectral shifting is affected by temperature. The temperature effect was observed with samples in two groups. One group ran the reaction in aqueous solution in a moderate temperature range (89-100℃). The other group ran it in hydrothermal conditions, i.e. the solution temperatures were over 100℃, but below the critical point (374℃and 221 bar) during the synthesis process. At high temperature and pressure, the chemical and physical properties of water changed. For example, temperature increased, the dielectric constant of water dropped, the ionic product increased, and PKw, the negative log of the water ion product, decreased [25]. Water became both a stronger acid and a stronger base with increased temperature [25]. When temperature rose to 103℃, the process followed the hydrothermal condition. The emissions started to increase with total output energy. In other words, temperature could also be a factor affecting the emission shifting. It was hard to distinguish the effect of power delivery rate and temperature. It is also possible that both factors affect emission shifting.

5.1.3.7 Intensity of PL and heating process

Since the intensity of emission from CNPs was quantified by Gumbel distribution fitting, the effects of heating parameters on emission intensities were also studied. The results showed the intensities were not dependent on the output energy or temperature, but dependent on the heating power and heating time supplied by the microwave system; thus, the intensities were not affected by the combination of power and time, but were

affected by them individually. If we only change either the power or time during synthesis, the intensities of emission will change regularly. However, if we change both power and time together, the intensity of emissions changes without specific order. In order to show the relationship, 3D diagrams were used to plot heating power (x-axis), heating time (y-axis), and intensity (z-axis). In the z-direction, red regions showed high intensity and blue regions showed low intensity. Figure 5-9 shows the 3D diagrams and Figure 5-10 shows the 2D projections of emission intensities for each excitation wavelength. The high intensity region crossed at 100w15m, 100w10m, 200w5m. For the 380 nm exciting emissions, the higher intensity region crossed at 200w5m, 100w15m, 150w5m. When excitation was increased to 420 nm, the high intensity red region shifted to the 150w15m, 200w10m, and 250w5m regions. When excitation was increased to 460 nm again, the high intensity band extended to the 150w15m, 200w10m, and 300w5m regions. In these 3D diagrams and 2D projections, we could see the intensity propagate as a wave with increasing excitation from bottom-left to top-right, which denotes a shift from lower power and less heating time to higher power and longer heating time.

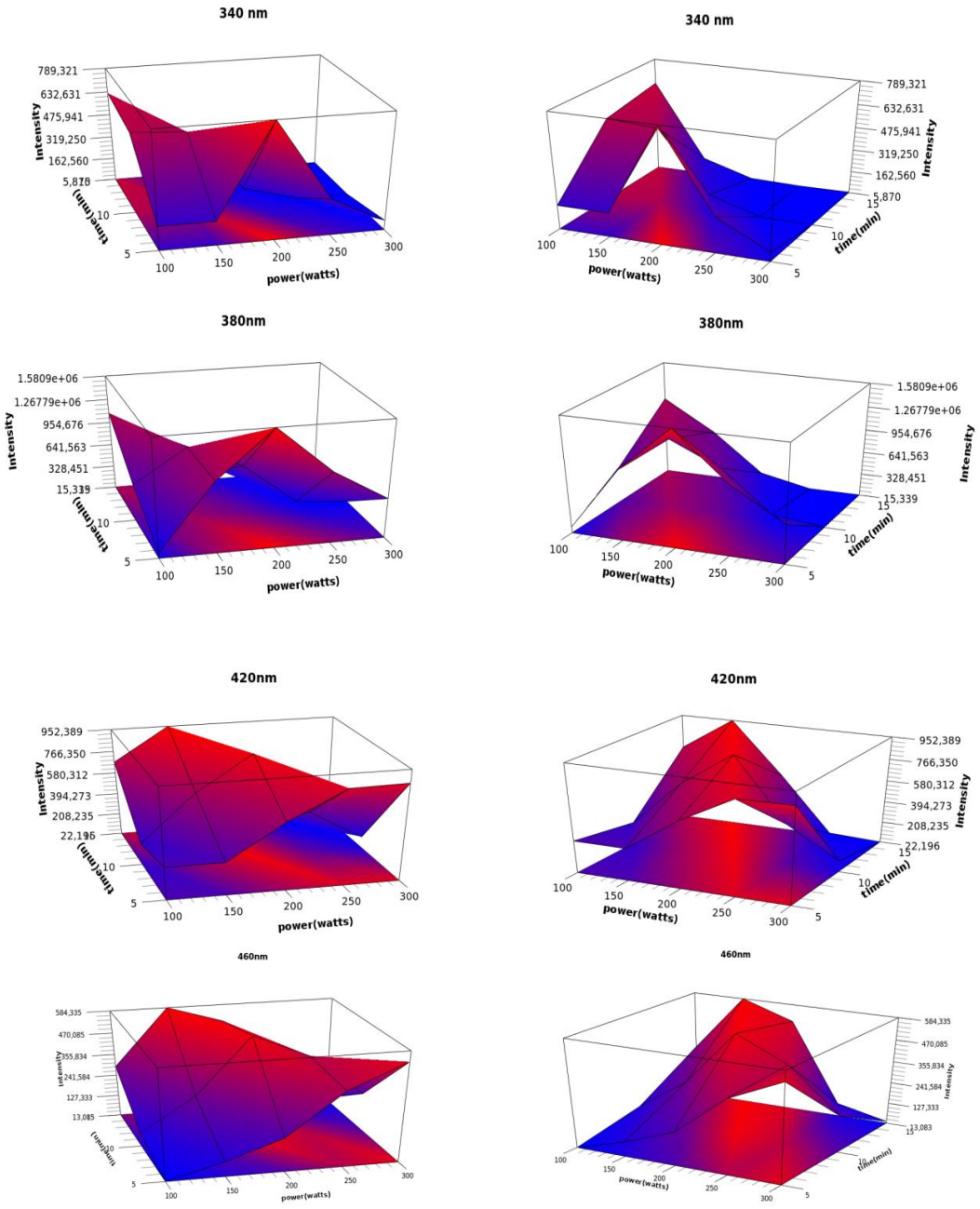

Figure 5-9. 3D diagrams of intensity of emission peaks. The red color shows the high intensity region, which were a red region cross the different heating power and time.

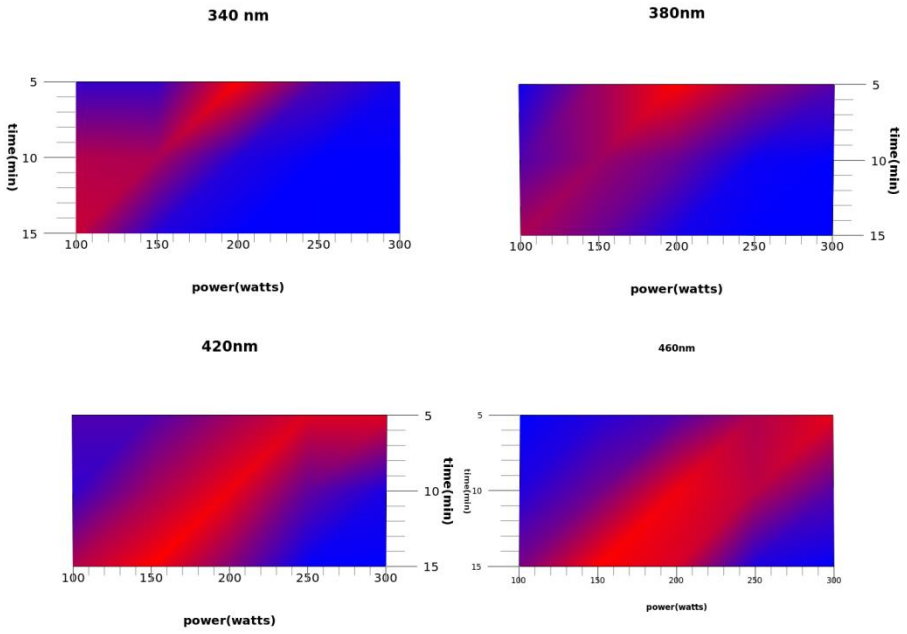

Figure 5-10. 2D projection of 3D diagram of Figure 5-9. 2D projection showed high-intensity slash regions propagated from bottom-left to top-right when the excitation wavelength was increased.

5.1.4 Excitation scanning and fitting results

The excitation spectra were also studied. Emission wavelengths were chosen to be the wavelengths that had the maximum emission for that sample. All samples tested from 200 nm to the wavelength 10 nm less than its emission wavelength. Moreover, the emission spectra were fitted by either Gaussian or Lorentzian distribution with Qtiplot.

For example, the experimental excitation spectrum of the 150w5m sample is presented in Figure 5-11. The emission maximum of the sample was 449 nm, so 450 nm was used as the emission source to detect the excitation spectrum. The result showed that

the sample absorbs wavelengths between 300 to 440 nm to convert emission. The excitation peaked around 371 nm.

Gaussian or Lorentzian distributions were used for spectral fitting. The equations are presented in Section 3.3.2. These equations define the peak location, intensity and FWHM. The results are shown in Table 5-6 with graphs of the curves. For the 250w15m sample, the Lorentzian distribution replaced the Gaussian distribution to fit the excitation curve. For the 300w15m sample, since the intensity was low, the experimental spectra could not be well fitted by either Gaussian or Lorentzian distributions.

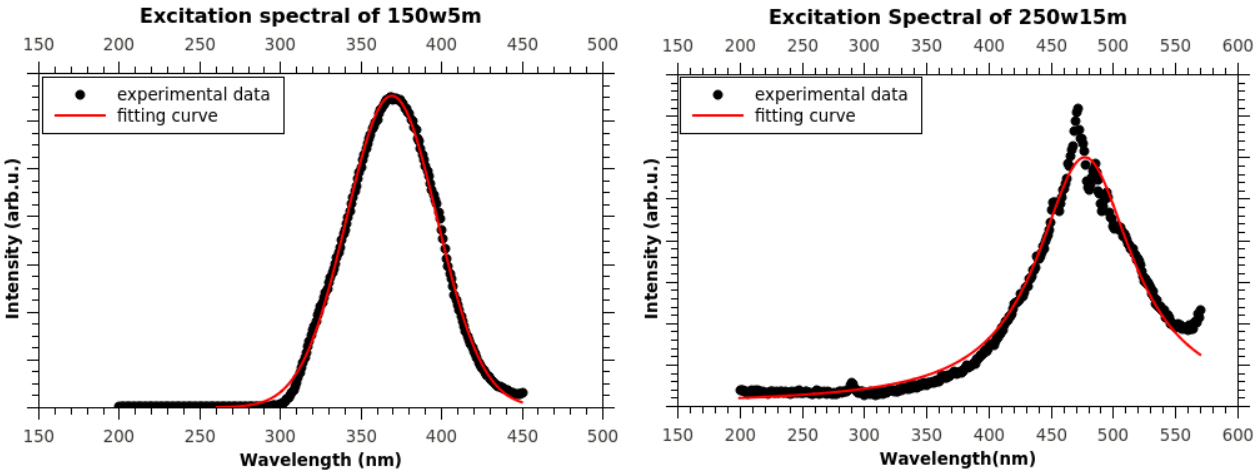

Figure 5-11. Experimental data and Gaussian fitting curve. Left, experimental data (block dots) and Gaussian fitting curve (red line) of the 150w5m sample. All of the excitation spectra of CNPs were fitted by Gaussian distribution except the 250w15m and 300w15m samples. Right, experimental data (block dots) and Lorentz fitting curve (red line) of the 250w15m sample.

Table 5-6. Excitation scanning spectra and their fitting results.

Sample	Emission source (nm)	Fitting parameters			
		Xc (nm)	w (nm)	R^2	A (arb.u.)
100w5m	450	358	66.54	0.995	14069761
100w10m	460	365	56.91	0.996	76452187
100w15m	460	373	53.44	0.998	118865650
150w5m	480	369	56.25	0.998	91994752
150w10m	510	374	54.42	0.998	114610093
150w15m	450	403	68.78	0.993	104138458
200w5m	460	375	53.01	0.999	133213476
200w10m	500	402	68.84	0.992	109823683
200w15m	550	427	80.91	0.989	55096148
250w5m	560	388	58.35	0.995	130248471
250w10m	460	440	79.11	0.992	40905317
250w15m	500	477	93.45	0.979	8760719
300w5m	540	411	70.36	0.990	110925918
300w10m	580	456	77.92	0.988	16834581
300w15m	600	--	--	--	--

5.1.5 Discussion of excitation center shifting

The fitting results showed the excitation peaks ranged from 300 to 550 nm, and the centers ranged from 358 to 456 nm. They showed that the CNPs could absorb UV, near-

UV, and visible light. Figure 5-12. shows excitation fitting centers with a linear fitting line. The slope of the fitting line was 0.0006 with a y-intercept of 335.86 nm. The slope of excitation was close to the slope of the emission excited at 380 nm.

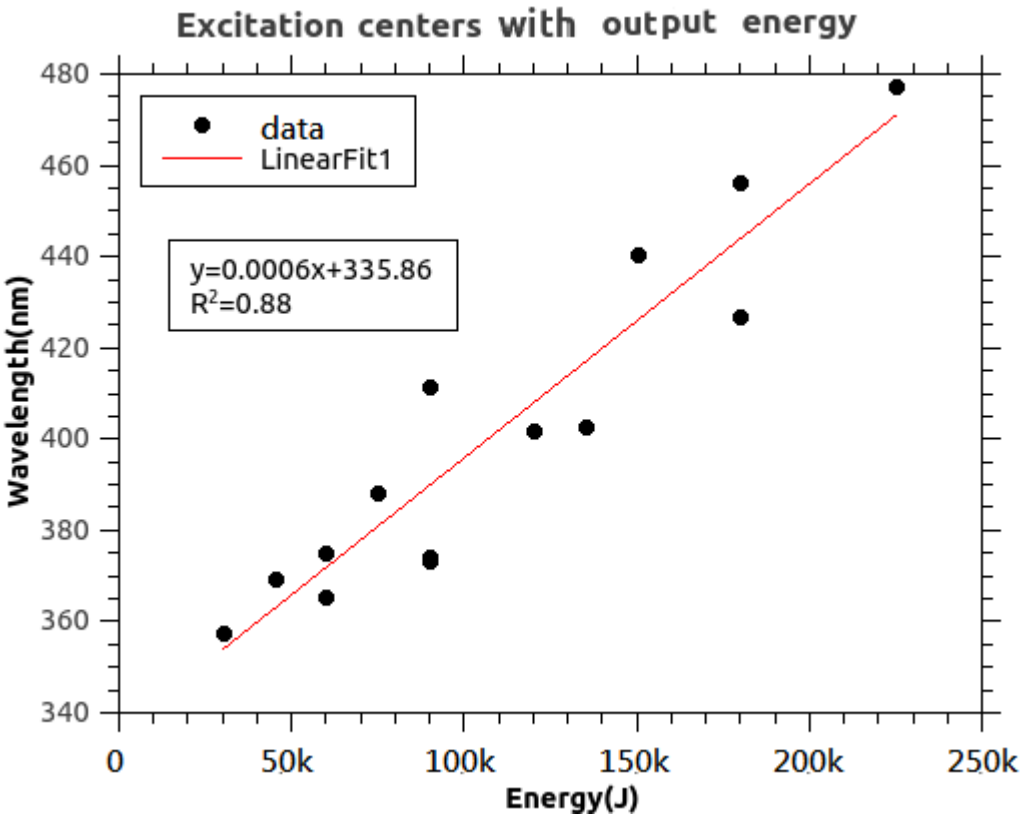

Figure 5-12. Excitation centers plotted with total output energy. Black dots are experimental data and the red line the linear fitting function with a slope of 0.0006 and intercept y-axis at 335.86.

Moreover, the power delivery rate of microwaves had more effect on excitation shifting than emission spectra. Figure 5-13 shows the power delivery rate of the microwaves plotted against excitation wavelength with the five colored lines indicating

the different microwave power used during synthesis. For the sample with lower power, the slope was flat and intersected with the y-axis in the UV region. For the sample with higher power, the slope of excitation increased and intersected with the y-axis in the near-UV region. Figure 5-13 shows that increasing the power resulted in more shifting of excitation centers.

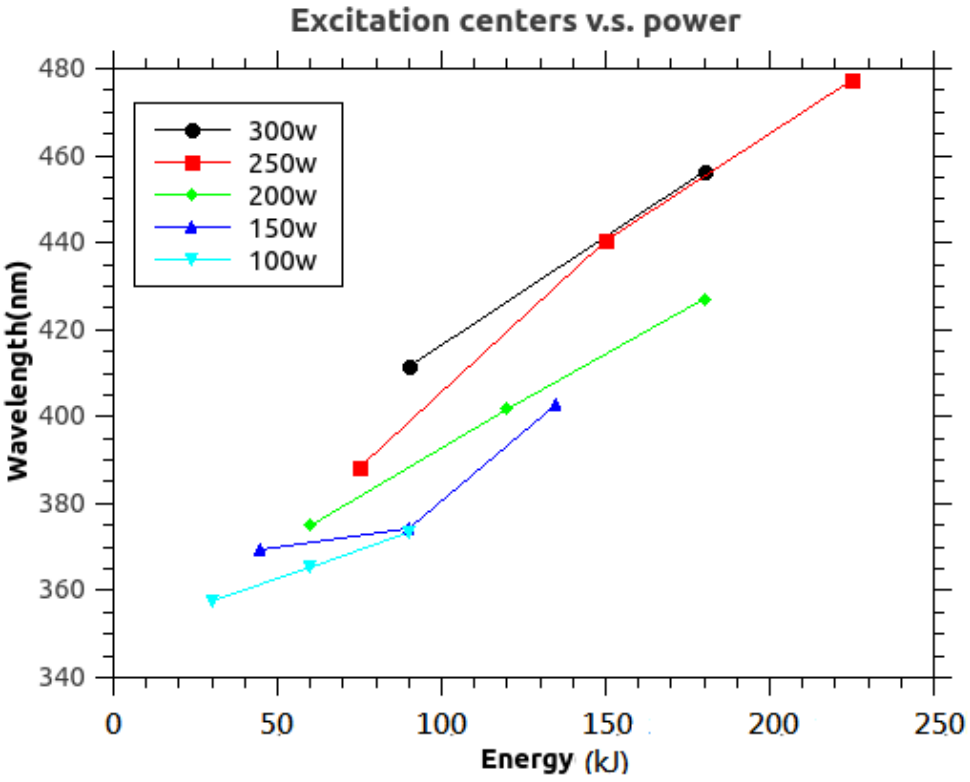

Figure 5-13. Excitation centers plotted with total output energy and power delivery rate. The dots with the same power delivery rate are connected by differently colored lines. The result shows excitation shift depends on power delivery rates.

5.1.6 Summary of emission and excitation

In Section 5.1 the emission shifting properties of the CNPs were presented. The emission spectra of CNPs were recorded under excitation at 340, 380, 420 and 460 nm. Emission spectra of CNPs were fitted with Gumbel distribution to define parameters such as emission maximum and width. The emission peaks shifted with excitation wavelength and output energy of microwaves and either power (energy delivery rate) or temperature during synthesis. The shifting interval of emission centers showed two different groups: one with higher distance of shifting interval and lower output energy, one with lower distance of shifting interval and higher output energy. When increasing output energy was supplied to samples, the shifting intervals of emission peaks were reduced.

Excitation spectrum and shifting properties were also studied. Gaussian and Lorentzian distributions were used to fit and quantify the excitation spectra. The excitation spectra also depended on total output energy. Moreover, the excitation shift depended on the power delivery rate.

5.2 Absorbance

5.2.1 Absorbance spectra

Absorbance spectra of the CNPs were measured from 200 nm to 700 nm. The resulted showed the CNPs had high absorption across the UV region to the visible region. As produced, the peak absorbance of CNPs was too strong to measure. So, measurements were also made with concentrations of CNPs solutions diluted to 1% with

water. The results showed there was a 3-4% error between 100% and 1% of CNP solutions.

Figure 5-14 shows the absorbance spectra of CNPs with different heating time and power. The absorbance spectrum of the glucose solution without microwave heating is also presented as a reference to show that there is no absorbance in the 210 nm to 700 nm range. For the CNPs, the spectra have two general characteristics. First, the absorbance spectra exhibit two peaks located at 283 nm and 225 nm that did not shift with experimental parameters. However, the intensity increased with heating time and power. Second, long tails extended from the base of the 283 nm peak toward the visible region. The tail became longer with increasing total output energy. However, the excitation scanning spectra showed that the 283 nm and 225 nm peaks did not cause fluorescence and only part of the long tails did so.

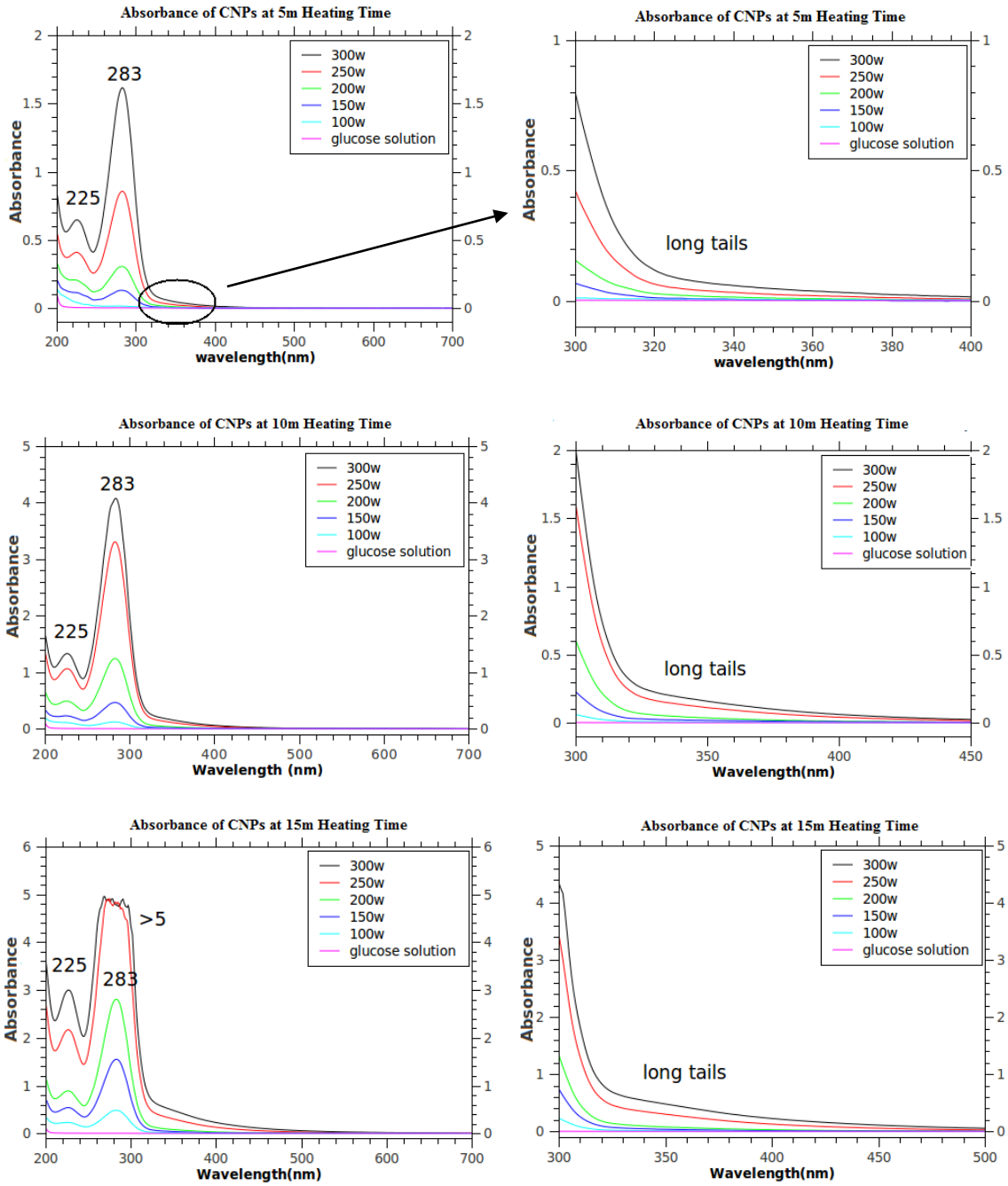

Figure 5-14. Absorbance of 1%CNPs with different heating time and power. Top: five-minute heating time. Middle: 10-minute heating time. Bottom: 15-minute heating time. Two specific peaks are located at 283 nm and 225 nm. The intensity increased with heating time and power. Long tails extend from them UV region to the visible region, and according to excitation scanning, only part of the long tails results in luminance.

5.2.2 A 283 nm peak in absorbance provides carbon derivatives

Schroder's research group studied the major products of microwave synthesis in hydrothermal conditions to degrade glucose and fructose[35]. In their report, two of the major products were 5-(hydroxymethyl)furfural (5-HMF) and 3-Deoxyglucosone (3-DG). In other literature, the absorption and Raman spectra of 5-HMF were studied. The absorbance spectrum of 5-HMF showed a peak between 277 and 284 nm [33, 36]. and 3-DG exhibited a peak in 223 nm [36]. In their report, the Raman spectra of 5-HMF and 3-DG were also reported. There are several peaks in the spectrum [33, 37]. However, in our Raman spectra of CNPs, peaks are encased together so that we could not identify the specific peak of 5-HMF. The absorbance peaks at 283 and 225 nm show the decomposition of glucose and show glucose derivatives are presented during microwave synthesis.

5.2.3 Discussion of absorbance intensities and emission intensities

According to literature reports, the absorbance intensity at 283 nm reflects mainly 5-HMF concentration. Therefore, we can assume that 5-HMF accounts for the intensity of the 283 nm peak. The samples with excitation at 340 nm and excitation at 380 nm exhibited high intensity when absorbance was between 0.2 and 0.4. This result implies the blue-fluorescent CNPs were manufactured in the early stage of glucose decomposition. It showed the green-luminance CNPs were generated in the middle stage of glucose decomposition. An interesting small decrease of 1.6 in absorbance intensity of all samples meant all emission intensity decreased after this point. It implies CNPs start to degrade after this point.

5.2.4 Hypothesis on the product of CNPs

The 5-HMF and 3-Deoxyglucosone had no luminance under UV exposure. Moreover, the excitation scans showed that excitation at 283 nm and 225 nm did not produce fluorescence. The absorption causing fluorescence must be located in the tails extending toward the visible region. Schroder's group reported the following results of keeping 5-HMF decomposed. The product in the microwave synthesis process was 1,2,4 trihydroxy benzene. The literature study found 5-HMF derivatives [38] and benzenetriol had an excitation range from 300 nm to 400 nm and emission range from 400 to 500 nm. The emission properties changed depending on the 5-HMF derivatives. The 1,2,4 trihydroxy benzene had several absorbance peaks at 300 nm to 400 nm and Raman spectral peaks in the 1400 cm^{-1} to 1600 cm^{-1} region [39]. However, in CNP solutions, these peaks are encased in a broad band or long tails. So these data could not provide definitive evidence that 1,2,4 trihydroxy benzene was present in CNP solutions. In summary, the most reasonable explanation of the fluorescence mechanism of CNPs is some derivative of 5-HMF and 1,2,4-benzenetriol.

5.2.5 Summary of absorbance

The absorbance of 1% CNPs diluted with water was reported. The absorbance of CNPs showed strong peaks at 225 nm and 283 nm. According to reference, these two peaks are owed to the 5-HMF and 3-DG. The intensity of these peaks increased with heating power and time, as with emission spectra. The blue emission of CNPs had high intensity when 1% CNPs had 0.12 to 0.46 absorption. The green emission of CNPs had high intensity when 1% CNP had 0.857 to 1.615 absorption.

CHAPTER VI

HYPOTHESIS OF FLUORESCENT MECHANISM, SUMMARY AND FUTURE WORKS

6.1 Summary

In the microwave-assisted synthesis, the experiment started with 33% by weight of glucose solution. The solutions were microwaved by a CEM laboratory. The controlled variables were heating power and heating time. We calculated the combination of power and time for the total output energy of the microwave source. The color of the CNPs solutions changed with synthesis parameters. Fluorescence could be detected after synthesis. Physical properties and optical performance were studied. When the total microwave output energy increased, the results showed:

Physical properties

- Particle size increased from 3 nm to 100 nm (by TEM)
- Particle size distribution became wide (by TEM)
- Particle structure from amorphous to polycrystalline (by diffraction patterns)
- δ (C-C-C), δ (C-C-O) bond increase (by Raman)
- D band and G band peaks in Raman spectrum decreased

Optical performance

- Emission red shift with excitation wavelength
- Emission red shift with microwave output energy
- Emission position slope became flatter and emission interval narrowed down

- Excitation red shift with microwave output energy
- Absorption intensity at 283 nm and 225 nm increased
- Absorption tails into the visible extended
- Intensity of absorption in 283 nm was in proportion to emission intensity

6.2 Discussion of Raman spectrum, absorbance and emission of CNPs.

6.2.1 Raman spectrum implied CNP product

Raman spectra showed two characterful peaks in 1363 cm^{-1} and 1820 cm^{-1}, which we attribute to a disordered aromatic compound with defects and carbonyl compounds. For the 300w15m sample, the aromatic and carbonyl signals reduce but there is still a relatively strong signal in skeletal carbon bonding, implying the major products in the sample are carbon hydrate chains. The 425 and 538cm^{-1} peaks implied CNPs have carbon linear chains.

Schroder's research group studied the major products of glucose decomposition in microwave synthesis [35]. In their report, two of the major products were 5-HMF and 3-DG. In other literature reported, the Raman spectra of 5-HMF and 3-DG have several peaks [33, 37]. However, in our Raman spectra of CNPs, peaks were encased together so that we could not identify the specific peak of 5-HMF.

6.2.2 Discussion of absorbance intensities and emission intensities

According to literature reports, the absorbance intensity at 283 nm mainly reflects 5-HMF concentration. Therefore, we can assume that 5-HMF accounts for the intensity of the 283 nm peak. Figure 6-1 shows the relationship between emission intensity and absorbance intensity at 283 nm, implying changes in the concentration of 5-HMF. In

Figure 6-1, excitation 340 nm and excitation 380 nm groups exhibited high emission intensity when absorbance was between 0.2 and 0.4. This result implied the blue-luminance CNPs were manufactured in the early stage of glucose decomposition. The 420 nm and 460 nm excitations exhibited high emission intensities had an absorbance between 1 to 3. It showed the green- and yellow-luminance CNPs were generated in the middle stage of glucose decomposition. An interesting small decrease of 1.6 in absorbance intensity of all samples meant all emission intensity decreased after this point. It implied CNPs start to degrade after this point.

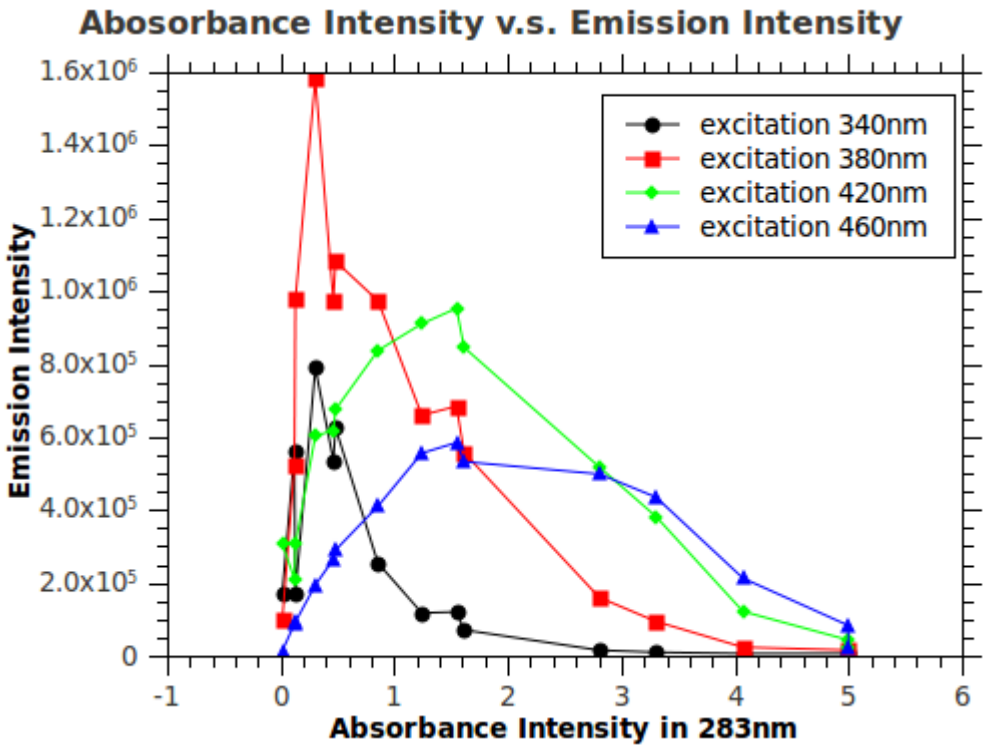

Figure 6-1. Absorbance intensity at 283 nm of CNPs (1%)plotted with emission intensity.

6.3 Hypothesis on the product of CNPs

The absorption shows 5-HMF and 3-DG in CNP solution. However, the 5-HMF and 3-DG had no luminance under UV exposure. Moreover, the excitation scans showed that excitation at 283 nm and 225 nm did not produce fluorescence. The absorption causing fluorescence must be located in the tails extending toward the visible region.

In Schroder's report, glucose decomposition under microwave heating took place [35]. Although their experiment under a different microwave synthesis conditions (1400 watts in power and 180 to 250℃ in temperature), our absorbance spectrum showed two peaks at 225 and 283, which shows 5-HMF were synthesized during microwave synthesis. The glucose in low-pH environment decomposed to 5-HMF [36]. If the oxidation reaction were continuous, 5-HMF would change to three different routes. First, 5-HMF would become 1,2,4-benzenetriol. Second, 5-HMF would decompose to levulinic acid and formic acid. Third, some literature reports the products would apply intermolecular dehydration and aldol condensation reaction to form cellular particles or dye [40, 41]. The whole reaction process is shown in Figure 6-2.

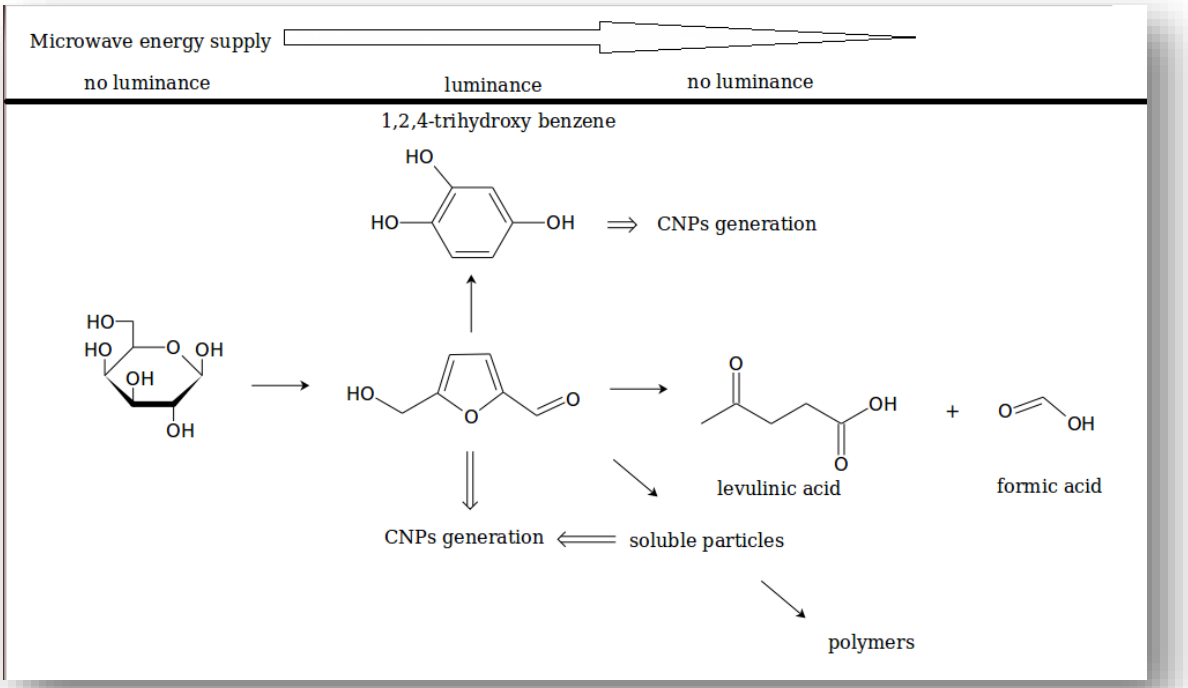

Figure 6-2. Hypothesis of the reaction process of CNP generation. Glucose was oxidized and decomposed to 5-HMF under microwave heating. 5-HMF generated CNPs in the following steps. Finally, the heating energy was overloaded so the CNPs transferred to alliphic products.

In the first and third routes, 5-HMF was oxidized to 1,2,4 trihydroxy benzene and 5-HMF derivatives. In the literature study, we found 5-HMF derivatives and benzenetriol had an excitation range from 300 nm to 400 nm and fluorescent emission range from 400 nm to 500 nm [36], which matched the excitation and emission region with CNPs. Moreover, the emission could change depending on different 5-HMF derivatives. Therefore, the most plausible explanation is that CNPs are a derivative of 5-HMF and 1,2,4-benzenetriol.

In the second route, 5-HMF was oxidized to levulinc acid and formic acid. 5-HMF showed an aromatic ring in its molecular structure. The levulinc acid and formic acid were carbon hydrate chains. The results match the Raman spectrum tendency. When the glucose solution was prepared, there was no luminance in the solutions. After the heating process started, the glucose was oxidized and started to decompose to 5-HMF. The increased temperature made water act like acid to catalyze the glucose transfer to 5-HMF. The aromatic structure and sp2 carbon bonding of 5-HMF made the Raman spectrum show a high intensity at peaks of 1363 and 1820 cm^{-1}. During microwave output energy increase, 5-HMF went through a chemical reaction such as condensation and derivatives were synthesized. When the energy supplied was more than the reaction needs CNPs and 5-HMF started to degrade with output energy. The aromatic rings were opened and more alliphic products such as levulinc acid and formic acid were produced. In the Raman spectrum, peaks at 1363 and 1820 cm^{-1} decrease because CNPs and 5-HMF transfer to carbon hydrate chains.

6.4 Experimental limitation and future works

Our experimental work has some limitations, which we hope can be modified in the future. First, there is no direct evidence of the fluorescent mechanism. Although we propose a logical hypothesis to explain the phenomenon, we cannot deny that fluorescence could be caused by other factors. In order to understand the fluorescent mechanism of CNPs, further study is necessary.

Second, the resolution of the TEM sample is low. Although the negative staining preparation method is applied, the images of the CNPs are still not clear when the

particles are small. In future works, a better imaging method or sample preparation method should be created to give more information about CNP structure.

Third, the absorbance and Raman spectrum were encased together so it was hard to distinguish the single peak in the spectrum. The multiple products in the solutions are probably a direct result of this. Future work should design a purification method to filter other non-fluorescent products. The purification of CNPs could clarify absorbance and Raman spectra for studying their properties and fluorescent mechanism.

6.5 Contributions

In this dissertation, three aims were accomplished. We are responsible for four innovations that contribute to CNP research.

First, we designed a new microwave-assisted synthesis method and the experimental parameters were studied: critical parameters of power, time, and total output microwave energy were found to control emission and excitation properties. According to our results, engineers could design CNP products at specific excitations and emission wavelengths. As far as we know, we are the first group to develop the emission control technique in the CNP manufacture process.

Second, we are the first group to design a microwave-assisted synthesis method to make fluorescent carbon particles of huge size. The particles have the ability to change shape during the synthesis process. This process means CNPs have high potential not only for bio-imagery and bio-labeling, but also application in the monitoring industries since they offer stable and low-cost products.

Third, CNP properties were analyzed in terms of their physical and optical properties by experimental and statistical methods. This result provides a clue for the study of the electronic configuration of excited state.

Finally, we posited a hypothesis about the products of CNPs' formation process and an assumption exploring the fluorescent mechanism supported by our experimental data and reference literature. Although we do not have definitive evidence to prove the fluorescent mechanism, this hypothesis provides a logical explanation that should be explored in the future.

REFERENCES

1. Ntziachristos, V., *Fluorescence Molecular Imaging.* Annual Review of Biomedical Engineering, 2006. **8**(1): p. 1-33.

2. Lakowicz, J., *Principles of Fluorescence Spectroscopy*. Principles of Fluorescence Spectroscopy. 1999, New York,: Kluwer Academic/Plenum Publishers.

3. Bera, D., et al., *Quantum Dots and Their Multimodal Applications: A Review.* Materials, 2010. **3**(4): p. 2260-2345.

4. Lin, C.-A.J., et al., *Bioanalytics and biolabeling with semiconductor nanoparticles (quantum dots).* Journal of Materials Chemistry, 2007. **17**(14): p. 1343-1346.

5. Esteves da Silva, J.C.G. and H.M.R. Gonçalves, *Analytical and bioanalytical applications of carbon dots.* TrAC Trends in Analytical Chemistry, 2011. **30**(8): p. 1327-1336.

6. Xu, X., et al., *Electrophoretic Analysis and Purification of Fluorescent Single-Walled Carbon Nanotube Fragments.* Journal of the American Chemical Society, 2004. **126**(40): p. 12736-12737.

7. Cao, L., et al., *Carbon Dots for Multiphoton Bioimaging.* Journal of the American Chemical Society, 2007. **129**(37): p. 11318-11319.

8. Yang, S.-T., et al., *Carbon Dots for Optical Imaging in Vivo.* Journal of the American Chemical Society, 2009. **131**(32): p. 11308-11309.

9. Sahu, S., et al., *Simple one-step synthesis of highly luminescent carbon dots from orange juice: application as excellent bio-imaging agents.* Chemical Communications, 2012. **48**(70): p. 8835-8837.

10. Yang, Z.-C., et al., *Intrinsically fluorescent carbon dots with tunable emission derived from hydrothermal treatment of glucose in the presence of monopotassium phosphate.* Chemical Communications, 2011. **47**(42): p. 11615-11617.

11. Sun, Y.-P., et al., *Quantum-Sized Carbon Dots for Bright and Colorful Photoluminescence.* Journal of the American Chemical Society, 2006. **128**(24): p. 7756-7757.

12. Zhang, B., C.-y. Liu, and Y. Liu, *A Novel One-Step Approach to Synthesize Fluorescent Carbon Nanoparticles.* European Journal of Inorganic Chemistry, 2010. **2010**(28): p. 4411-4414.

13. Peng, H. and J. Travas-Sejdic, *Simple Aqueous Solution Route to Luminescent Carbogenic Dots from Carbohydrates.* Chemistry of Materials, 2009. **21**(23): p. 5563-5565.

14. Wang, X., et al., *Bandgap-Like Strong Fluorescence in Functionalized Carbon Nanoparticles.* Angewandte Chemie International Edition, 2010. **49**(31): p. 5310-5314.

15. Dong, Y., et al., *Extraction of Electrochemiluminescent Oxidized Carbon Quantum Dots from Activated Carbon.* Chemistry of Materials, 2010. **22**(21): p. 5895-5899.

16. Liu, H., T. Ye, and C. Mao, *Fluorescent Carbon Nanoparticles Derived from Candle Soot.* Angewandte Chemie International Edition, 2007. **46**(34): p. 6473-6475.

17. Wang, X., et al., *Microwave assisted one-step green synthesis of cell-permeable multicolor photoluminescent carbon dots without surface passivation reagents.* Journal of Materials Chemistry, 2011. **21**(8): p. 2445-2450.

18. Sun, X., et al., *Nano-graphene oxide for cellular imaging and drug delivery.* Nano Research, 2008. **1**(3): p. 203-212.

19. Tian, L., et al., *Nanosized Carbon Particles From Natural Gas Soot.* Chemistry of Materials, 2009. **21**(13): p. 2803-2809.

20. Qian, Z., et al., *The visible photoluminescence mechanism of oxidized multi-walled carbon nanotubes: an experimental and theoretical investigation.* Journal of Materials Chemistry C, 2013. **1**(2): p. 307-314.

21. Kozawa, D., et al., *Exploring the Origin of Blue and Ultraviolet Fluorescence in Graphene Oxide.* The Journal of Physical Chemistry Letters, 2013. **4**(12): p. 2035-2040.

22. Li, H., et al., *One-step ultrasonic synthesis of water-soluble carbon nanoparticles with excellent photoluminescent properties.* Carbon, 2011. **49**(2): p. 605-609.

23. Lin, Z., et al., *Peroxynitrous-Acid-Induced Chemiluminescence of Fluorescent Carbon Dots for Nitrite Sensing.* Analytical Chemistry, 2011. **83**(21): p. 8245-8251.

24. Zhou, J., et al., *An Electrochemical Avenue to Blue Luminescent Nanocrystals from Multiwalled Carbon Nanotubes (MWCNTs).* Journal of the American Chemical Society, 2007. **129**(4): p. 744-745.

25. Dallinger, D. and C.O. Kappe, *Microwave-Assisted Synthesis in Water as Solvent.* Chemical Reviews, 2007. **107**(6): p. 2563-2591.

26. Stuerga, D., *Microwave–Materials Interactions and Dielectric Properties: From Molecules and Macromolecules to Solids and Colloidal Suspensions*, Microwaves in Organic Synthesis. 2012, Germany, Wiley-VCH Verlag GmbH & Co. KGaA. p. 1-56.

27. P. Debye, *Polar molecules.* Journal of the Society of Chemical Industry, 1929. **48**(43): p. 1036-1037.

28. Ondruschka, B., W. Bonrath, and D. Stuerga, *Development and Design of Reactors in Microwave-Assisted Chemistry*, Microwaves in Organic Synthesis. 2012, Germany, Wiley-VCH Verlag GmbH & Co. KGaA. p. 57-103.

29. Zhu, H., et al., *Microwave synthesis of fluorescent carbon nanoparticles with electrochemiluminescence properties.* Chemical Communications, 2009(34): p. 5118-5120.

30. CEM Corporation.(2006), August 2014; (a): CEM Discover® microwave instrument. http://cem.com/discover-sp-accessories.html, (b): CEM's microwave heating theory http://cem.com/discover-sp-technology.html, (c): specific glass vessel http://cem.com/discover-sp-vessels.html. Available from: http://www.cem.com/.

31. Zhu, S., et al., *Highly Photoluminescent Carbon Dots for Multicolor Patterning, Sensors, and Bioimaging.* Angewandte Chemie International Edition, 2013. **52**(14): p. 3953-3957.

32. Richardson, B., *Electron Microscopy in Microbiology.* Journal of Microscopy, 1999. **195**(2): p. 164-164.

33. Jia, T.-j., et al., *A study of surface enhanced Raman scattering for furfural adsorbed on silver surface.* Journal of Molecular Structure, 2008. **873**(1–3): p. 1-4.

34. Söderholm, S., et al., *Raman spectra of fructose and glucose in the amorphous and crystalline states.* Journal of Raman Spectroscopy, 1999. **30**(11): p. 1009-1018.

35. Möller, M., F. Harnisch, and U. Schröder, *Microwave-assisted hydrothermal degradation of fructose and glucose in subcritical water.* Biomass and Bioenergy, 2012. **39**(0): p. 389-398.

36. KJELLSTRAND, et al., *Degradation in peritoneal dialysis fluids may be avoided by using low pH and high glucose concentration*. Vol. 21. 2001, Milton, ON, Canada: Multimed.

37. Kim, T., et al., *Studies of the Raman spectra of cyclic and acyclic molecules: Combination and prediction spectrum methods.* Chemical Physics Letters, 2012. **531**(0): p. 210-215.

38. Walmsley, T.A. and M. Lever, *Fluorometric measurement of furfural and 5-hydroxymethylfurfural.* Analytical Biochemistry, 1982. **124**(2): p. 446-451.

39. Qin, L., G.N.R. Tripathi, and R.H. Schuler, *Radiolytic oxidation of 1,2,4-benzenetriol. An application of time-resolved resonance Raman spectroscopy to kinetic studies of reaction intermediates.* The Journal of Physical Chemistry, 1987. **91**(7): p. 1905-1910.

40. Sevilla, M. and A.B. Fuertes, *The production of carbon materials by hydrothermal carbonization of cellulose.* Carbon, 2009. **47**(9): p. 2281-2289.

41. Zhen Fang, R.L.S.J., Janusz A. Kozinski,et al., *Reaction Of D-glucose In Water At High Temperatures (410 Oc) And Pressures (180 Mpa) For The Production Of Dyes And Nano-particles[J]*. The Journal Of Supercritical Fluids, 2011. **56(1)**: p. 41-47.

APPENDIX A

Emission spectrum of CNPs

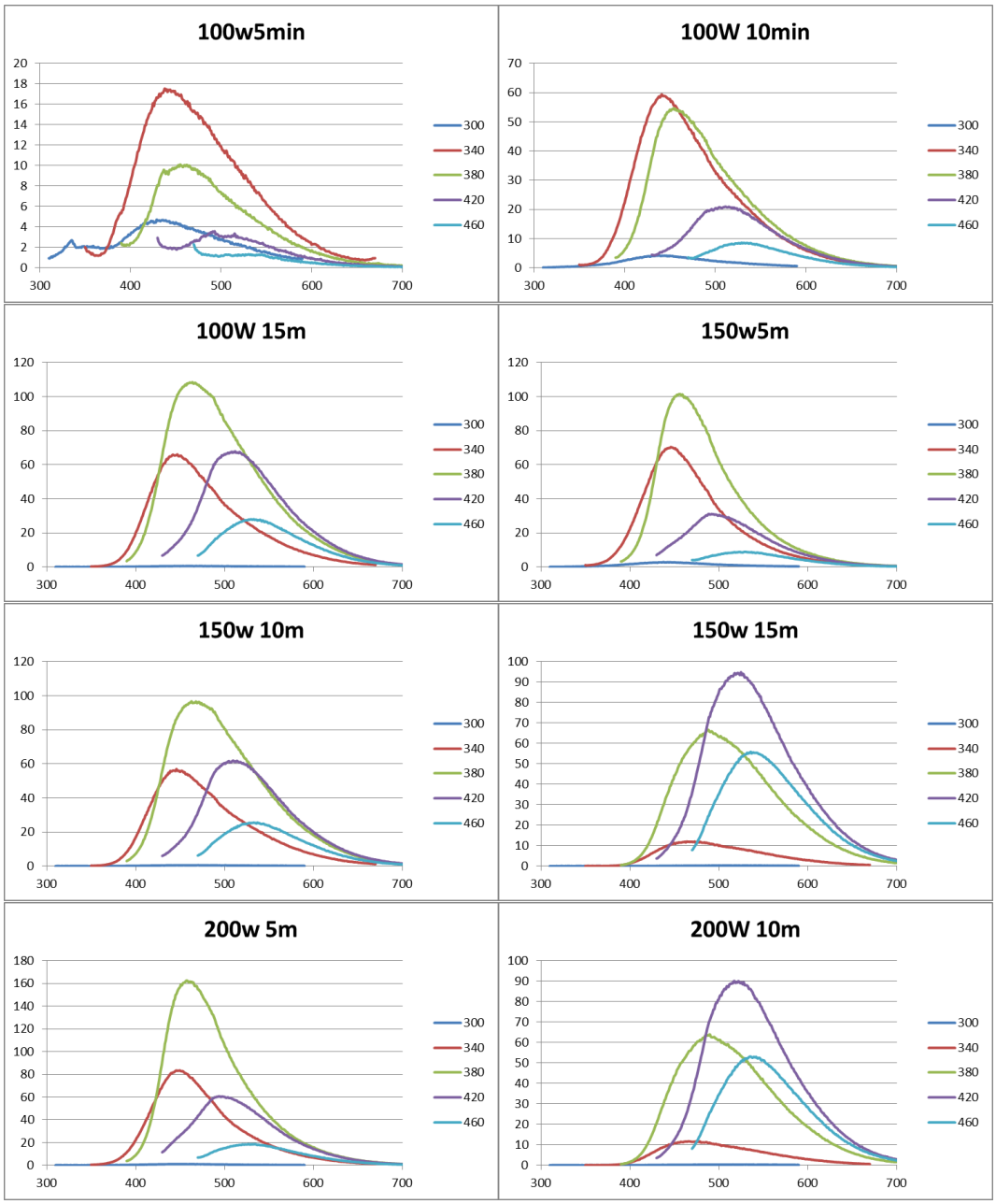

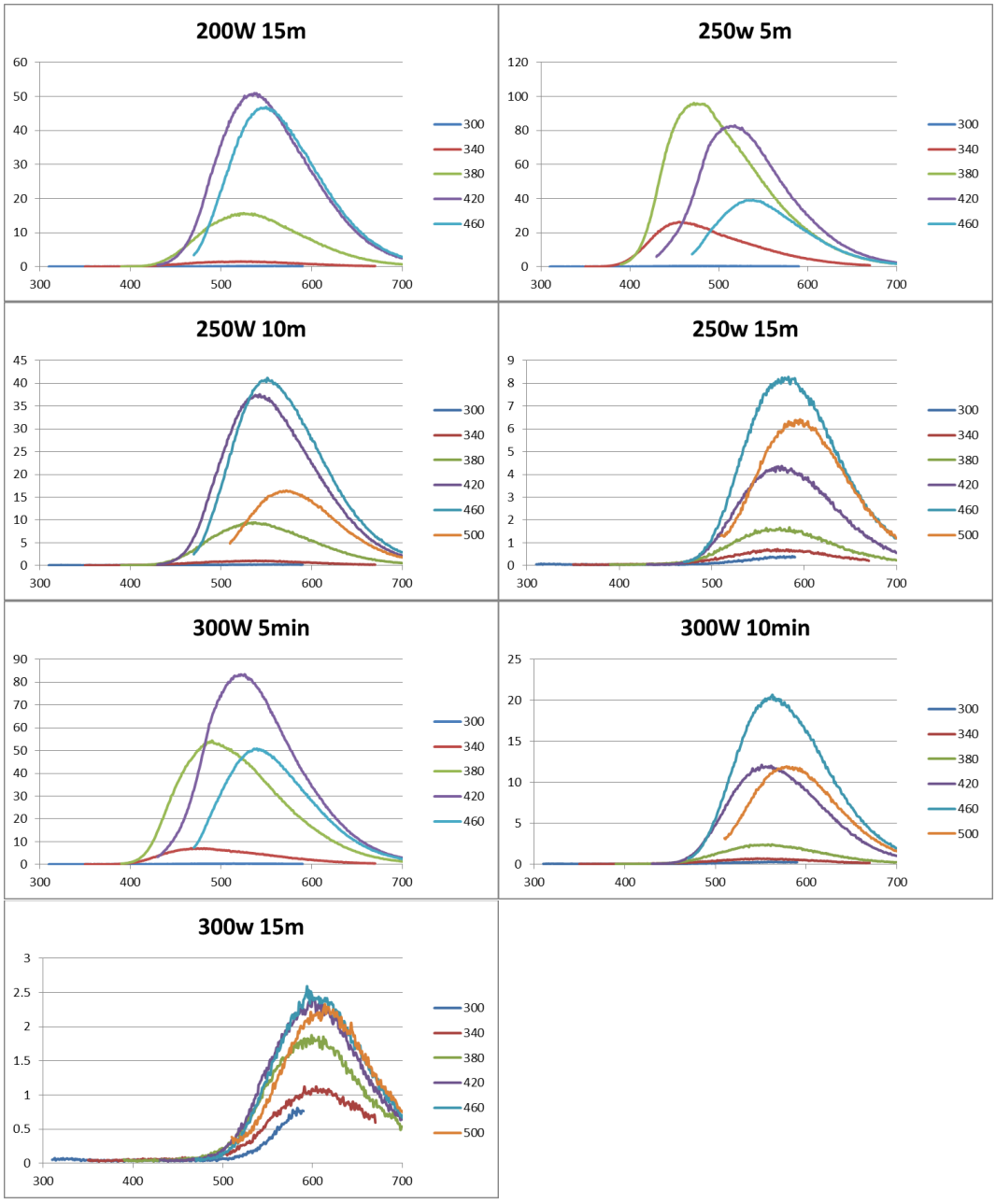
200W 15m
250w 5m
250W 10m
250w 15m
300W 5min
300W 10min
300w 15m
300
340
380
420
460
500

APPENDIX B

Emission spectrum and fitting result

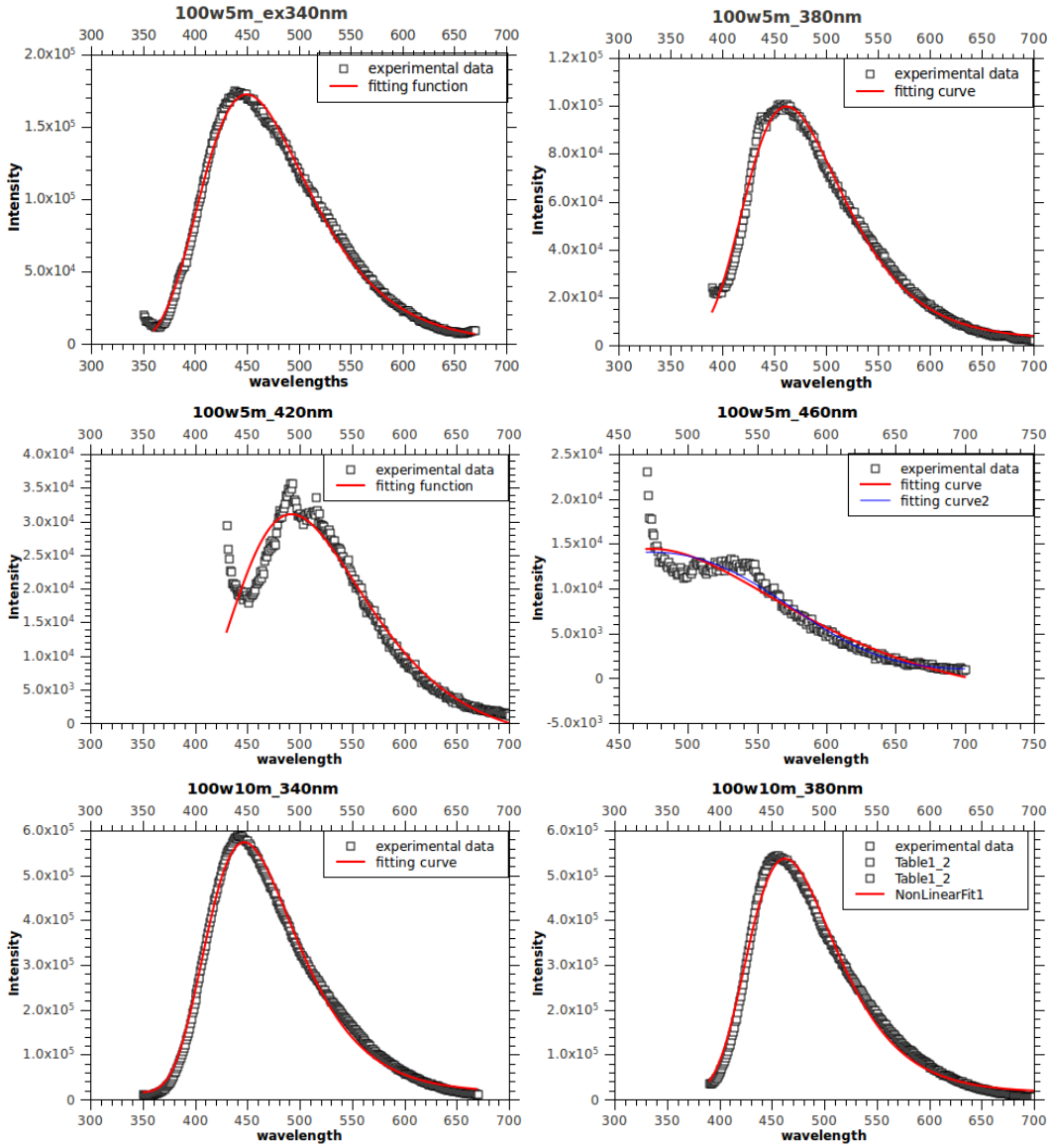

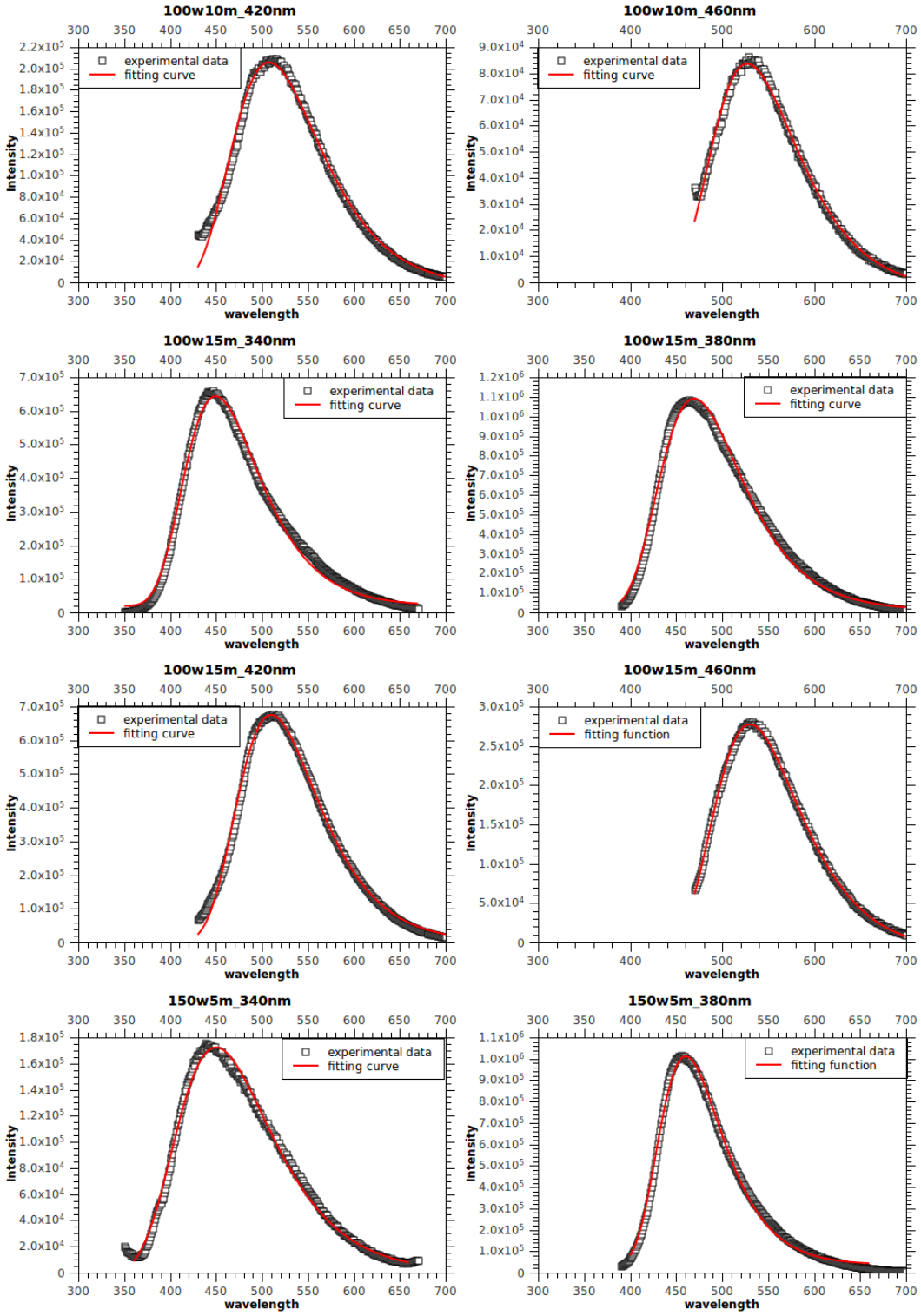
100w10m_420nm
experimental data
fitting curve
Intensity
wavelength
100w10m_460nm
experimental data
fitting curve
Intensity
wavelength
100w15m_340nm
experimental data
fitting curve
Intensity
wavelength
100w15m_380nm
experimental data
fitting curve
Intensity
wavelength
100w15m_420nm
experimental data
fitting curve
Intensity
wavelength
100w15m_460nm
experimental data
fitting function
Intensity
wavelength
150w5m_340nm
experimental data
fitting curve
Intensity
wavelength
150w5m_380nm
experimental data
fitting function
Intensity
wavelength

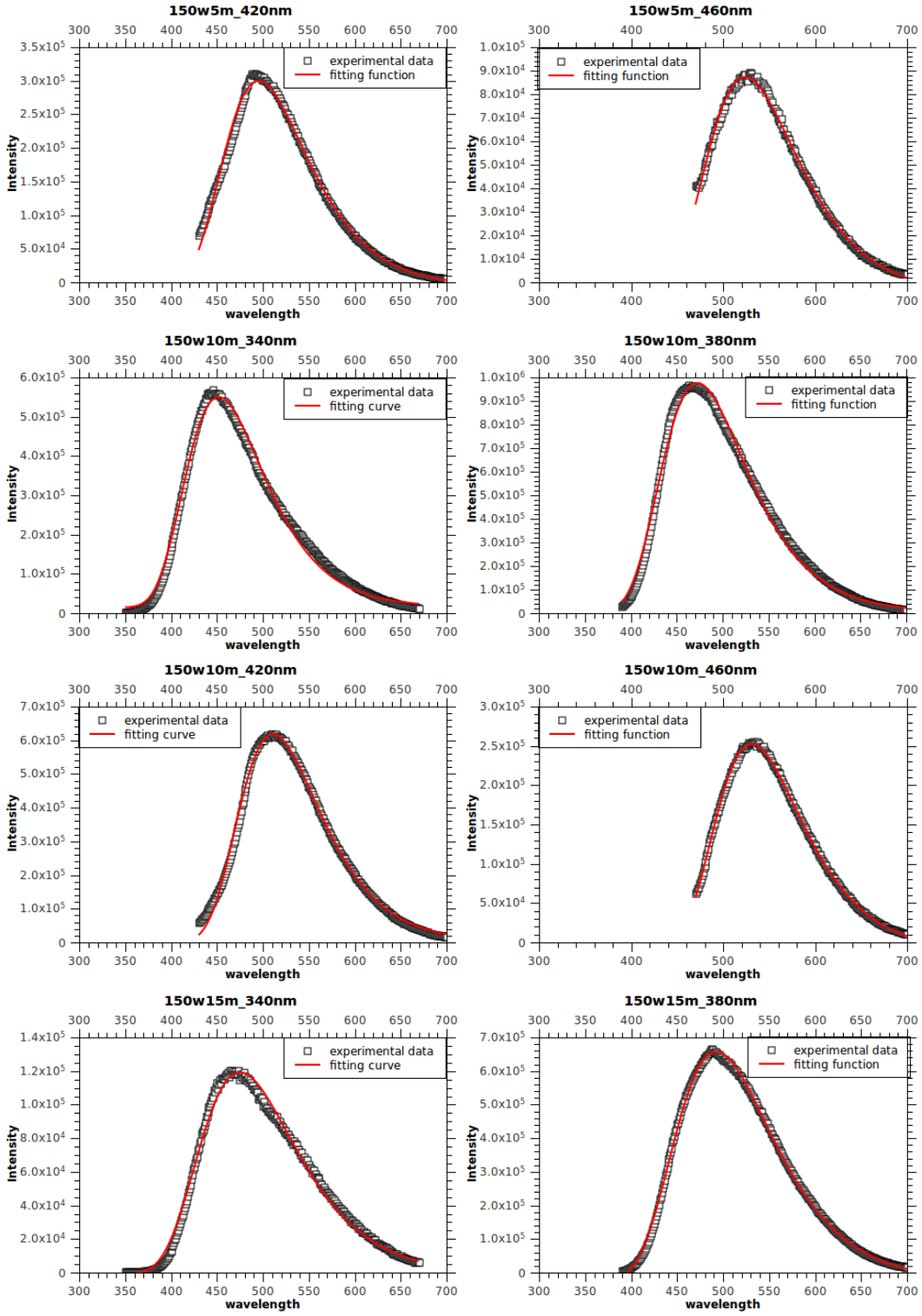
150w5m_420nm
experimental data
fitting function
Intensity
wavelength
150w5m_460nm
experimental data
fitting function
Intensity
wavelength
150w10m_340nm
experimental data
fitting curve
Intensity
wavelength
150w10m_380nm
experimental data
fitting function
Intensity
wavelength
150w10m_420nm
experimental data
fitting curve
Intensity
wavelength
150w10m_460nm
experimental data
fitting function
Intensity
wavelength
150w15m_340nm
experimental data
fitting curve
Intensity
wavelength
150w15m_380nm
experimental data
fitting function
Intensity
wavelength

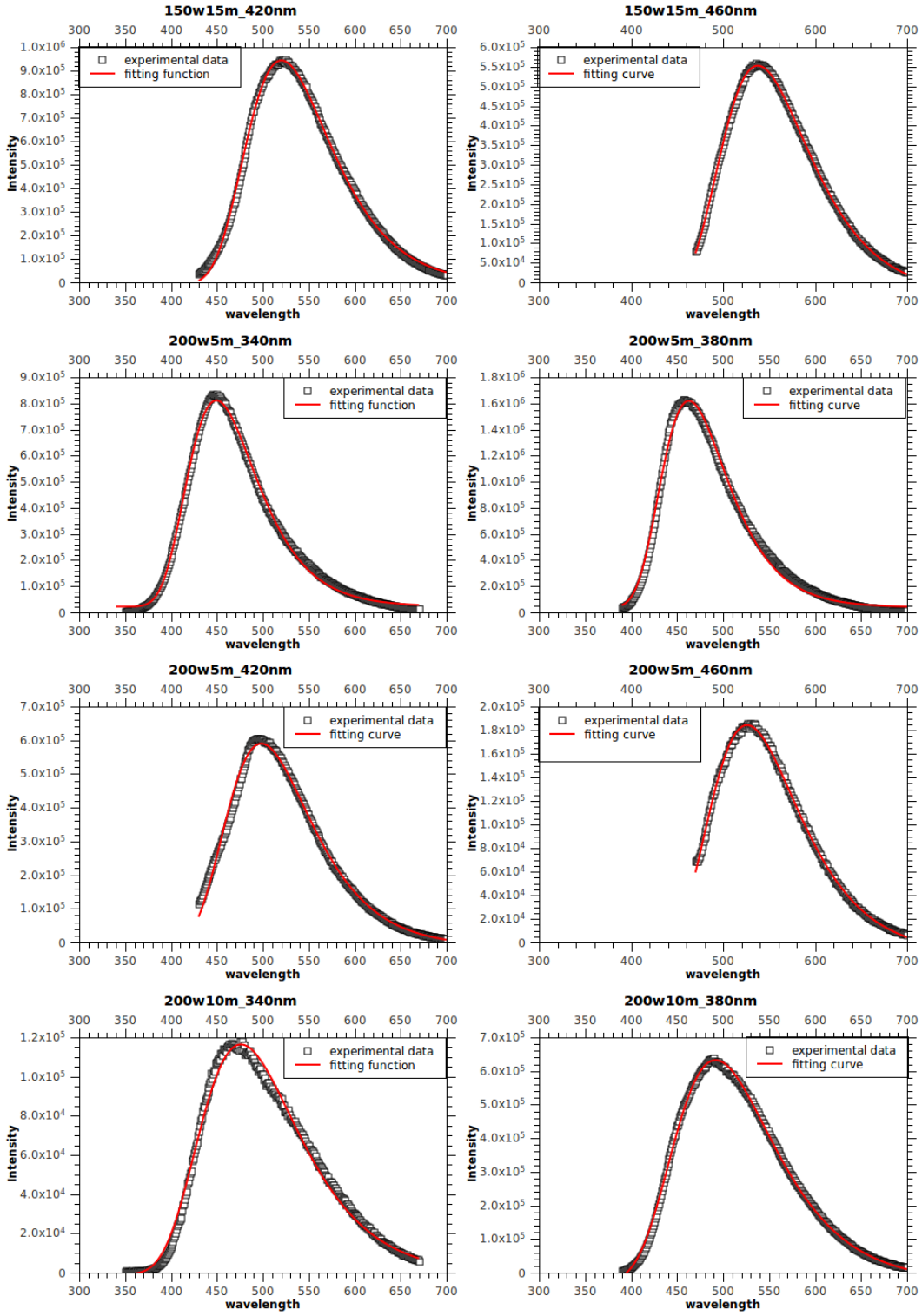
150w15m_420nm
experimental data
fitting function
Intensity
wavelength
150w15m_460nm
experimental data
fitting curve
Intensity
wavelength
200w5m_340nm
experimental data
fitting function
Intensity
wavelength
200w5m_380nm
experimental data
fitting curve
Intensity
wavelength
200w5m_420nm
experimental data
fitting curve
Intensity
wavelength
200w5m_460nm
experimental data
fitting curve
Intensity
wavelength
200w10m_340nm
experimental data
fitting function
Intensity
wavelength
200w10m_380nm
experimental data
fitting curve
Intensity
wavelength

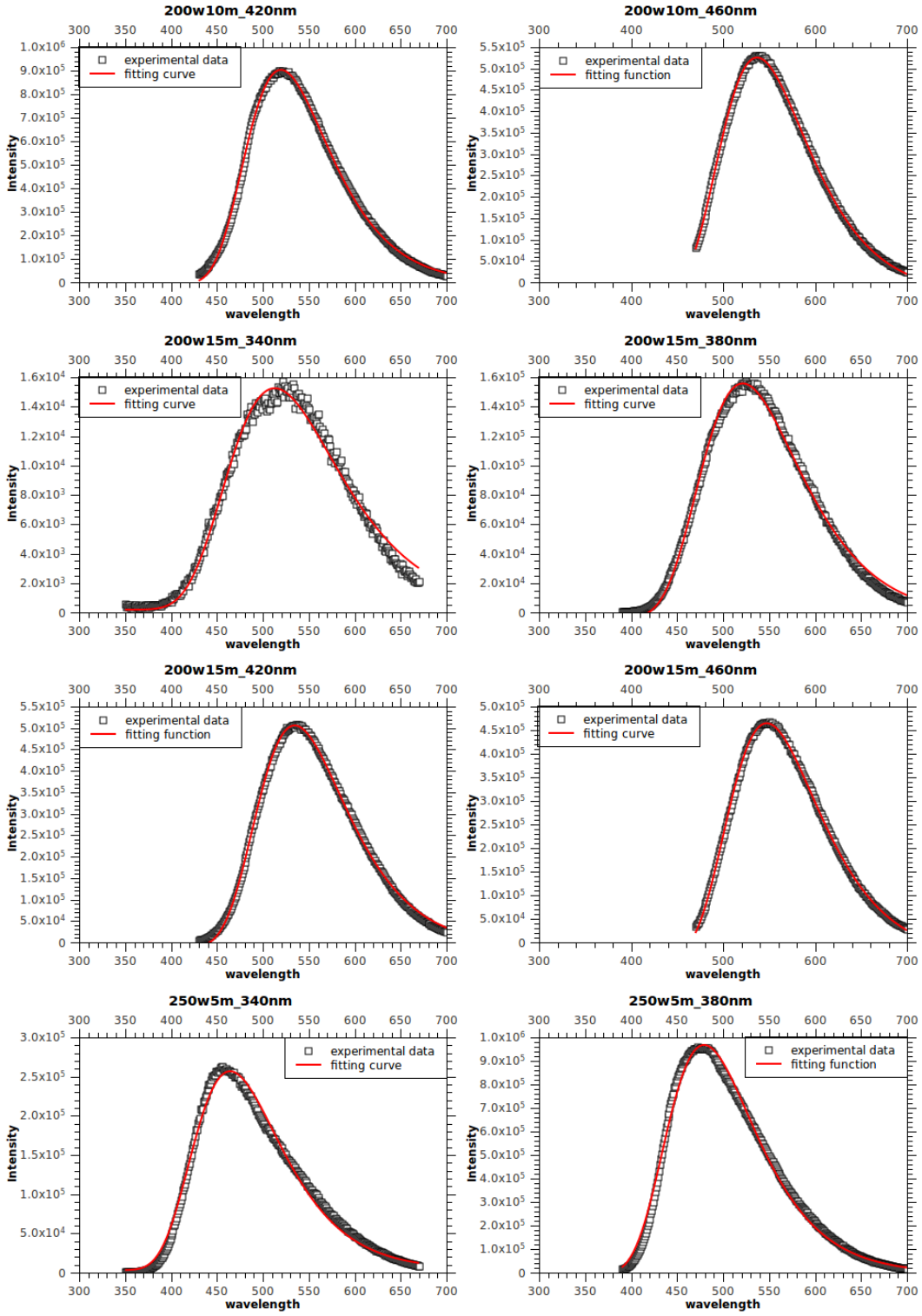
200w10m_420nm
experimental data
fitting curve
Intensity
wavelength
200w10m_460nm
experimental data
fitting function
Intensity
wavelength
200w15m_340nm
experimental data
fitting curve
Intensity
wavelength
200w15m_380nm
experimental data
fitting curve
Intensity
wavelength
200w15m_420nm
experimental data
fitting function
Intensity
wavelength
200w15m_460nm
experimental data
fitting curve
Intensity
wavelength
250w5m_340nm
experimental data
fitting curve
Intensity
wavelength
250w5m_380nm
experimental data
fitting function
Intensity
wavelength

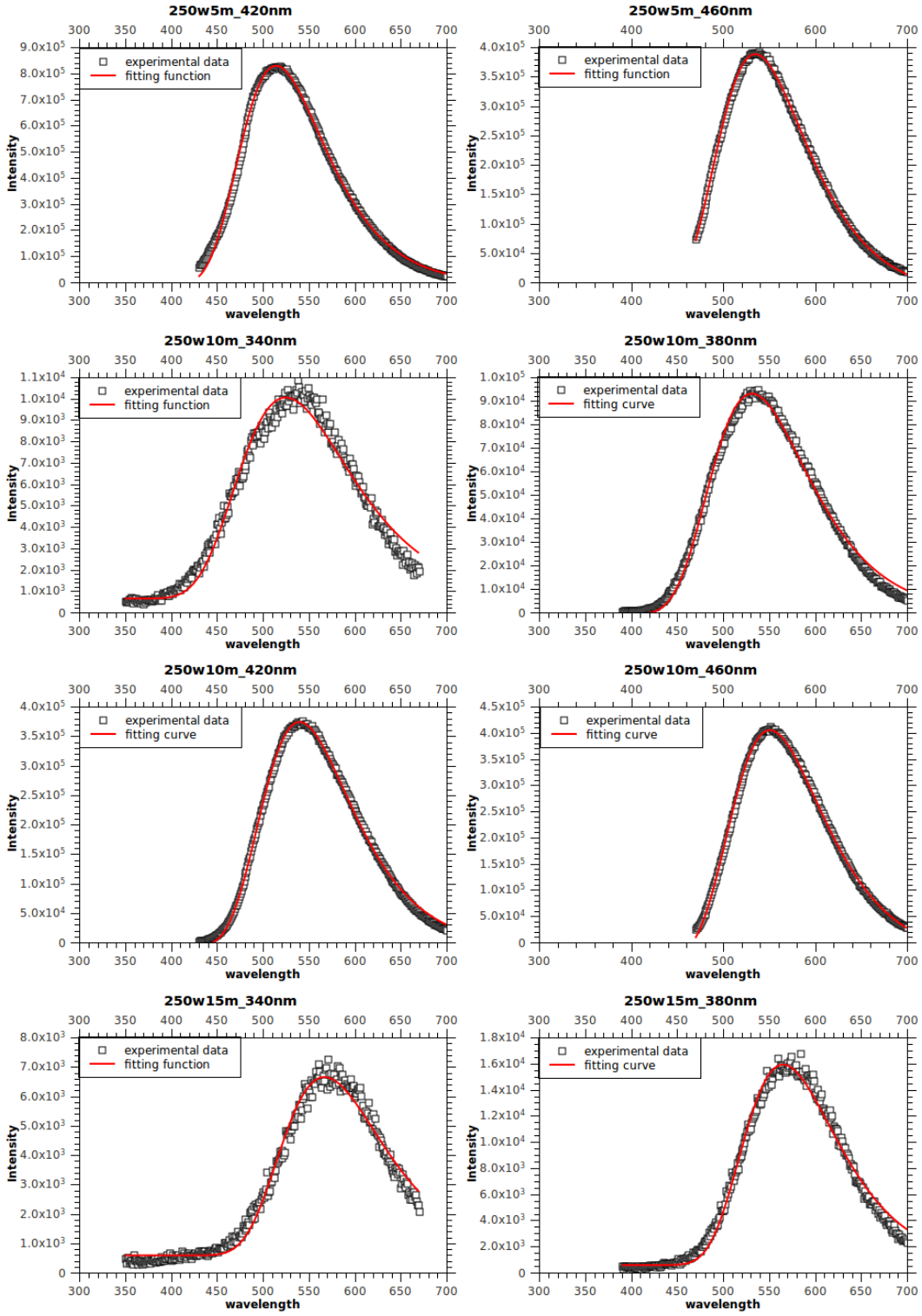
250w5m_420nm
experimental data
fitting function
Intensity
wavelength
250w5m_460nm
experimental data
fitting function
Intensity
wavelength
250w10m_340nm
experimental data
fitting function
Intensity
wavelength
250w10m_380nm
experimental data
fitting curve
Intensity
wavelength
250w10m_420nm
experimental data
fitting curve
Intensity
wavelength
250w10m_460nm
experimental data
fitting curve
Intensity
wavelength
250w15m_340nm
experimental data
fitting function
Intensity
wavelength
250w15m_380nm
experimental data
fitting curve
Intensity
wavelength

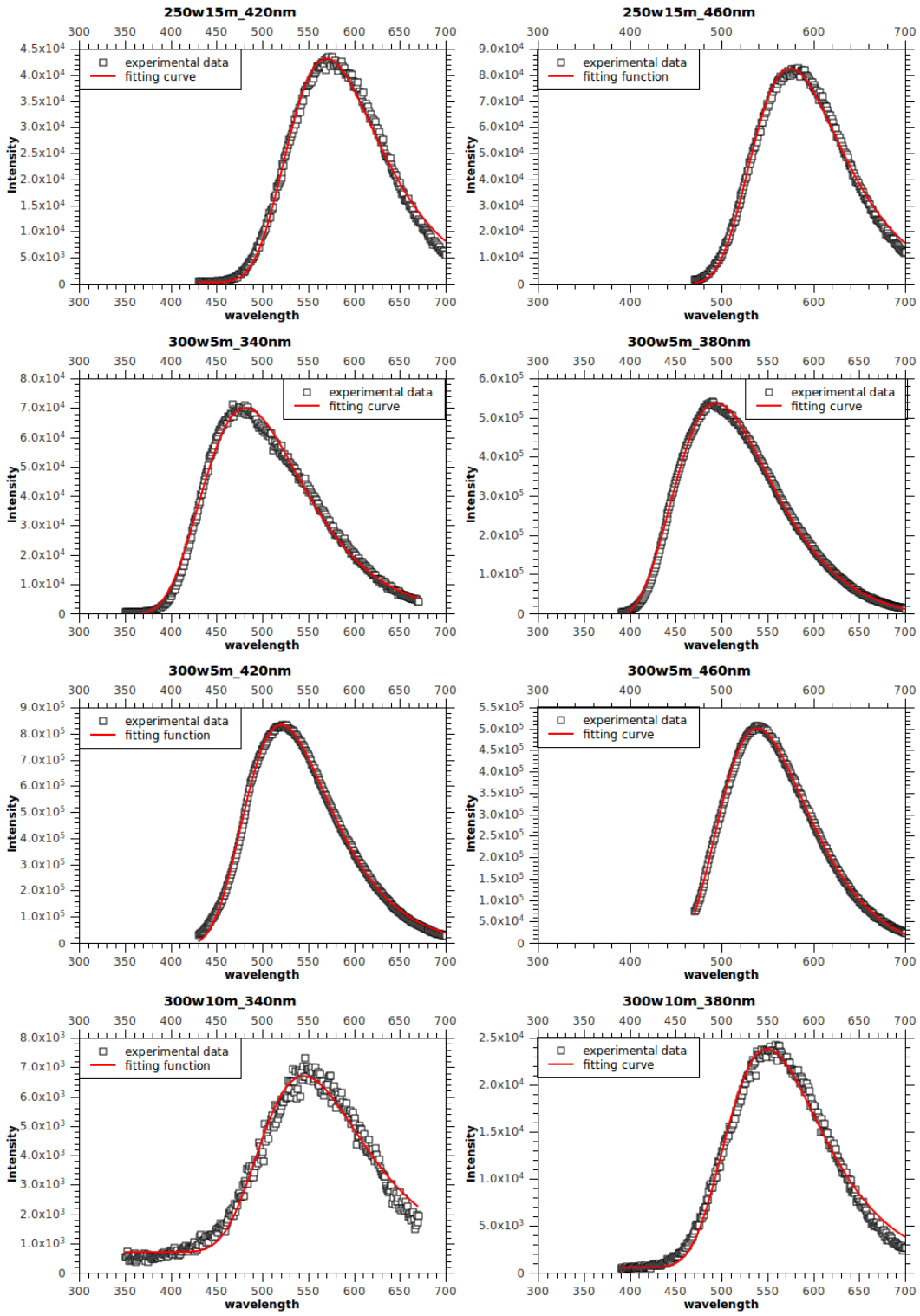
250w15m_420nm
experimental data
fitting curve
Intensity
wavelength
250w15m_460nm
experimental data
fitting function
Intensity
wavelength
300w5m_340nm
experimental data
fitting curve
Intensity
wavelength
300w5m_380nm
experimental data
fitting curve
Intensity
wavelength
300w5m_420nm
experimental data
fitting function
Intensity
wavelength
300w5m_460nm
experimental data
fitting curve
Intensity
wavelength
300w10m_340nm
experimental data
fitting function
Intensity
wavelength
300w10m_380nm
experimental data
fitting curve
Intensity
wavelength

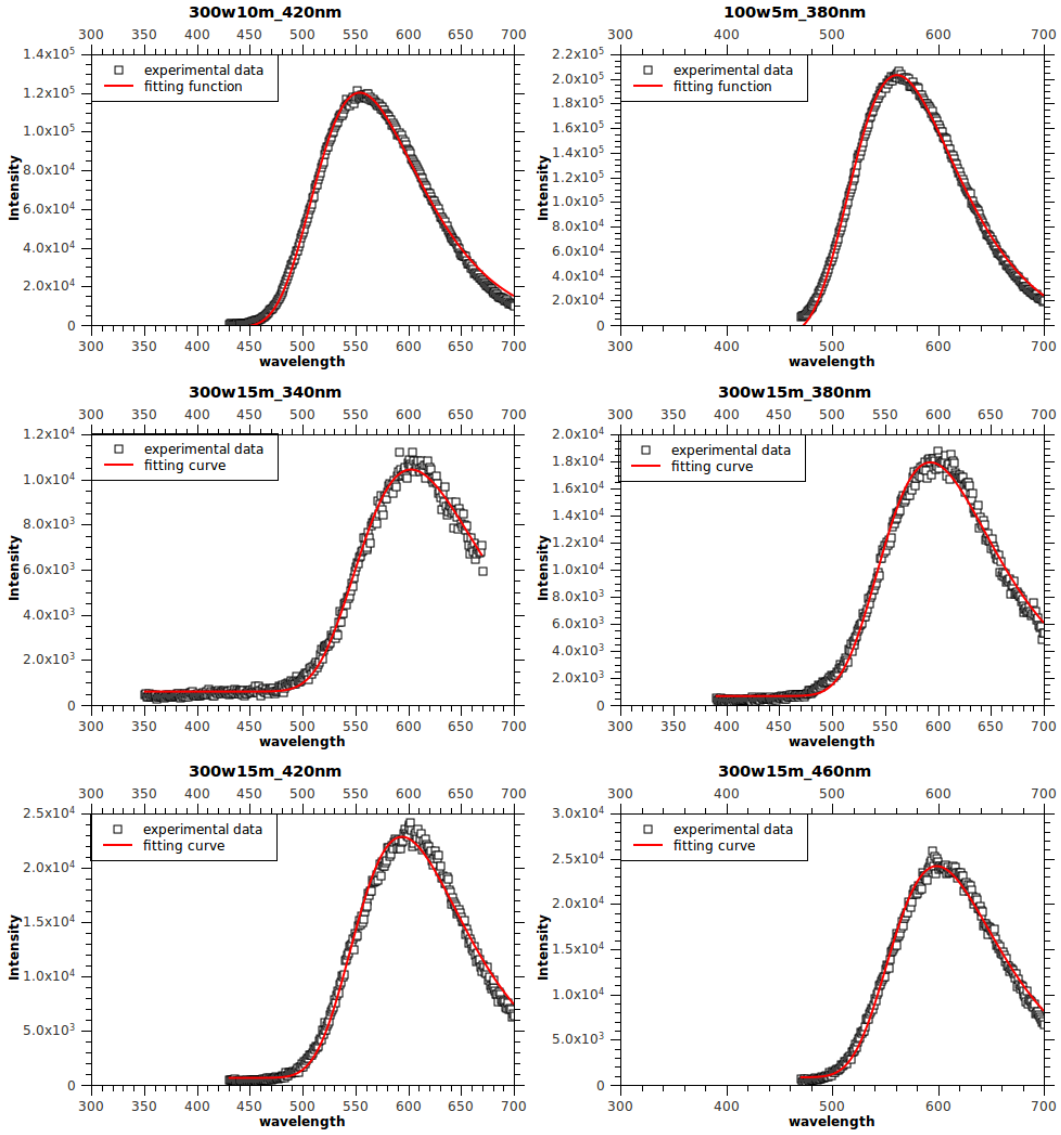
300w10m_420nm
experimental data
fitting function
Intensity
wavelength
100w5m_380nm
experimental data
fitting function
Intensity
wavelength
300w15m_340nm
experimental data
fitting curve
Intensity
wavelength
300w15m_380nm
experimental data
fitting curve
Intensity
wavelength
300w15m_420nm
experimental data
fitting curve
Intensity
wavelength
300w15m_460nm
experimental data
fitting curve
Intensity
wavelength

APPENDIX C

Excitation spectrum and fitting results

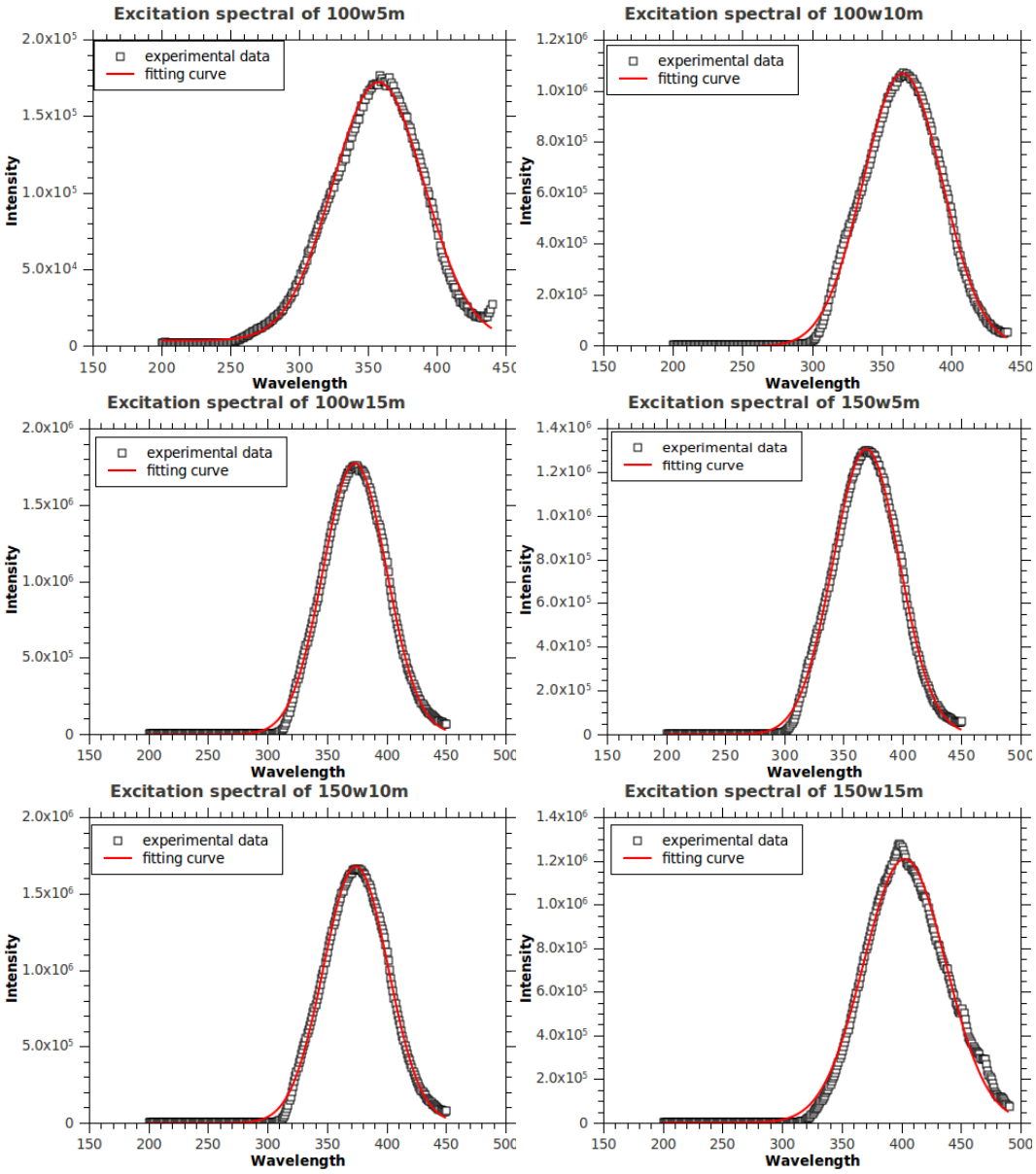

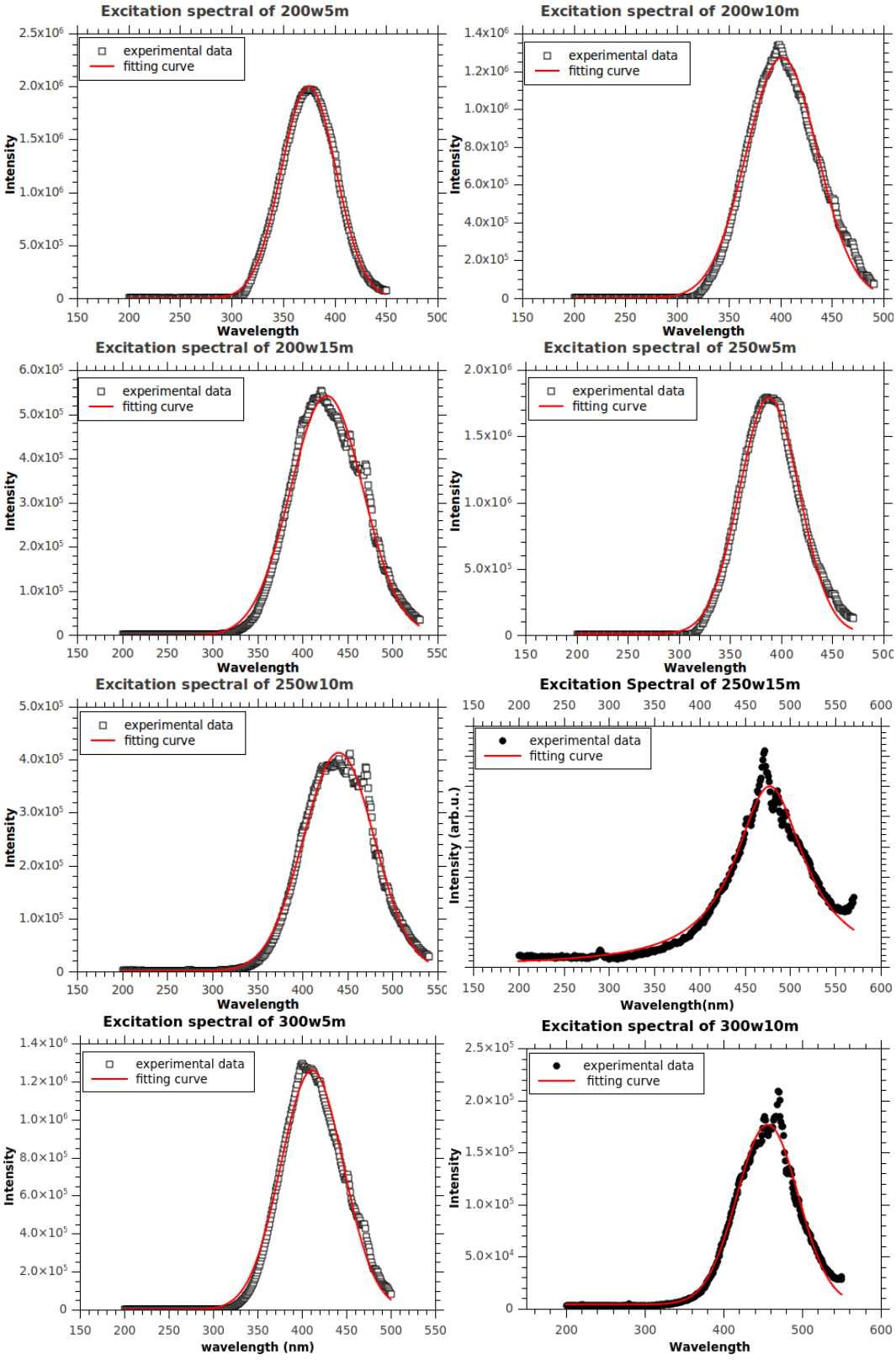
Excitation spectral of 200w5m
experimental data
fitting curve
Intensity
Wavelength
Excitation spectral of 200w10m
experimental data
fitting curve
Intensity
Wavelength
Excitation spectral of 200w15m
experimental data
fitting curve
Intensity
Wavelength
Excitation spectral of 250w5m
experimental data
fitting curve
Intensity
Wavelength
Excitation spectral of 250w10m
experimental data
fitting curve
Intensity
Wavelength
Excitation Spectral of 250w15m
experimental data
fitting curve
Intensity (arb.u.)
Wavelength(nm)
Excitation spectral of 300w5m
experimental data
fitting curve
Intensity
wavelength (nm)
Excitation spectral of 300w10m
experimental data
fitting curve
Intensity
Wavelength